UNIVERSITÉ DU QUÉBEC

THÈSE PRESENTÉE À

L'UNIVERSITÉ DU QUÉBEC À CHICOUTIMI

COMME EXIGENCE PARTIELLE

DU DOCTORAT EN INGÉNIERIE

PAR

CHUNYING ZHANG

MODELING AND SIMULATION OF MELTING PROCESS IN A SNOW SLEEVE ON OVERHEAD CONDUCTORS

MODÉLISATION ET SIMULATION DU PROCESSUS DE FUSION DU MANCHON NEIGE SUR CONDUCTEURS AÉRIENS

JUNE 2011

ABSTRACT

The general objective of this PhD study is to develop models that simulate the snow melting process on overhead conductors and predict snow shedding under various meteorological and current transmission conditions. In an attempt to validate this new model, a number of experimental tests were carried out in the CIGELE cooling chamber and wind tunnel, and the results obtained from these tests were then compared with those from numerical simulations.

Firstly, two-dimensional Reynolds-Average Navier-Stokes (RANS) simulations were implemented in FLUENT software to predict both the local heat-transfer coefficient distribution along the snow sleeve surface in a cross flow of air, and the overall heat-transfer rate. These investigations reveal the characteristics of forced convection around a snow sleeve, especially the effects resulting from the roughness of the snow surface and the non-circular shape of the sleeve. The study shows that roughness has a significant effect on the heat transfer rate, although the effect of the non-circular shape is negligible in most cases. The computational results show a satisfactory concordance with the theoretical analyses as well as with the experimental data derived from the literature in the field.

Secondly, a microstructure model was developed to estimate the equivalent thermal conductivity of dry snow. This study describes the relationship between the equivalent

thermal conductivity and the microstructure of dry snow under different temperatures regimes. These results were compared with those obtained in prior research, and showed good agreement. A set of experiments was carried out at the CIGELE laboratories and the results were compared with those produced by this particular model. Furthermore, the relationship between the snow conductivity model and the weather is introduced here.

Thirdly, a two-dimensional time-dependent numerical model of water percolation within a wet snow sleeve was constructed based on the Galerkin method. The effects of wind speed, air temperature, Joule heating, snow surface roughness and snow grain size was investigated. The numerical results show that Joule heating and snow surface roughness have an obvious influence on water percolation. The time required to reach quasi-steady state was reduced by 50% and more, considering that the electric current or surface roughness exceeded a critical value. The numerical results accord well with the experimental studies conducted at the CIGELE laboratories.

Fourthly, the problem of determining the occurrence of snow shedding was also investigated. Such an analytical model is based on a dry snow failure model and on experimental tests carried out at the CIGELE laboratories. It is a model which takes into account the effect of the water flow within the sleeve. The results show that the time required to snow shedding occurrence decreases in a non-linear fashion as the initial volume water content, the air velocity, and the electric current intensity increase. This model can provide a rapid estimation of the required Joule heat or wind to trigger snow shedding from the cable.

RÉSUMÉ

L'objectif général de cette recherche était de développer des modèles capables de simuler les processus de fonte de la neige accumulée sur des conducteurs aériens et de prévoir leur délestage, dans diverses conditions météorologiques et types de transmission de courant.

Dans le but de valider ce nouveau modèle, un certain nombre de tests expérimentaux ont été réalisés aux laboratoires de la CIGELE, à l'aide d'une chambre climatique et de la soufflerie réfrigérée, qui ont ensuite été comparés avec ceux simulés numériquement.

Premièrement, des simulations en deux dimensions Reynolds Average Navier-Stokes (RANS) ont été effectuées avec FLUENT pour prédire le coefficient de distribution du transfert de chaleur local, le long de la surface du manchon avec flux transversal d'air, ainsi que le taux global de transfert de chaleur. Ces investigations permettent de connaître les caractéristiques de la convection forcée autour d'un manchon de neige, et également les effets dus à la rugosité de la surface de la neige et à la forme non-circulaire du manchon. Elles montrent aussi l'effet significatif de la rugosité de surface sur le taux de transfert de la chaleur.

Deuxièmement, un modèle microstructural a été développé pour estimer la conductivité thermique équivalente de la neige sèche, qui établit la relation entre la conductivité thermique équivalente et la microstructure de la neige sèche dans divers régimes de température. Ces résultats ont été comparés avec ceux de recherches antérieures, montrant un bon accord. De plus, une série d'expériences a été réalisée dans les laboratoires de la CIGELE et leurs résultats ont été comparés avec ceux du modèle. Finalement, une relation entre le modèle de conductivité de la neige et la température a été proposée.

Troisièmement, un modèle numérique 2-D en fonction du temps, de la percolation de l'eau dans un manchon de neige fondante a été établi sur la base de la méthode de Galerkin. L'influence de la vitesse du vent, de la température de l'air, de l'effet Joule, de la rugosité de la surface de la neige et de la dimension des grains de neige a été étudiée. Les résultats du modèle montrent que l'effet Joule et la rugosité de la surface de neige ont des effets notables sur la percolation de l'eau. Le temps requis pour parvenir à un état de quasi-équilibre est réduit de 50% ou plus, si le courant électrique ou la rugosité de surface excèdent certaines valeurs critiques. On a trouvé que les résultats du modèle concordaient bien avec ceux obtenus expérimentalement aux laboratoires de la CIGELE.

Quatrièmement, la question de la détermination du déclenchement du délestage de la neige a été étudiée. Un tel modèle analytique est basé sur un modèle de défaillance de la neige sèche et sur des essais expérimentaux réalisés aux laboratoires de la CIGELE. Ce modèle prend en compte l'effet de l'écoulement de l'eau dans le manchon de neige. Les résultats montrent que le temps requis pour parvenir au délestage de la neige diminue de

façon non linéaire alors que la teneur en eau initiale, la vitesse de l'air et l'intensité du courant électrique augmentent. Ce modèle peut fournir une estimation rapide de la chaleur de Joule ou du vent nécessaire pour déclencher le délestage de la neige sur un câble.

ACKNOWLEDGEMENTS

First of all, I would like to express my deepest gratitude to my supervisor, Professor Masoud Farzaneh who is Chairholder of the NSERC/Hydro-Québec/UQAC Chair on Atmospheric Icing of Power Network Equipment (CIGELE), as well as the Canada Research Chair, Tier 1, on the Engineering of Power Network Atmospheric Icing (INGIVRE). He granted me the invaluable opportunity to pursue my Ph.D. studies with his encouragement, guidance and support from the initial to the final level thereby enabling me to develop a thorough understanding of the subject.

I must express particular appreciation to Professor László I. Kiss, the co-director of the project. His ideas and the discussions we have had have helped immensely with this study.

I would like to thank Dr. László E. Kollár who helped me so much. I learned many things from him and he has always been most kind.

I am grateful to the researchers, professionals and technicians at CIGELE, who who provided me with their personal support, technical support, and valuable suggestions) in the fulfillment of this study. These great people include Pierre Camirand, Claude Damours, Denis Masson and Xavier Bouchard. I am thankful for the time they have devoted to me and the pains they have taken. I would also like to extend my thanks to all of my peer students at the CIGELE for the pleasant times spent together.

An acknowledgement is specifically extended to M. L. Sinclair, for her patience in editing my thesis.

Lastly, my profound gratitude goes to my family, for their substantial contribution and sacrifice throughout the duration of my Ph.D. studies.

CONTENTS

LIST OF FIGURES

LIST OF TABLES

LIST OF SYMBOLS

Symbol	Concept	Dimensions
a	Semimajor axis	m
A	Area of domain under study	m^2
b	Semi-minor axis	m
C	Moisture capacity	1/m
C_{Ks}	Roughness constant	
d	Deformation factor	
D	Diameter	m
e	Ellipse eccentricity	
f	Ellipse flatness ratio	
g	Gravitational acceleration	m/s^2
G	Geometry	
h	Heat transfer coefficient	$W/m^2 K$
h_g	Height of snow grain	m
h_p	Pressure head	m
i	Turbulence intensity	
I	Electric current	A
k	Thermal conductivity	W/m K
k_e	Equivalent thermal conductivity	W/m K
k_i	Intrinsic permeability	m^2

k_{rw}	Relative permeability of water	
K	Saturated hydraulic conductivity	m/s
K_s	Roughness Height	m
l	Length of bond	m
L	Latent heat	J/kg
M	Mass	kg
Nu	Nusselt number	
P	Pressure	Pa
Pr	Prandtl number	
q	Heat flux	W/m^2
Q	Heat transfer rate	W
r	Roughness Constant	
R	Radius	M
R	Thermal resistance	m^2 K/W
Re	Reynolds number	
Re_t	Turbulent Reynolds number	
S	Water saturation	
S_e	Effective water saturation	
t	Time	s
T	Temperature	K or °C
u_{avg}	Mean flow velocity	m/s
v	Velocity	m/s
V	Volume	m^3
W_v	Liquid flux	m^3/s

x, y, z	Cartesian coordinates	
Greek Symbols		
α	Thermal diffusivity	m^2/s
β	Weighting parameter	
θ	Angle from stagnation point	Degree
ϑ	Contact angle	Degree
μ	Dynamic viscosity	$N\ s/m^2$
ρ	Mass density	kg/m^3
σ	Stress	Pa
τ	Shear stress	Pa
ψ	Pore water pressure head	m
ϕ	Porosity	
Subscripts		
a	Dry air	
b	Bond between snow grain	
e	Equivalent or effective	
f	Film	
	Failure	
g	Saturated moist air	
i	Ice	
m	Melting point	
s	Surface	
	Snow	
w	Water	

CHAPTER 1

INTRODUCTION

1.1 Defining the Problem

In general, it has been considered that snow accretion on overhead power lines occurs only when wet snowflakes adhere to wires at surface temperatures slightly above freezing. Sakamoto (2000) suggested that, in practice, the phenomenon of snow accretion may customarily be experienced under a relatively wide range of combinations of meteorological parameters. The observation records show that the snow accretion on overhead wires may occur at air temperatures as low as -7°C.

Wet snow accretion, as reported by Colbeck *et al.* (1982), is known to be particularly troublesome since a large mass accumulation can occur in only a few hours. Snow accretion on overhead transmission lines and wires may thus be deemed a serious problem posing tremendous threats to existing power installations. Its subsequent shedding tends to cause power outages and severe damage to the power network structures, thereby leading to a number of serviceability, safety, and mechanical reliability issues.

Many countries such as Canada, the United States, the United Kingdom, France, Germany, Norway, Iceland, and Japan experience wet snowfalls which affect the related overhead transmission networks. The damage caused by a single wet snowstorm can necessitate the expenditure of sums on the order of 100 million dollars. Past records show that the occurrence of wet snow accretion is relatively more common and may be equally as catastrophic in France, Japan, and Iceland.

The shape of a snow sleeve accreted on overhead lines depends not only on meteorological parameters such as air temperature and velocity, but also on line parameters such as material and stranding. The snow sleeves taken under observation were usually almost cylindrical due to the effects of wind flow and cable torsion (Wakahama *et al.*, 1977, Admirat, 1988, Yukino, 1998), as shown in **Figure 1-1**.

Figure 1-1 Wet-snow accretion on a 300 kV power line in Dale-Fana, Norway (Photograph from Satnett)

Observations of wet snow accretion or shedding from a cable are rare, however, and are consequently not well documented. Few people have actually witnessed the phenomenon, while observations tend to be varied and scattered.

In order to minimize the damage, the physics of snow-shedding, as well as the effect of the different factors which influence snow shedding, are both important areas of research.

A satisfactory theoretical model for snow shedding from overhead lines is not yet readily available, even though extensive studies on snowing phenomena have been carried out to date by researchers in the domain. There are several factors existing which hamper research and investigation into the snow-shedding process.

- ***The complexity of the snow-shedding phenomenon itself.*** The shedding involves several feedback mechanisms and non-linear relationships between various factors, including the fact that ambient forced or natural air convection depends on the air temperature and velocity as well as on the shape of the snow sleeve and its surface roughness; and that water percolation within the snow not only depends on but also transforms the snow microstructure.
- ***The difficulty of predicting and* measuring snow *morphology.*** Significant characteristics of the snow microstructure involve the arrangement of snow grain, pores, and possibly liquid water; they tend to change dynamically due to water percolation within the snow, or as a result of such environmental effects as air convection. Snow-grain morphology is one of the most important parameters for predicting snow failure, or shedding. This parameter strongly influences the

mechanical properties and the settlement rate. There are, however, no effective methods available at present for observing the morphology of wet snow (Dozier, 1987; Brun, 1991).

- ***The lack of experimental data.*** Snow shedding under natural conditions is rarely observed. A method developed by Roberge (2006) was used to reproduce wet-snow sleeves in a cold chamber or wind tunnel. There are considerable technical problems involved in measuring accurately these quantities such as liquid water content, however, even under laboratory conditions.

The study of snow-shedding mechanisms poses a genuine challenge, considering the paucity of studies in the overview of the literature.

1.2 Research Objectives

The general objectives of this study include developing models which simulate the snow melting process within a wet snow sleeve and which also predict snow-shedding under various meteorological conditions or the current prevailing transmission environment.

The standard research objectives and modeling procedures are listed in **Figure 1-2.**

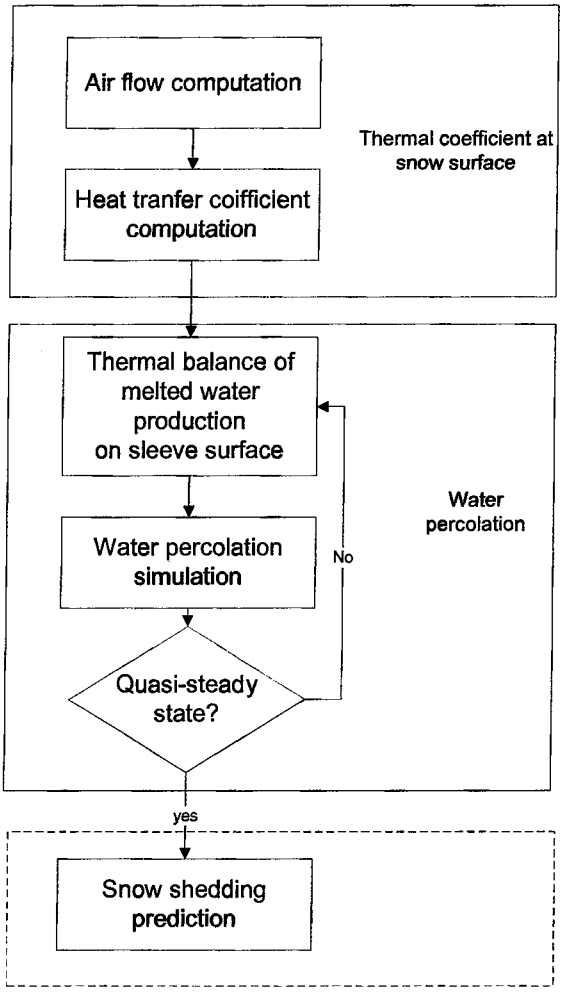

Figure 1-2 Research objectives and modeling procedure

A. Analysis of the Convective Heat Transfer around a Snow-Covered Conductor

An assessment of the overall Heat Transfer Coefficient (HTC) and local HTC distribution for a snow sleeve is required in order to complement the snow-melting model. Therefore, the objective of this part of the study is to determine the convective heat transfer coefficients around a snow sleeve in a cross-flow of air.

During the snow melting process, the snow sleeve changes its shape as shown in **Figure 1-3**. As a result, the air velocity distribution around the sleeve will change continually and will lead to variation in the local convective heat transfer rate.

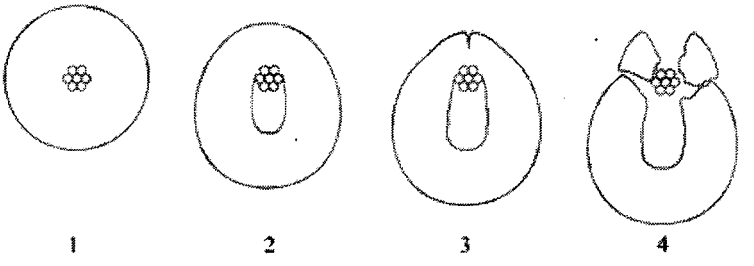

Figure 1-3 Creep progressions up to shedding (from Roberge 2006)

Not only has the shape of the snow sleeve influenced local HTC distribution, but also the status of the snow surface. The sleeve surface status is the research emphasis in this present study.

A snow sleeve has a relatively higher water content before snow shedding occurs. It is, therefore, reasonable to assume that the greater part of the sleeve surface is at a constant temperature, 0°C, while most prior experiments were conducted in a situation of constant heat flux from the surface.

B. Analysis of the Water Percolation within the Snow Sleeve

Wet snow was classified into two basic modes, or regimes, based on liquid water saturation: the pendular and the funicular. At low LWC values (Figure 1-4a), the water forms pendular rings at the points of contact between the particles, and the air is connected

throughout the pack. When the saturation level rises, however, the air is no longer connected; this is known as the funicular regime (see Figure 1-4b).

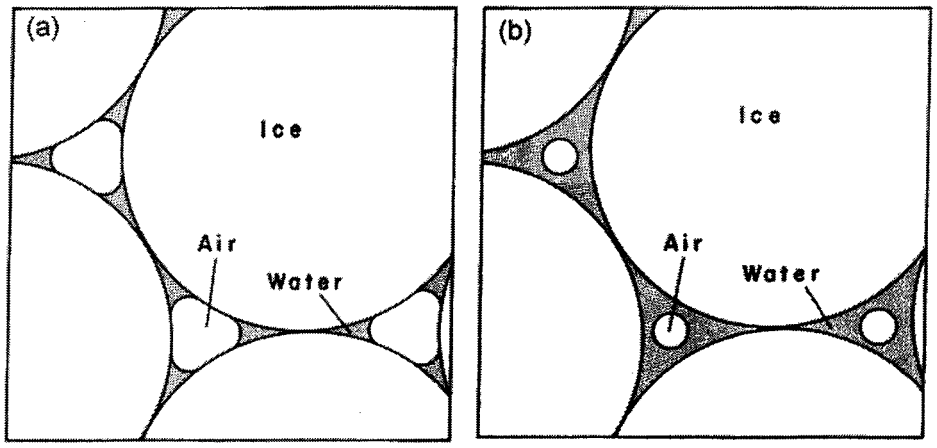

Figure 1-4 Wet snow in the (a) Pendular and (b) Funicular regimes. Reproduced from Armstrong *et al.* (1976)

Water percolation in snow is of fundamental importance in snow hydrology. Snow melting and water percolation are dynamic, evolutionary processes, however, and they are indeed quite complicated. The geometry of a snow sleeve with a hole produced by a line conductor is even more complex and is thus unsuitable for a one-dimensional model. For this reason, the mechanism study will pose a genuine challenge.

The water percolation within the snow sleeve depends not only on the initial water saturation but also on the microstructure of wet snow, including porosity, snow grain size and shape, which are all affected by the concurrent heat exchange between the water, air, and ice matrix. The wind velocity, air temperature, Joule heating, and snow surface roughness have an evident influence on the rate at which snow melts.

The objective here is to develop a two-dimensional time-dependent numerical model of water percolation within a wet snow sleeve.

C. Determining the Equivalent Conductivity of Dry Snow

For snow, which is composed of various substances in different states, heat transferred by conduction may occur in several forms. As temperature changes, snow exhibits a dynamically complex process represented by three fractions continuously changing their ratios: ice particles, water, and the gaseous phase (including air and water vapor). Based on an elegant experiment designed by de Quervain (1958, 1972) it was estimated that the ice matrix for snow samples carried 55-60% of the heat, the rest moving across the pores as sensible or latent heat. Reviewing the literature on vapor diffusion in snow, Colbeck (1993), concluded that 30-40% of the heat is moved by vapor transport because the vapor gradient enhancement predominates over the blocking effect of the ice matrix.

The thermal characteristics of snow depend upon various factors such as the thermal conductivity of constituent phases, porosity, shape and size of snow grain, and so forth. A microstructure model have a conceptual understanding of the snow structure and take into account the influence from geometry of snow grain and connection bond.

An assessment of the equivalent thermal conductivity of snow is required in order to complete the snow melting and shedding model. The objective of this part of the study is to determine the equivalent thermal conductivity of dry snow, especially for the snow accreted on an overhead cable.

D. Prediction of Wet Snow Shedding from an Overhead Line Conductor

Snow is a complex material with unique properties including high compressibility and thermodynamic instability. It is, therefore, not surprising that the failure mechanisms of wet snow shedding are not well understood, and that they are in fact, controversial.

A great number of studies have been carried out on dry snow failure, but wet snow shedding is more complicated. The water within the wet snow may incline or decline snow shedding according to snow porosity. Water percolation has an evident effect on snow shedding, in that it changes the size and shape of snow grains as well as the bonding connection between neighboring snow grains.

The objective of this portion of the work is to develop a mathematical model for predicting the occurrence of snow shedding based on the experimental data obtained at the CIGELE laboratories. This model is able to provide a rapid estimation of the Joule heat or wind required to trigger snow shedding from the cable.

1.3 Methodology

This research project will be carried out in such a way as to ascertain that theoretical modeling or numerical simulation is followed by the type of experimental investigation which will produce the relevant data for validating the preceding modeling procedures.

A. Analysis of the Convective Heat Transfer around a Snow-Covered Conductor

Two-dimensional State Reynolds-Average Navier-Stokes (RANS) simulations are here implemented in a commercial computational fluid dynamic software package, FLUENT, to facilitate predicting both the overall heat-transfer rate and the local heat-transfer coefficient distribution along the snow sleeve surface subsequently.

Firstly, a set of elliptical shapes were investigated and their values compared with the values obtained from the circular cylinder shape.

Secondly, in carrying out the above, the surface roughness of a circular cylinder sleeve was taken into account. A variety of roughness values were investigated and compared with each other under the same Reynolds number conditions.

The computational results were then compared with the theoretical analyses and experimental data from the literature in the field.

B. Analysis of Water Percolation within the Snow Sleeve

A two-dimensional Finite Element Method (FEM) and a Finite Volume Method (FVM) time-dependent model were both built to simulate melted-water percolation within a snow sleeve under the different prevailing snow properties and outer environment conditions.

With the above-declared intention, the effects of wind velocity, air temperature, Joule heating, snow surface roughness, and snow grain size were all investigated and analyzed.

The experimental study was carried out to validate the numerical approaches as well as to acquire a better understanding of the water percolation process within a snow sleeve.

Wet snow sleeves were reproduced and the variations of liquid water content and snow density were recorded.

C. Determining the Equivalent Thermal Conductivity of Dry Snow

A microstructure model was developed to estimate the quantitative relationship between the equivalent thermal conductivity and the constituents of dry snow.

First, the shape of the snow grain was classified into four main types and a microstructure model was developed to estimate the equivalent conductivity and density of the snow sleeve. Second, a study was made of the dependence of the thermal conductivity on such snow constituents as air, ice, and vapor, as well as on the effects of the temperature. Third, a set of experiments was conducted and a comparison was made with the results of the analytical model. The temperature gradient were measured within a dry snow sleeve. Lastly, the relationship between snow microstructure and the prevailing weather conditions was presented.

D. Prediction of Wet Snow Shedding from an Overhead Line Conductor

A dry snow failure model was revised and extended to apply to wet snow shedding from an overhead line conductor. The effective initial water content, in the form of a custom-defined parameter, was introduced, accounting for the effect of the water percolation within the snow sleeve.

With regard to the melted water percolation, the outer conditions were subdivided into two types: forced air convection and Joule heating with natural air convection. Under the former conditions, melted water percolates throughout all areas within the snow sleeve and the rate of snow melting is not consistent due to local HTC variation along the snow sleeve surface. Under the latter conditions, melted water concentrates on the lower section of the snow sleeve.

Wet snow sleeves were reproduced and the occurrence of snow shedding were recorded at the CIGELE laboratories. The experimental data are used to fit the value of the parameters in this empirical model.

CHAPTER 2

A NUMERICAL STUDY OF HEAT CONVECTION AROUND A SNOW SLEEVE IN A CROSS-FLOW OF AIR

2.1 Introduction

Snow accretion on overhead transmission lines and ground wires can lead to a number of serviceability, safety, and mechanical issues. In order to develop methods for preventing snow accretion or shedding from overhead conductors, it is necessary to estimate the heat transfer and flow characteristics around snow sleeves from the point of view of various engineering aspects. For example, convective heat transfer plays a significant role in the thermal balance for snow melting and refreezing processes.

The air flow around a circular cylinder at a high Reynolds number (*Re*) has long been the subject of intense attention from academic and practical standpoints. This flow is concerned with the complicated interaction between the transition and separation of the boundary layer on a rounded surface. A large number of studies were carried out by numerous investigators, and several empirical correlations were developed for the heat transfer coefficient.

Considering that a snow sleeve is not always a perfect cylinder, however, it is necessary to make a specific study of snow sleeves in this respect.

This chapter presents the results of a numerical investigation into the effects of the special characteristics of a snow sleeve, including surface roughness and non-circular shape, on the local HTC distribution around the sleeve under different wind conditions.

1. Non-Circular Shape

During the snow melting process, the outer shape of the sleeve changes continuously due to the melted water flow, the metamorphism of the ice matrix within the snow, and so forth.

For the purposes of this investigation, a set of elliptical cylinders was simulated in a cross flow of air. The numerical results were compared with those for circular cylinders.

2. Roughness

In prior works, the snow sleeve was assumed to have a smooth surface but, in actuality, it has a rough surface. Micro-reliefs on the snow surface are formed by a process of erosion and snow redeposition by the wind.

Normally, increasing the roughness increases the heat transfer rate in the turbulent boundary layer and, in addition, causes the transition from a laminar to a turbulent layer to occur earlier.

A total of 10 wind scenarios were simulated in FLUENT. The wind varies from 1 to 10m/s, and the Reynolds number from 7400 to 74 000. Three typical scenarios are presented here.

2.2 Review of the Literature

The air flow past a circular cylinder at a high Reynolds number has long been the subject of intense attention from academic and practical studies. This subject is concerned with the complicated interaction between the transition and separation of the boundary layer on rounded surfaces. Numerous studies have been carried out and several empirical correlations have been developed for the heat transfer coefficient.

The local and overall heat transfer coefficient (HTC) can be determined by:

- experiments (traditional electrical heating method, optical method)
- numerical calculations (using finite volumes, differences and element methods)

As is well known from the literature, the laminar boundary layer over the front stagnation point of a cylinder in a cross-flow is the thinnest and its thickness increases with downstream displacement. Separation of the laminar boundary layer takes place when the low velocity fluid close to the cylinder wall cannot overcome the adverse pressure gradient over the rear portion of the cylinder and the flow eventually stops and begins to move in the opposite direction (Incropera *et al.*, 2002). Fluid movement starts to curl and gives rise to vortices that shed from the cylinder. The Nusselt number then increases as a result of the intense mixing in the separated flow region, called the wake.

The complicated flow pattern across a cylinder greatly influences heat transfer. Giedt (1949) proposed an experimental schematic to measure the variation of local HTC along the circumference of a circular cylinder in a cross-flow of air. Achenbach (1975), Zhukauskas (1985), Scholten *et al.* (1998) and Buyrul (1999) also presented the distribution of local HTC along a circular or elliptical surface by means of well-designed experiments. **Figure 2-1** describes simultaneous measurements of time-resolved heat flux at the surface of a cylinder in a cross-flow through wind tunnel experiments by Scholten *et al.* (1998).

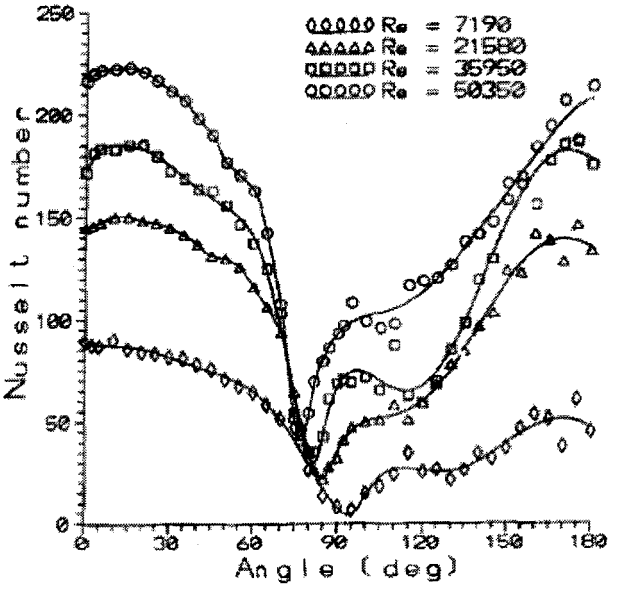

Figure 2-1 Surface Nusselt number by Scholten *et al.* (1998)

The complicated nature of the cross-flow around the bluff body makes it an excellent case for assessing the ability of computational software to reproduce real flow conditions. FLUENT and CFX are popular programmes used to simulate the process of air flow and heat transfer.

A modified ***k-ω*** turbulence model proposed by Durbin (1993, 1996) was implemented in FLUENT by Szczepanik *et al.* (2004). The modification arose from the unfortunate tendency of two equation turbulence models to over-predict levels of turbulent kinetic energy close to a stagnation point. **Figure 2-2** shows the ***Nu*** profiles for a given Reynolds number studied, including the experimental data from Scholten *et al.* (1998) and also considering the overall comparison between the experiment and the simulation.

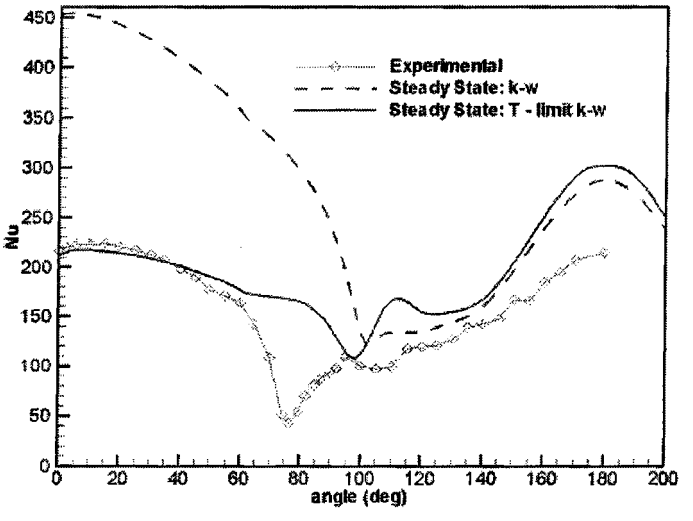

Figure 2-2 Surface Nusselt number for ***Re*** = 50350 by Szczepanik *et al.* (2004)

Péter (2006) conducted an intensive study on heat exchange around a circular cable. He utilized the Finite Volume Method (FVM) to study the relationship between the local HTC distribution and the Reynolds numbers.

Little work is known to have been carried out for cylinders with rough surfaces. Elmar (1977) and Achenbach (1977) designed a series of tests to obtain local heat transfers on

rough surfaces and Makkonen (1985) developed a mathematical boundary-layer model to predict the local HTC distribution along rough cylinder surfaces.

2.3 Modeling in FLUENT

2.3.1 Geometry

The snow sleeve was modeled as a circular or elliptic cylinder while a square flow domain was created around the cylinder, as shown in **Figure 2-3**. A uniform velocity at the inlet of the flow domain can thus be specified.

The general procedure for solving the problem is:

a) create the geometry (cylinder and flow domain)

b) set the material properties and boundary conditions

c) mesh the domain

d) carry out the computation in FLUENT

e) analyze the results.

A flow domain was created surrounding the cylinder. The upstream length is 15 times the radius of the cylinder, and the downstream length is 40 times the same radius, while the width of the flow domain is 50 times that radius. To facilitate meshing, a square with a side length of 6 times the radius of the cylinder was created around the cylinder. The square was then split into four pieces, as shown in **Figure 2-3**.

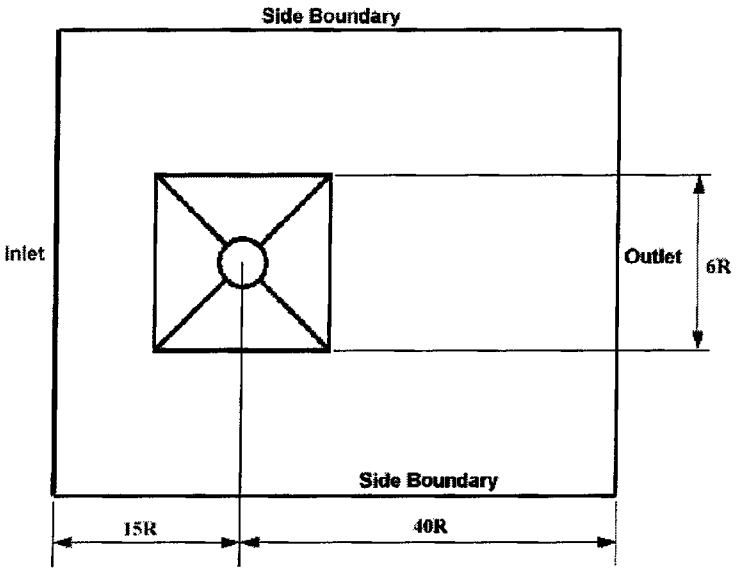

Figure 2-3 Air flow domain schematic

2.3.2 Mesh

The edges were meshed using the First Cell Height and the calculated number of intervals. The entire domain was meshed using a map scheme (**Figure 2-4**). Only the upper part of the domain was selected in order to save computing resources.

A boundary layer with 12 rows was placed at the cylinder wall using the calculated value of First Cell Height.

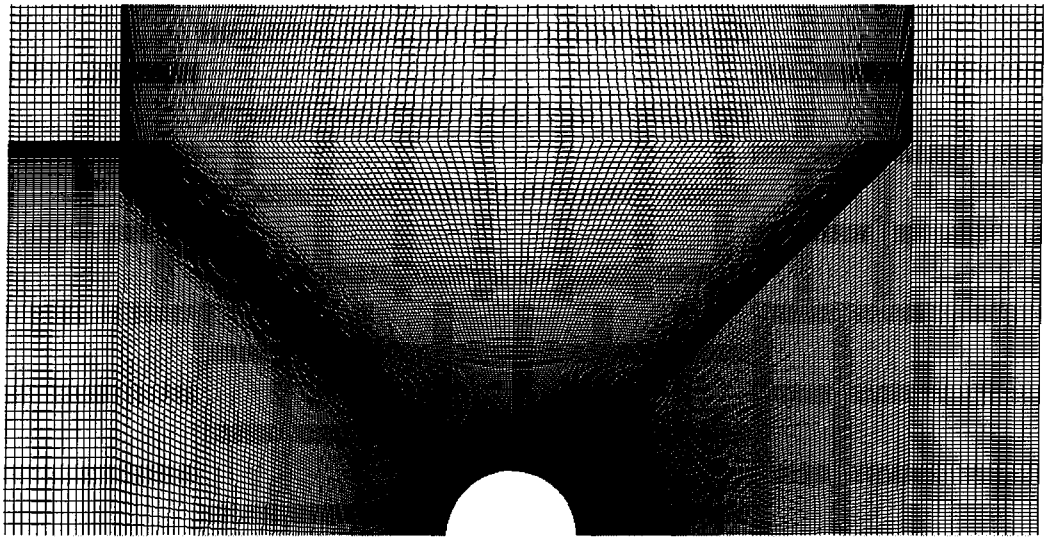

Figure 2-4 Partial schematic of a domain mesh

2.3.3 Boundary Conditions

The boundary conditions were assigned in FLUENT as shown in following table.

Table 2-1 Boundary conditions assigned in FLUENT

Boundary	Assigned As
Cylinder	Wall
Inlet	Velocity inlet
Side boundaries	Symmetry
Outlet	Pressure outlet

2.3.4 Reynolds Numbers and Flow Classification

Table 2-2 provides the Reynolds numbers for airflow under different air velocities. The outer diameter of the cylinder was assumed as 0.1m.

Table 2-2 Reynolds number at different air velocities

Velocity (m/s)	Reynolds number
1	7407
2	14815
3	22222
4	29630
5	37037
6	44444
7	51852
8	59259
9	66667
10	74074

Based on the Reynolds numbers, the following physical models are to be recommended:

- $Re < 1000$ laminar flow
- $1000 < Re < 10000$ low Reynolds number k-ω model or k-ε model
- $Re > 10000$ k-ω model or k-ε model

At higher Reynolds numbers, and as presently investigated, the wake of the boundary layer becomes turbulent, a turbulence model should thus be chosen. Two-equation models such as the k-ω model or the k-ε families offer the ability to introduce turbulence into the flow.

2.3.5 Turbulence Models

For numerical solutions of the Reynolds-averaged Navier Stokes equations, the commercial Computational Fluid Dynamic (CFD) software package, FLUENT, was used. FLUENT uses the finite volume method (FVM) to solve the governing equations sequentially. Several turbulence models were used in this study. From among these, the results obtained from the shear stress transport (SST) k-ω model show better agreement when compared to the experimental data.

The SST k-ω turbulence model utilizes a calculation of turbulent viscosity based on the standard k-ω model. Thus, the closure coefficients and other relations also differ slightly. Nonetheless, the SST k-ω turbulence model may be considered the standard or unmodified turbulence model for the current study.

The SST k-ω model was developed by Menter to blend the robust and accurate formulation of the k-ω model effectively in the near-wall region with the free-stream independence of the k-ω model in the far field. To achieve this, the k-ω model was converted into a k-ω formulation. The SST k-ω model is similar to the standard k-omega model, but includes the following refinements.

1. The standard k-ω model and the transformed k-ε model are both multiplied by a blending function and both models are added together. The blending function is designed to be one in the near-wall region, which activates the standard k-ω model, as well as zero, away from the surface, which activates the transformed k-ε model.

2. The SST model incorporates a damped cross-diffusion derivative term into the ω equation.
3. The definition of the turbulent viscosity was modified to account for the transport of the turbulent shear stress.
4. The modeling constants are different.

These features make the SST ***k-ω*** model more accurate and reliable for a wider class of flows (e.g., adverse pressure gradient flows, airfoils, transonic shock waves) than the standard ***k-ω*** model. Other modifications include the addition of a cross-diffusion term in the ω equation and a blending function to ensure that the model equations behave appropriately in both the near-wall and far-field zones.

2.3.6 Determining Turbulence Parameters

The flow across the snow sleeve was solved as an incompressible problem with air being the fluid. Pressure discretization was set by using the Standard and other Second Order Upwind. This coupled method was adopted for pressure-velocity coupling.

In most turbulent flows, higher levels of turbulence are generated within the shear layers which enter the domain at the flow boundaries, making the result of the calculation relatively insensitive to the inflow boundary values. Nevertheless, caution must be used to ensure that boundary values are not so unphysical as to contaminate the solution or impede the convergence. This is particularly true of external flows where unphysical large values of effective viscosity in the free stream can "swamp" the boundary layers.

The turbulence specification methods described above can be used to enter uniform constant values instead of profiles. Alternatively, the turbulence quantities in terms of more convenient quantities such as turbulence intensity, turbulent viscosity ratio, hydraulic diameter, and turbulence length scale may be specified.

2.3.6.1 Turbulence Intensity

The turbulence intensity, I, is defined as the ratio of the root-mean-square of the velocity fluctuations, u', to the mean flow velocity, u_{avg}.

To match experimental values, inlet I at different Reynolds numbers was set as follows:

Table 2-3 Turbulence intensity

Re	*I*
7407	1.6%
29630	0.4%
59259	0.32%

2.3.6.2 Turbulent Viscosity Ratio

The turbulent viscosity ratio, μ_t/μ, is directly proportional to the turbulent Reynolds number ($Re_t = k^2/(\varepsilon v)$). The Re_t is large, on the order of 100 to 1000, in high-Reynolds-number boundary layers, shear layers, and fully-developed duct flows.

However, at the free-stream boundaries of most external flows, μ_t/μ is fairly small. Typically, the turbulence parameters are set so that $1 < \mu_t/\mu < 10$.

2.4 Heat Transfer around a Circular Smooth Surface Cylinder

2.4.1 Flow Properties

2.4.1.1 Velocity Distribution

The contours of velocity are shown plotted in **Figure 2-5**. It may be seen that, from the front stagnation point, the air velocity increases with θ and the maximum velocity occurs at $\theta \approx 80°$ (red area).

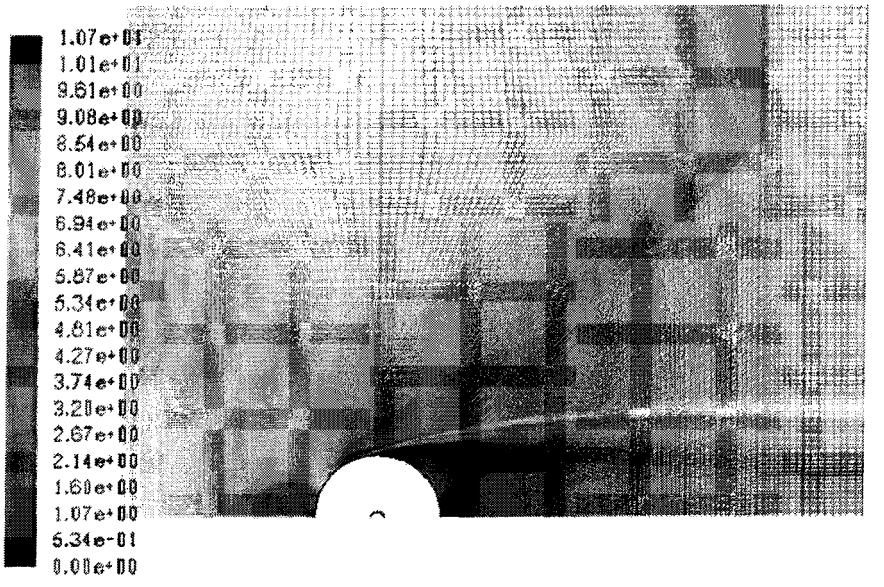

Figure 2-5 Contours of velocity at inlet velocity = 8m/s

2.4.1.2 Local Static Pressure

As shown in **Figure 2-6** and **Figure 2-7**, the free stream fluid is brought to rest at the frontal stagnation point, with an accompanying rise in pressure. From this point, the

pressure decreases with increasing η, the streamline coordinate, and boundary layer develop under the influence of a favorable pressure gradient ($dp/d\eta$ <0), where η is the streamwise coordinate measured along the surface. The pressure eventually reaches a minimum, however, and towards the rear of the cylinder, further boundary layer development occurs in the presence of an adverse pressure gradient ($dp/d\eta$ >0).

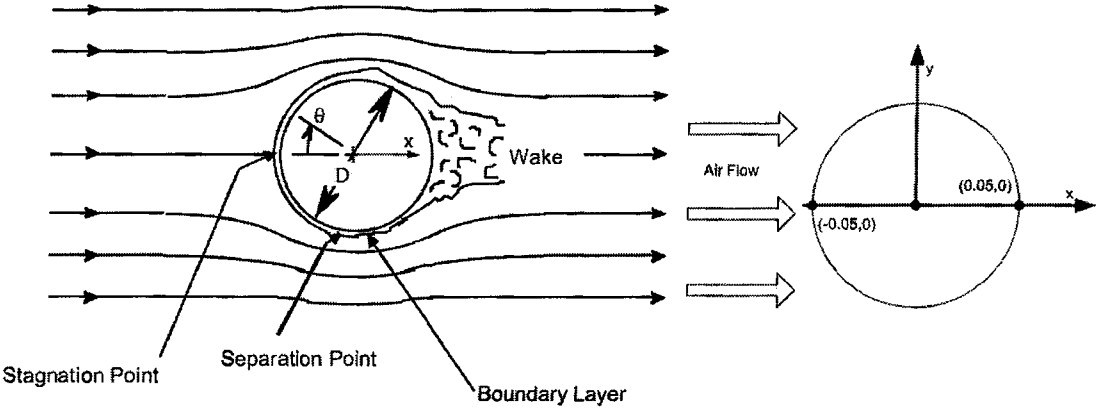

Figure 2-6 Sketch of the flow field around a cylinder in cross flow

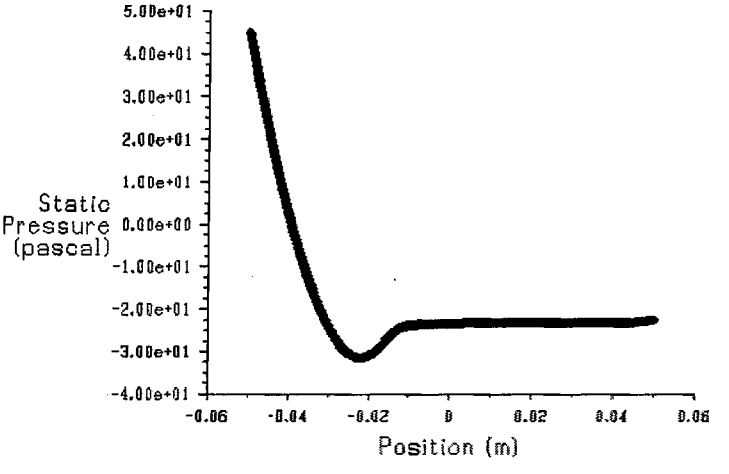

Figure 2-7 Static pressure distribution along sleeve surface at inlet velocity v = 8m/s (the origin coordinates are at the cylinder center point)

2.4.2 Local HTC Distribution

In general, all cases indicate the correct characteristic shape of the local Nusselt number (***Nu***) around the circular cylinder. In the subcritical range (***Re***$<10^5$), a local maximum of the ***Nu*** is located at or close to the stagnation point, and the ***Nu*** decreases when θ increases as a result of laminar boundary layer development. A minimum ***Nu*** is reached close to the top of the cylinder, at $\theta \approx 80°$, which is associated with separation. Moving further into the wake region, ***Nu*** increases with θ due to mixing associated with vortex formation (Incropera, 2007).

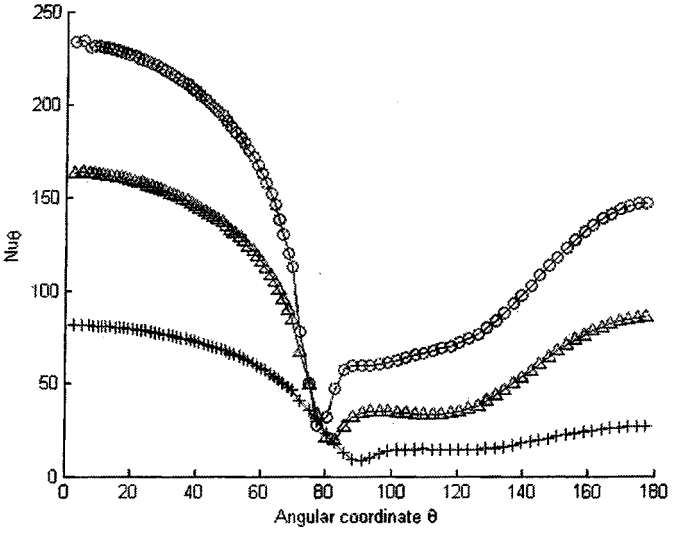

Figure 2-8 Local HTC at variable ***Re***: +, ***Re*** = 7407; Δ, ***Re*** = 29630; o, ***Re*** = 59259

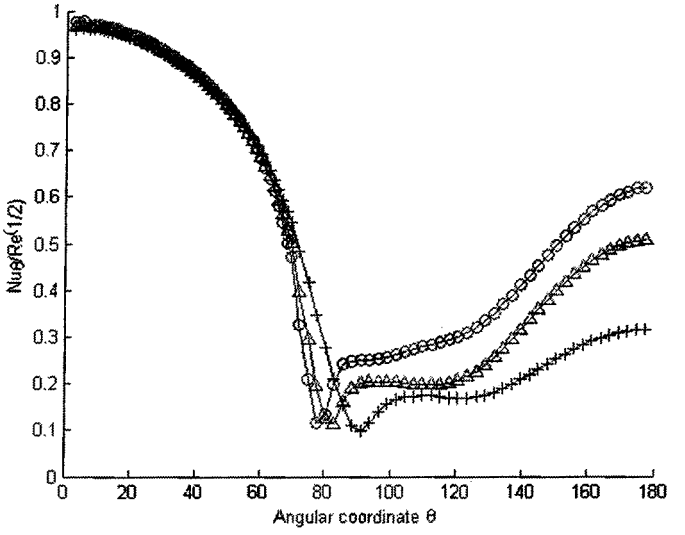

Figure 2-9 Local HTC at variable ***Re***: +, ***Re*** = 7407; Δ, ***Re*** = 29630; o, ***Re*** = 59259

Figure 2-8 and **Figure 2-9** show the ***Nu*** profile from the numerical results for the smooth surface cylinder, *i.e.* $K_s/d = 0$. The horizontal axis is a circumferential angle in degrees, where 0 degrees is the leading edge or front stagnation point of a cylinder, and 180 degrees is the trailing edge or rear. The diameter of the circular cylinder is 0.1m.

2.4.3 Overall HTC

The empirical equation from Hilpert is

$$\overline{Nu_D} \equiv \frac{\bar{h}D}{k} = CRe^{m}Pr^{1/3} \qquad \textbf{Equation 2-1}$$

where the constants C and m are listed in Table 2-4 for *Re* value ranges.

Table 2-4 Constants of **Equation 2-1**

Re_D	C	M
4000-40,000	0.193	0.618
40,000-400,000	0.027	0.805

Churchill and Bernstein have proposed a single comprehensive equation which is valid for a wide range of Reynolds numbers (Re_D) and Prandtl numbers. The equation is recommended for all $Re_D Pr > 0.2$ and has the form

$$\overline{Nu_D} = 0.3 + \frac{0.62 Re_D^{1/2} Pr^{1/3}}{[1 + (0.4/Pr)^{2/3}]^{1/4}} \left[1 + \left(\frac{Re_D}{28200}\right)^{5/8}\right]^{4/5} \qquad \textbf{Equation 2-2}$$

The assumed condition is that the surface temperature is 0°C and the ambient air temperature is 3°C. In Equation 2-1 and Equation 2-2, the air properties are evaluated at the film temperature of 1.5 degrees.

$$T_f = \frac{T_s + T_a}{2} \qquad \textbf{Equation 2-3}$$

where T_f is the film temperature, T_s is the surface temperature, and T_a is the air temperature.

Table 2-5 Overall average Nu for a circular cylinder

Air Velocity(m/s)	Reynolds Number	Nu(**Equation 2-1**)	Nu(**Equation 2-2**)	Nu(numerical)
1	7407	42.90	46.00	39.59
4	29630	101.04	101.06	86.46
8	59259	169.85	154.91	133.03

Table 2-5 compares the average Nusselt numbers obtained from empirical **Equation 2-1, Equation 2-2** and the numerical simulations. It may be observed that the numerical results are about 15% less than those obtained from the empirical equations. The reason for this discrepancy is that the simulations were carried out at a constant surface temperature, while most experiments were conducted in a constant heat flux from the surface.

Considering that mixtures of ice particles and water are produced during the snow melting process, it is therefore better to choose a model at a constant surface temperature of 0°C.

2.5 Local HTC Distribution for Rough Surface Cylinders

2.5.1 Roughness of Snow

The roughness of a snow surface is caused by wind, uneven evaporation, or uneven melting. Lacroix *et al.* (2008) investigated snow pack and found that the roughness of snow varied largely as a result of weather and geographical conditions. Even for relatively smooth surfaces, the classical roughness parameters are found to be in the 0.5-9.2 mm range for the RMS height distribution. For more detailed information on the rough surface effects, a set of values is listed in **Table 2-6.**

To model the wall roughness effects, two roughness parameters must be specified: the Roughness Height, K_s, and the Roughness Constant, C_{Ks}. The default roughness height (K_s) is zero, corresponding to smooth walls. For snow types of roughness, it is recommended that an "equivalent" sand-grain roughness height should be used for K_s.

Choosing a proper roughness constant (C_{Ks}) is dictated mainly by the type of the given roughness. The default roughness constant ($C_{Ks} = 0.5$) was recommended by FLUENT to simulate for uniform sand-grain roughness and computation convergence.

The roughness factor, r is defined as ratio of roughness height, K_s and the diameter of snow sleeve, D and shown in **Table 2-6**. The diameter of snow sleeve is assumed as 0.1 m in this study.

$$r = \frac{K_s}{D} \qquad \textbf{Equation 2-4}$$

Table 2-6 Roughness parameters

K_s (m)	D (m)	r ($\times 10^{-3}$)
0.000075	0.1	0.75
0.00009	0.1	0.9
0.0001	0.1	1
0.0005	0.1	5
0.001	0.1	10
0.002	0.1	20
0.003	0.1	30
0.004	0.1	40

2.5.2 Pressure Distribution

The local static pressure distribution around the circumference of a rough cylinder is shown in **Figure 2-10**. The static pressure was plotted against the angle from the front stagnation point, while the Reynolds number appears as a parameter. The pressure is normalized by the following equation.

$$P_e = \frac{P - P_\infty}{\frac{\rho}{2} u_\infty^2} \qquad \textbf{Equation 2-5}$$

For subcritical flow conditions, the pressure minimum is located at about $\theta = 70°$ and it decreases with increasing ***Re***.

Figure 2-11 represents the pressure distribution at a constant Reynolds number for variable roughness parameters. It may be found that the lower roughness ($r < 9\times10^{-3}$) does not affect the pressure distribution. The maximum value of the adverse pressure increases obviously when the roughness is greater than 9×10^{-3}.

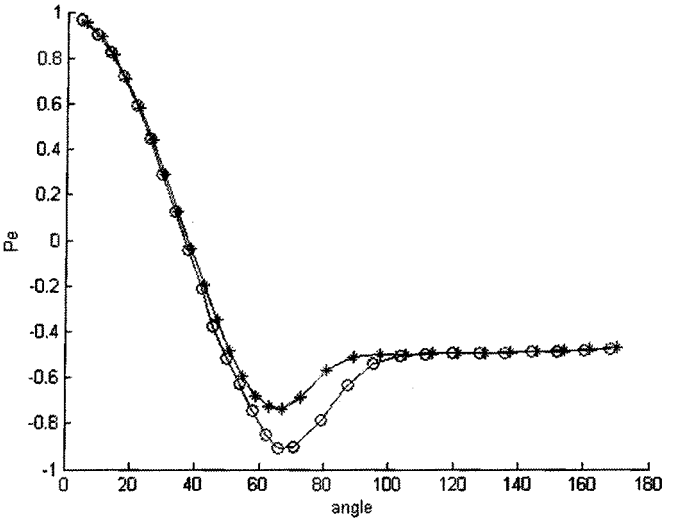

Figure 2-10 Local static pressure distribution at $r = 3\times10^{-3}$ and variable ***Re*** parameter. *, ***Re*** = 7104; o, ***Re*** = 22222

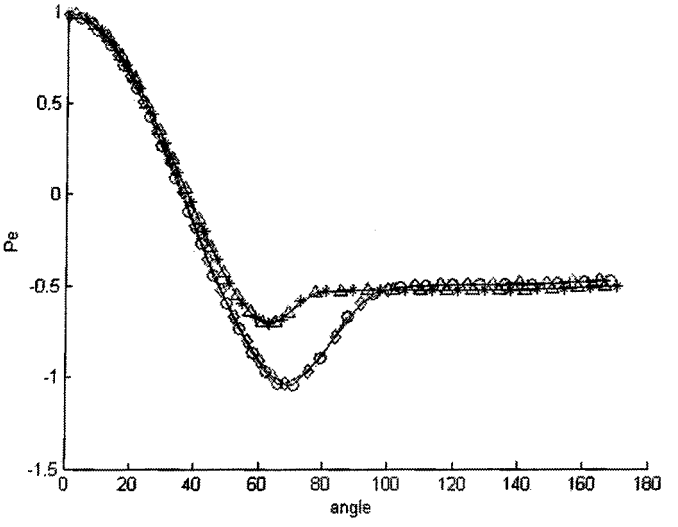

Figure 2-11 Local static pressure distribution at $Re = 6.67\times10^4$ and variable roughness parameter. *, $r = 0$, smooth surface; Δ, $r = 2\times10^{-3}$; o, $r = 11\times10^{-3}$; ◊, $r = 15\times10^{-3}$

2.5.3 Local HTC Distribution

In **Figure 2-12**, **Figure 2-13**, and **Figure 2-14**, the local heat-transfer distribution around a cylinder was plotted for each Reynolds number. The varied parameter here is surface roughness. The Nusselt number is normalized by $Re^{-1/2}$.

Figure 2-12 shows the results for the smallest Reynolds number, $Re = 7407$. It may be seen that most of the effects caused by surface roughness occur in the wake range of the air flow. Even at the highest roughness value, $r = 50\times10^{-3}$, the minimum Nu is still at almost the same position as it is for a smooth surface.

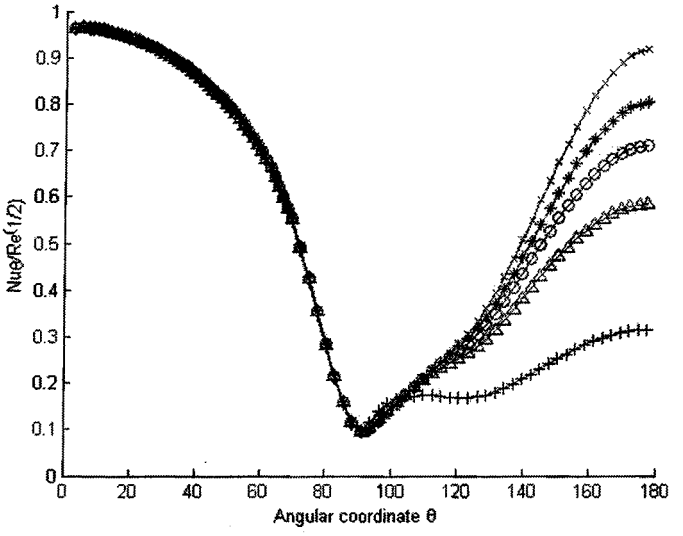

Figure 2-12 Local HTC at ***Re*** = 7407 and variable roughness parameter. +, ***r*** = 0, smooth surface; Δ, ***r*** = $10*10^{-3}$; o, ***r*** = 30×10^{-3};*, ***r*** = 40×10^{-3}; x, ***r*** = 50×10^{-3}

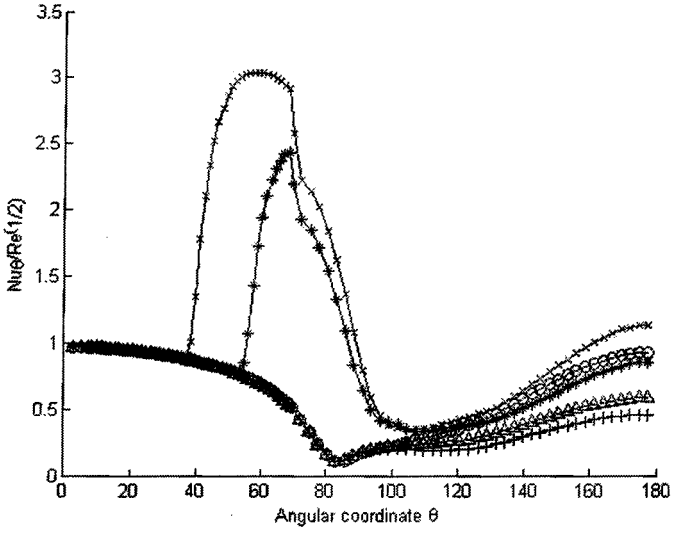

Figure 2-13 Local HTC at ***Re*** = 2.2×10^{4} and variable roughness parameter. +, ***r*** = 0, smooth surface; Δ, ***r*** = 12×10^{-3}; o, ***r*** = 20×10^{-3}; *, ***r*** = 30×10^{-3}; x, ***r*** = 35×10^{-3}

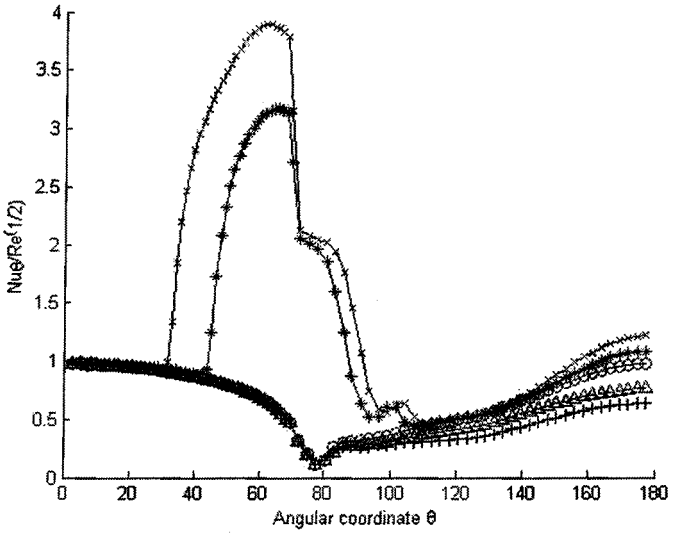

Figure 2-14 Local HTC at $Re = 6.67\times10^4$ and variable roughness parameter. +, $r = 0$, smooth surface; Δ, $r = 3\times10^{-3}$; o, $r = 9\times10^{-3}$;*, $r = 12\times10^{-3}$; x, $r = 15\times10^{-3}$

Figure 2-13 exhibits the results for a higher Reynolds number, Re = 22222. In a lower roughness range $r < 2\times10^{-2}$, the curves have similar shape characteristics: the boundary layer is laminar throughout, and its separation is indicated by a minimum near $\theta = 80°$.

When the curve is associated with a higher roughness value, $r = 30\times10^{-3}$ is compared to the one with a smooth surface and the difference is largely apparent. There is a direct transition from the laminar to the turbulent boundary layer at 50° which generates high heat transfer coefficients downstream because the heat transfer in the turbulent flow is more effective than in the laminar flow. In the turbulent region, Nu increases with increasing θ until it reaches its maximum value at around $\theta \approx 70°$, and then decreases. The separation occurs at $\theta \approx 110°$. The curve $r = 35\times10^{-3}$ shows similar behavior with the exception of the

fact that the transition point is at $\theta \approx 40°$ and the peak value of the Nusselt number is approximately 23% higher.

Figure 2-14 qualitatively shows similar results for the local heat transfer at $Re = 66667$. Comparing **Figure 2-14** and **Figure 2-13**, it may be observed that as the roughness parameter increases, the laminar-turbulent transition occurs at a decreasing Re. These results are consistent with Achenbach's experiments (1977).

The values of heat transfer at the front stagnation point would be expected to be equal to unity, considering that the flow near the stagnation point is laminar. Some experimental results are greater than unity mainly because of the limitations of laboratory equipment.

At a given Reynolds number, it may be observed that:

- the greater the roughness, the closer the laminar-turbulent transition point approaches the front stagnation point;
- the peak value of Nu increases upon increasing the roughness parameter;
- the location of the Nu peak value moves closer to the front stagnation point with increasing roughness;
- the heat transfer within the wake region increases with increasing roughness.

2.5.4 Total Heat Transfer

Figure 2-15 exhibits the overall average Nusselt numbers at different roughness values. It can be seen that the total heat-transfer increases with the surface roughness. After the

roughness parameter exceeds a critical value, heat transfer increases more intensely. But, at a lower ***Re***, there is no such critical value while $r < 0.05$.

Table 2-7 Overall average Nusselt number

Roughness r ($\times 10^{-3}$)	***Re*** = 7407	***Re*** = 22222	***Re*** = 66666
0	47.60	85.91	161.45
3			170.11
9		90.22	182.21
10	52.19		242.26
11			286.61
12		90.33	326.83
15			429.46
18			514.65
20		99.7	
25		98.99	
30	53.86	139.58	
35		199.98	
40	54.98		
50	56.32		

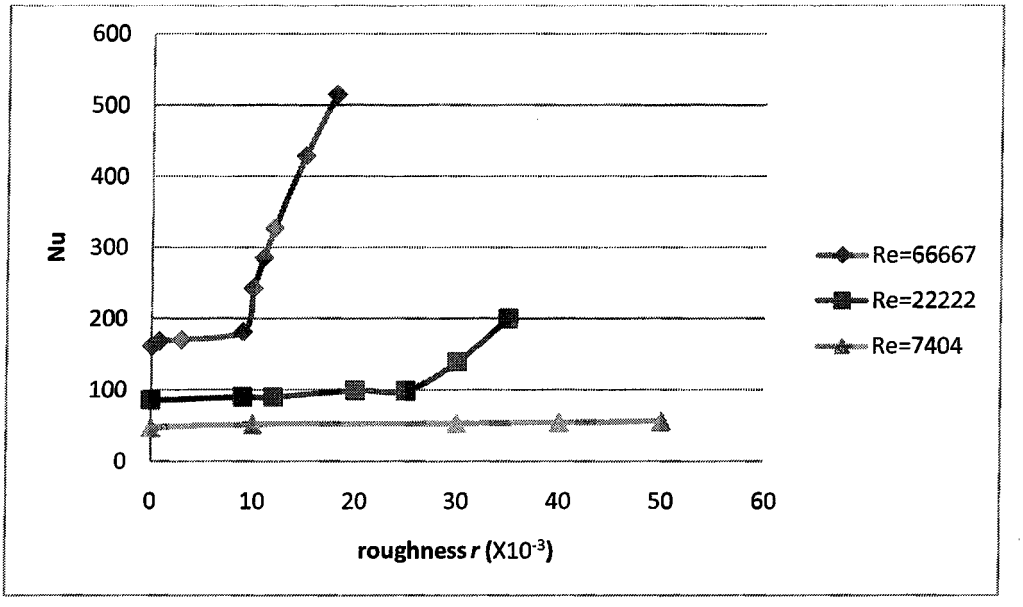

Figure 2-15 Overall average HTC at variable roughness

2.6 Local HTC Distribution for an Elliptical Cylinder

2.6.1 Elliptical Cylinder: Definition

An ellipse is a smooth closed curve which is symmetric about its center. The distance between antipodal points on the ellipse, that is to say the pair of points whose midpoint is at the center of the ellipse, with a maximum and minimum along two perpendicular directions, namely the major axis, or transverse diameter, and the minor axis, or conjugate diameter, respectively. The semi-major axis or major radius, denoted by ***a*** in **Figure 2-16**, and the semi-minor axis or minor radius, denoted by ***b*** in **Figure 2-16**, are one half of the major and minor diameters, respectively.

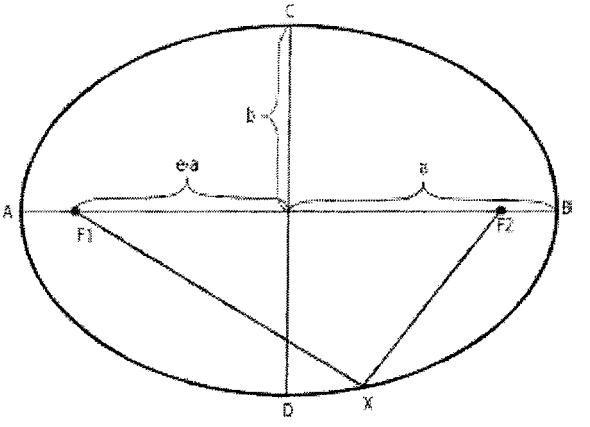

Figure 2-16 Definition of ellipse

1. The eccentricity of the ellipse is

$$e = \sqrt{1 - \left(\frac{b}{a}\right)^2} \qquad \textbf{Equation 2-6}$$

2. The flatness ratio is defined as

$$f = \frac{b}{a} \qquad \textbf{Equation 2-7}$$

3. The area enclosed by the ellipse is

$$A = \pi ab \qquad \textbf{Equation 2-8}$$

where ***a*** and ***b*** are one-half of the major and minor axes of the ellipse, respectively.

Circumference

The circumference ***C*** of an ellipse is $4aE(\varepsilon)$, where the function ***E*** is the complete elliptic integral of the second kind. A good approximation of circumference is Ramanujan's equation:

$$C \approx \pi\left[3(a+b) - \sqrt{(3a+b)(a+3b)}\right] \qquad \textbf{Equation 2-9}$$

2.6.2 Snow Sleeve Deformation

It is customarily assumed that the cross section of the snow sleeve remains constant during the snow melting process. The deformation factor may thus be defined as

$$d = \frac{\Delta l}{R} \qquad \textbf{Equation 2-10}$$

where $\boldsymbol{R}$ is the radius of the circular cylinder and $\Delta \boldsymbol{l}$ is the variation length for the semi-minor radius of the ellipse.

Therefore, it is possible to obtain the semi-minor radius by

$$b = R \times (1 - d) \qquad \textbf{Equation 2-11}$$

and the semi-major radius by

$$a = A/(\pi \times a) \qquad \textbf{Equation 2-12}$$

The parameters of a set of ellipses are listed in **Table 2-8**. From this, it is clear that the perimeter of an ellipse increases with its eccentricity.

It should be noted that snow sleeve becomes deformed as a bluff shape, *i.e.* when the minor axis is perpendicular to the flow.

Table 2-8 Ellipse parameters

Deformation	Circle			Ellipse				
	Radius	Area	Perimeter	*a*	*b*	Perimeter	Eccentricity	*b/a*
1%	0.05	0.0079	0.31	0.0505	0.0495	0.3140	0.20	0.98
2%	0.05	0.0079	0.31	0.0510	0.0490	0.3141	0.28	0.96
3%	0.05	0.0079	0.31	0.0515	0.0485	0.3142	0.34	0.94
4%	0.05	0.0079	0.31	0.0521	0.0480	0.3144	0.39	0.92
5%	0.05	0.0079	0.31	0.0526	0.0475	0.3146	0.43	0.90
6%	0.05	0.0079	0.31	0.0532	0.0470	0.3149	0.47	0.88
7%	0.05	0.0079	0.31	0.0538	0.0465	0.3152	0.50	0.86
8%	0.05	0.0079	0.31	0.0543	0.0460	0.3156	0.53	0.85
9%	0.05	0.0079	0.31	0.0549	0.0455	0.3161	0.56	0.83
10%	0.05	0.0079	0.31	0.0556	0.0450	0.3166	0.59	0.81
20%	0.05	0.0079	0.31	0.0625	0.0400	0.3257	0.77	0.64
30%	0.05	0.0079	0.31	0.0714	0.0350	0.3440	0.87	0.49

2.6.3 Local HTC Distribution

Figure 2-17, **Figure 2-18**, and **Figure 2-19** show the numerical results for a set of elliptical cylinders. The parameter varied here is ellipse eccentricity, and the ***Nu*** is normalized by $Re^{-1/2}$.

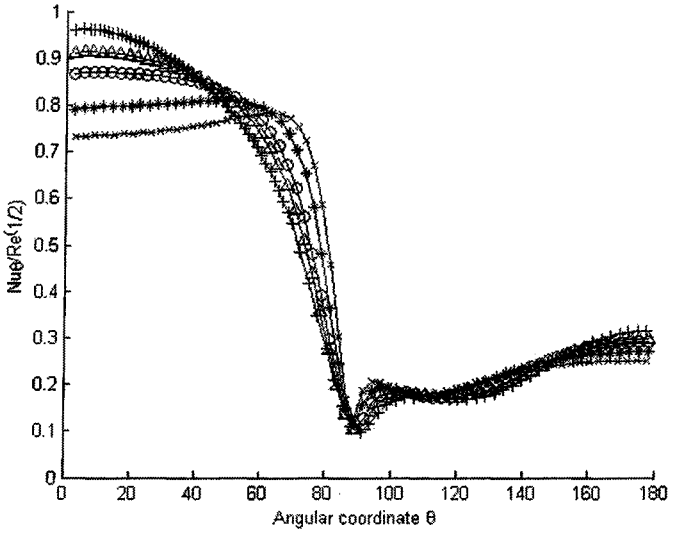

Figure 2-17 Local HTC at ***Re*** = 7407 and variable eccentricity parameter. +, ***e*** = 0; Δ, ***e*** = 0.43; o, ***e*** = 0.59; *, e = 0.77; x, ***e*** = 0.87

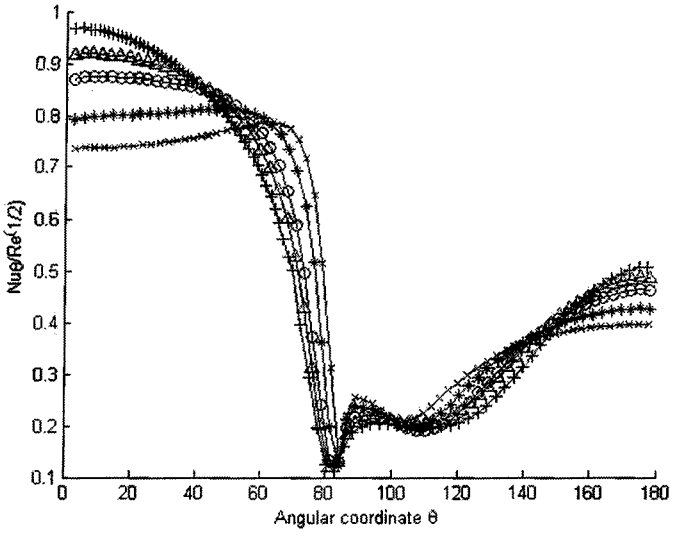

Figure 2-18 Local HTC at ***Re*** = 29630 and variable eccentricity parameter. +, ***e*** = 0; Δ, ***e*** = 0.43; o, ***e*** = 0.59; *, ***e*** = 0.77; x, ***e*** = 0.87

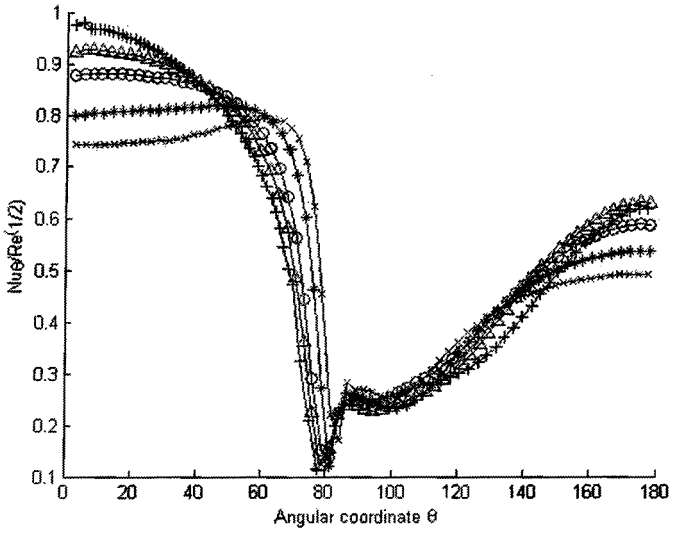

Figure 2-19 Local HTC at ***Re*** = 59259 and variable eccentricity parameter. +, ***e*** = 0; Δ, ***e*** = 0.43; o, ***e*** = 0.59; *, ***e*** = 0.77; x, ***e*** = 0.87

Figure 2-17 shows the results associated with the smallest Reynolds number, ***Re*** = 7407. The curves have a similar shape when the deformation factor is less than 10%: the maximum ***Nu*** is near the front stagnation point, and the separation point is at approximately $\theta = 80°$.

It may be observed that the ***Nu*** value near the front stagnation point decreases with the increasing eccentricity of the ellipse, *i.e.* with the increase in deformation. For a higher deformation range (factor > 10%), the maximum ***Nu*** occurs at about $\theta = 70°$ which is close to the separation point.

The major reason for this divergence is the difference in geometry between the circle and the ellipse. The curvature of an ellipse is not uniform along its boundary, thus at $\theta = 0°$, near the front stagnation point, or at $\theta = 180°$, the curvature has a minimum value; whereas

at $\theta = 90°$ or $\theta = 270°$, the curvature reaches its maximum value. Also, the perimeter of an ellipse is longer than that of a circle. Thus, at $\theta = 0°$, an elliptical cylinder shows more analogical features with a plate which is perpendicular to the air flow, than does a circular cylinder. Furthermore, at the higher eccentricity, the smaller curvature is at $\theta = 0°$. Therefore, the value of Nu at $\theta = 0°$ decreases as the eccentricity increases.

In the wake region, the air flow is full of vortices and does not have a direction going towards unity. The effects occurring there are much less important than those occurring in the laminar boundary layer.

At a given Reynolds number, it will also be found that:

- the separation point moves downward with increasing eccentricity values;
- the value of Nu at the separation point increases as the eccentricity increases.

Baevay *et al.* (1997) proposed a theoretical analysis of the heat transfer from a moving elliptical cylinder, although the Péclet number used in the paper is less than 2.5 which is too small for snow sleeve issues. Furthermore, a number of similar characteristics may be found between **Figure 2-20** and **Figure 2-17** : thus lower values locate at $\theta = 0°$ and maximum values at approximately $\theta = 70°$.

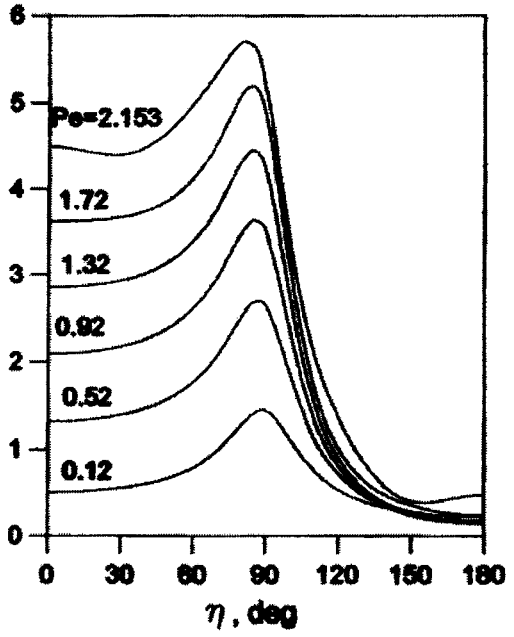

Figure 2-20 Heat-flux distributions obtained for flatness ratio = 0.25 and various Péclet numbers

2.6.4 Overall Heat Transfer

Zukauskas *et al.* (1985) reported on the external heat transfer for a single elliptical cylinder in cross-flow. These authors focused their investigation on an elliptical cylinder whose flatness ratio was 0.52. The cylinder was aligned with the major axis both parallel and perpendicular to the flow. They proposed a correlation that described the average external heat transfer for elliptic cylinders as:

$$Nu_{dl} = 0.27 Re_{dl}^{0.6} Pr^{0.37} \left(\frac{Pr}{Pr_w}\right)^{0.25} \qquad \textbf{Equation 2-13}$$

where Nu_{dl} is the overall average Nusselt number, Pr and Pr_w are the Prantdl numbers of air and air near the wall, respectively. For the bluff elliptical body flow, dl is twice the major axis.

This correlation was derived for the boundary condition of uniform heat flux (UHF) and is valid over the $2\times10^4 \leq Re_{dl} \leq 2\times 10^5$ range.

Harris *et al.* (2002) carried out experiments in a wind tunnel and reported results for flatness ratios 0.20, 0.31, and 0.52, in addition to incidence angles of 0, 45, and 90 degrees.

Flatness ratios of less than 0.80, however, imply enormous deformation in snow sleeves which would not otherwise occur in reality. Nevertheless, it is still a satisfactory way of verifying the validity of numerical methods by comparing results.

From **Equation 2-13**, it is possible to obtain the Nusselt number Nu_{ell} for an elliptical cylinder at a flatness ratio of 0.52, which is about 92% of that for a circular cylinder. From **Table 2-9**, the numerical results for an elliptical cylinder at a flatness ratio of 0.49 (e = 0.87) shows that the ratio is approximately 95%, a little higher than Zukauskas's data.

Table 2-9 ***Nu*** for circular and elliptical cylinder

Re	$e = 0$	$e = 0.87$	Ratio
7407	39.59	37.69	95%
29630	86.46	83.01	96%
59259	133.03	126.22	94%

Figure 2-21 and **Table 2-10** show the overall heat transfer around the elliptical cylinder. It may be observed that the heat transfer coefficient stays almost constant as eccentricity is less than 0.8, but this decrease accelerates for higher ***Re*** of 59259 as eccentricity becomes greater than 0.8.

Table 2-10 Overall HTC at variable Reynolds number

e	0	0.09	0.20	0.28	0.34	0.39	0.43	0.59	0.77	0.87
Re = 7407	39.59	39.60	39.58	39.55	39.53	39.39	39.40	39.21	38.53	37.69
Re = 29630	86.46	85.88	85.95	85.91	86.37	86.08	86.77	85.68	84.39	83.01
Re = 59259	133.0	133.7	132.9	132.5	132.2	133.9	133.2	134.0	128.7	126.2

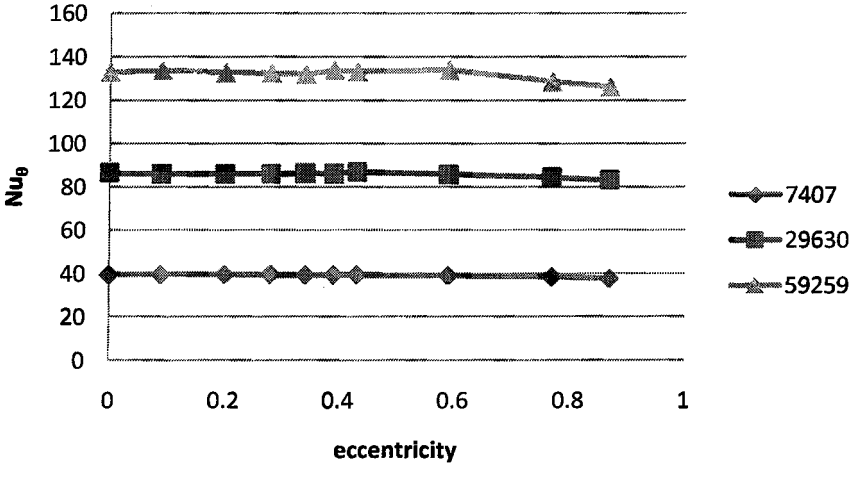

Figure 2-21 Overall HTC at variable Reynolds number

2.7 Conclusions

A numerical study of forced convection around a snow sleeve in a cross flow of air was conducted by using the computational fluid dynamic (CFD) software FLUENT. This investigation was carried out (i) into the effects of the special characteristics of a snow sleeve, including surface roughness and the non-circular shape, (ii) into the local HTC distribution, and (iii) into the overall HTC under different wind conditions.

The computational results show satisfactory concordance with the theoretical analyses and experimental data reported in the relevant literature from this domain.

CHAPTER 3

THE EQUIVALENT THERMAL CONDUCTIVITY OF SNOW SLEEVE ON OVERHEAD TRANSMISSION LINES

3.1 Introduction

Heat transfer within snow is one of the most essential processes characterizing a variety of snow properties, thus playing an important role in snow technology and science. For example, when an attempt is made to remove a snow sleeve from overhead cables, thermal conductivity is one of the key factors in determining the quantity of electric current required for this purpose.

For snow, which is composed of variously textured substances in different states, as shown in **Figure 1-4**, heat transfer by conduction may occur in several forms. Its thermal characteristics depend upon a variety of such factors as thermal conductivity of constituent phases, shape and size of snow grain, temperature, and so forth. The complexity of these factors presents a challenge to the research in the equivalent thermal conductivity of dry snow.

Snow may be regarded as a kind of multi-composition medium and several models have already been developed to study the equivalent thermal conductivity of snow. A microstructure model, however, provides a conceptual understanding of snow structure and takes into account the influence of geometry on snow grain and the connection bond.

The residual water in wet snow tends to produce a number of effects including heat transfer by water movement, thus making it more complex to estimate the equivalent conductivity of wet snow than dry snow. It should be mentioned here that only dry snow has been modelled for this study.

The aims of this research are:

1. to develop a microstructure model to estimate the equivalent thermal conductivity of dry snow;
2. to analyze the dependence of thermal conductivity on snow microstructure and other factors such as temperature and vapor;
3. to establish the relationship between the snow conductivity model and the weather;
4. to validate the microstructure model experimentally.

3.2 Review of the Literature

The equivalent thermal conductivity of snow can be determined either experimentally or mathematically.

3.2.1 Experimental Measurements

The first formal measurement of the thermal conductivity of snow dates back to at least 1886 (Andrew, 1886). Pitman *et al.* (1966) and Sturn *et al.* (1997) demonstrated in detail the method and devices for measuring the thermal conductivity of snow. **Figure 3-1** shows measurement data of the snow thermal conductivity. Abel's regression equation (1893) has been superimposed on the data in **Figure 3-1** for comparison purposes. **Figure 3-2** shows a part of the published empirical relationship between snow density and thermal conductivity.

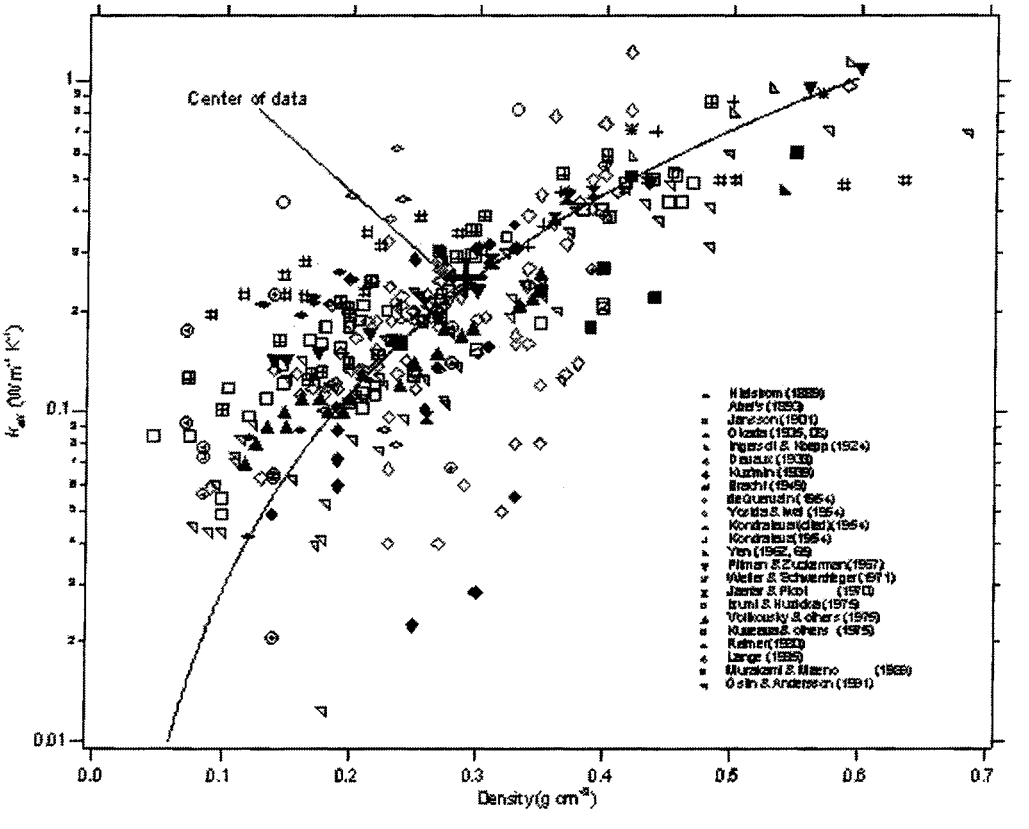

Figure 3-1 Measurement of the thermal conductivity of snow. Abel's regression equation (1893) is superimposed on the data for reference (Sturn *et al.* 1997)

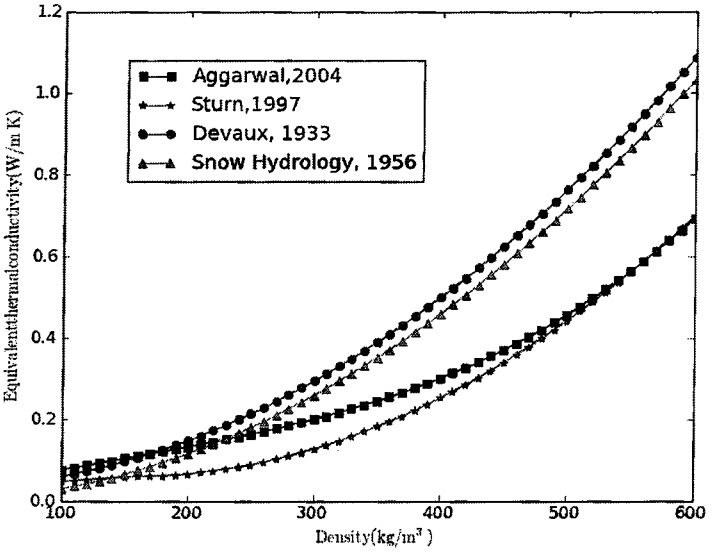

Figure 3-2 The published relationship between snow density and thermal conductivity. □, Aggarwal 2004; *, Sturn *et al.* 1997; o, Devaux 1933; Δ, Snow Hydrology 1956.

3.2.2 Mathematical Models

Two kinds of mathematical models were developed to predict the equivalent thermal conductivity of dry snow.

1. Multi-Component Model

The Krischer model is popularly applied to estimating the equivalent thermal conductivity of porous media. Krischer's model recognizes that there are two extremes in thermal conductivity values, one derived from the parallel model and the other derived from the series model, while the real value of thermal conductivity should be located somewhere in between these two extremes. A conceptual diagram is provided in **Figure 3-3**.

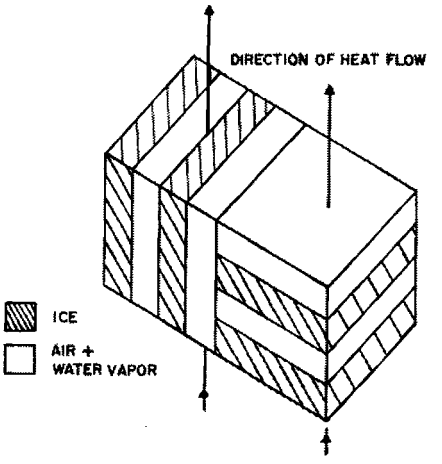

Figure 3-3 Schematic of two types of unit cell in Krischer's model

Pitman *et al.* (1966) proposed a model and applied it to dry snow research. The Pitman model is similar to the Krischer model, with the essential difference between the two models being the parameter which accounts for the moisture and density.

2. Microstructure Models

Under a certain set of assumptions, the microstructure models take into account the effects from the geometry of snow grains and the connection bond.

Pitman *et al.* (1966) proposed a modified Woodside model (1961) to estimate the equivalent conductivity of snow. The Pitman model allows for conduction through continuous ice paths.

Verma *et al.* (1991) proposed a two-dimensional resistor model to obtain an expression for predicting the equivalent thermal conductivity. The snow grains were assumed to be

spherical particles and located at the corners of a simple cube side. This model is essentially identical to the microstructure approach.

Satywali *et al.* (2008) proposed a three-dimensional model which includes different geometrical shapes influencing the thermal conductivity of snow. This geometrical model has been assumed to comprise unit cells having solid (ice) inclusion which are spherical, cylindrical, and cubical in shape with vertical connections arranged in a cubic packing.

3.2.3 Discussion

In previous investigations, it was usually assumed that the equivalent thermal conductivity is almost independent of temperature and other snow properties except density, *i.e.* snow conductivity is presented as a function of snow density. The research also shows that the value of the snow thermal conductivity increases with density.

These observed data pertaining to thermal conductivity vary over wide ranges. Most of the scatter is the result of a natural variation in the thermal conductivity of the snow, and is thus a direct consequence of variations in the microstructure of snow. The scatter is also the result of tests which were carried out over a large range of temperatures.

Recently, more research has focused on the microstructure of snow. Several papers estimate snow conductivity by setting up a two-dimensional or three-dimensional ice-particle grid.

3.3 Thermal Conductivity of Snow

Dry snow may be regarded as a multi-phase system. As the temperature changed, the snow exhibits a complicated dynamic complex of three fractions, continuously changing their ratios: ice particles, water and gaseous phase (including air and water vapor). Thus, the heat transport of snow is more complicated than it is for that of a single-phase substance. Thermal transport in snow has three main components:

1. conduction through the ice lattice;
2. conduction through the air in the pore spaces;
3. latent heat transport across the pore spaces due to vapor sublimation and condensation.

These mechanisms of heat transport are generally combined into a single value (k_e):

$$q = -k_e \frac{dT}{dX} \qquad \textbf{Equation 3-1}$$

Radiation and convection, which are the other two heat transport mechanisms, can also operate but are not significant in the context of thermal conductivity measurements. For common snow temperature and pore sizes, radiation transfers is several orders of magnitude of less heat than other mechanisms.

Certain difficulties arise when apportioning the total heat transfer into transport mechanism since the thermal and water vapor pressure gradients in snow are coupled and depend on the microstructure, thus making it difficult to quantify. The ice matrix, namely

grains and necks, is about 100 times more conductive than the air in the pore spaces. Since this ice matrix provides a much better thermal pathway than the pore spaces, temperature gradients across the pore spaces are enhanced when compared to those in the ice matrix (de Quervain, 1972). Such an enhancement also increases the vapor pressure gradients and hence the transport of water vapor. The associated transport of latent heat also increases. Simultaneously, the ice matrix has a blocking effect which limits vapor movement to the pore spaces. The balance between these contradictory processes (high thermal conductivity but low temperature gradients *vs.* low thermal conductivity but high gradients; blocking *vs.* enhancement) is a function of grain and pore configuration and size, as well as the temperature gradients imposed on the snow.

Based on an elegant experiment, De Quervain (1958) estimated that the ice matrix for his snow samples carried 55-60% of the heat, the rest moving across the pores as sensible or latent heat. Reviewing the literature on vapor diffusion in snow, Colbeck (1993), concluded that about 30-40% of the heat is transported by vapor considering that the vapor gradient enhancement predominates over the blocking effect of the ice matrix.

The equivalent thermal conductivity of dry snow depends on several factors.

- Density of snow

  The density of snow indicates the porosity because the density of air (1.29 kg/m^3 at 0°C) is observably less than that of ice (800-900 kg/m^3).

- Snow temperature

  Firstly, the temperature affects the conductivity of enclosed air and ice; secondly, it

affects the quantity of water vapor within the snow.

- Microstructure
    - Grain size and shape

Snow grains display several shapes including spheres, cylinders or cubes, depending on the weather conditions.

- The average contact area between grains

Normally, snow grains are compacted by each other when they accumulate around a cable. Increased contact areas result in higher conductivity of the ice matrix.

3.4 Snow Component Properties

Dry snow can be described as a porous medium consisting of air and two water phases, namely ice and vapor. The ice phase consists of an assemblage of grains which are initially arranged in a random but load-bearing skeleton. This assemblage is termed the ice matrix. The ice matrix is surrounded by the ambient air, subject to being separated into a dry air component and water vapor.

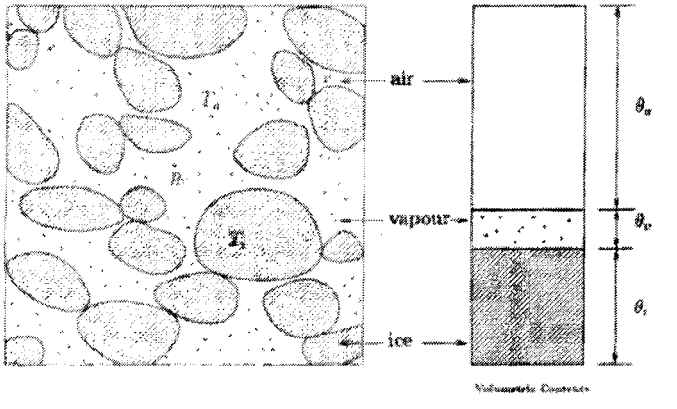

Figure 3-4 Schematic view of snow consisting of ice crystals, water vapor, and air for a density of 300 kg/m^3

1. Density

Snow density generally ranges from 100 to 500 kg/m^3 while light powdery snow is around 100 kg/m^3 and heavy wet snow is usually 500 kg/m^3. The density of ice is assumed to be 900 kg/m^3.

2. The Conductivity of Ice

The thermal conductivity in W/m°C of pure ice, k_i, is known as a function of temperature in °C, T, in and can be obtained by the following empirical equations:

$$k_i = 2.2196 - 6.248 \times 10^{-3}T + 1.0154 \times 10^{-4}T^2 \qquad \textbf{Equation 3-2}$$

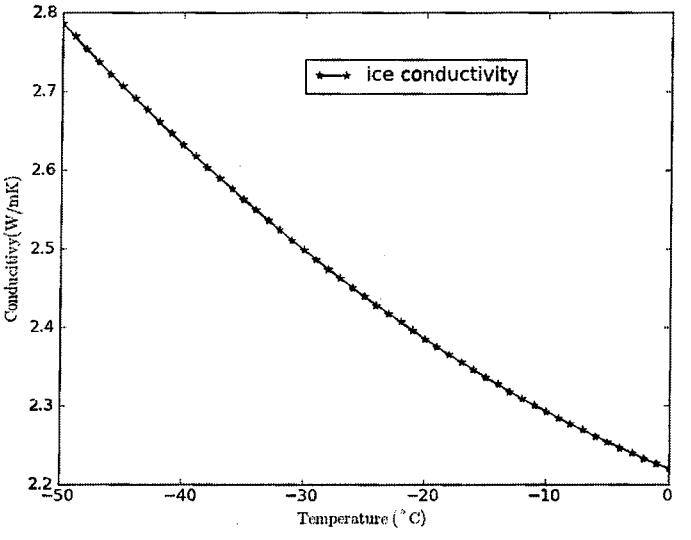

Figure 3-5 Conductivity of ice with respect to temperature

It may be observed that the conductivity of ice decreases as the temperature increases in **Figure 3-5**. Even at 0° C, the conductivity of ice is 50 times greater than that of saturated moist air.

3. The Conductivity of Dry Air and Saturated Moist Air

The conductivity of dry air k_a (W/m K) can be obtained as:

$$k_a = -3.9333 \times 10^{-4} + 1.10184 \times 10^{-4} T_a - 4.8574 \times 10^{-8} T_a^2 + 1.5207 \times 10^{-11} T_a^3 \quad \textbf{Equation 3-3}$$

where T_a is the temperature of dry air (K).

Based on Adams *et al.* (1993), the equivalent thermal conductivity for saturated moist air k_g can be written as:

$$k_g = k_a + \frac{DP_v L^2}{R_a^2 T^3} \quad \textbf{Equation 3-4}$$

where D is the diffusion coefficient of water vapor in air (2.02×10^{-5}), P_v is the saturation water vapor pressure over an ice surface, L is the latent heat of sublimation (2.838×10^6 J/kg), R_a is the specific gas constant (286.9 J/kg K), and T is the average temperature of water vapor (K).

The saturation vapor pressure P_v (Pa) over ice can be calculated through the Goff-Gratch equations:

$$P_v = 100 \times e_0 \times 10^X$$
$$X = a\left(\frac{T_0}{T} - 1\right) + b \log_{10} \frac{T_0}{T} + c\left(1 - \frac{T}{T_0}\right) \quad \textbf{Equation 3-5}$$

where

Item	Value
a	-9.09718

b	-3.56654
c	0.876793
e_0	6.1071 mb
T_0	273.16 K

The conductivity of saturated moist air and dry air are shown in **Figure 3-6**. It may be seen that the conductivity of saturated moist air and dry air increases as the temperature increases. The conductivity of saturated moist air (0.047) is almost twice as high as that of dry air (0.024) at 0° C. At -50° C, however, the difference between the conductivity of dry air (0.020083) and saturated moist air (0.020353) can be disregarded.

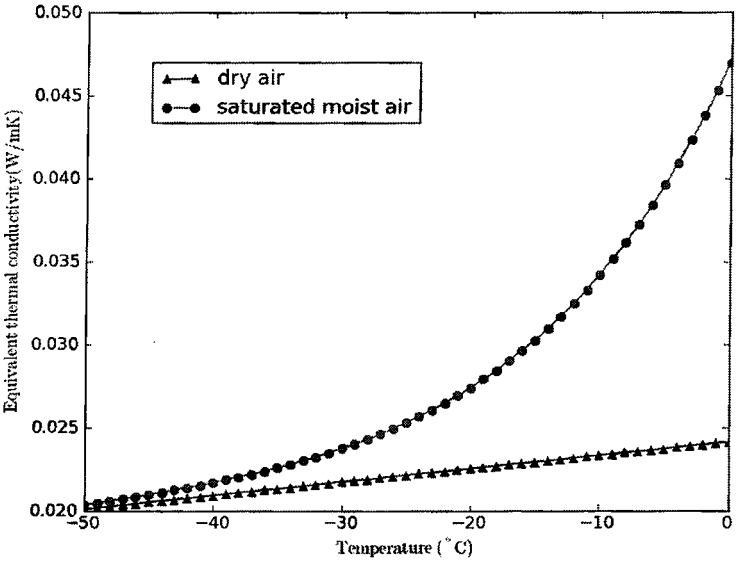

Figure 3-6 Thermal conductivity of pure air and gas. Δ, dry air; o, saturated moist air

4. The Density of Air and Saturated Moist Air

The density of dry air can be obtained by the following equation:

$$\rho_a = \frac{P_a}{R_a T_a} \qquad \textbf{Equation 3-6}$$

where P_a is the air pressure (assumed 101325 Pa here), R_a is the specific gas constant (286.9 J/kg K), and T_a is the temperature of air (K).

The density of water vapor may be obtained in a similar way:

$$\rho_v = \frac{P_v}{R_v T_v} \qquad \textbf{Equation 3-7}$$

where P_v is the saturation water vapor pressure (calculated through **Equation 3-5**), R_v is the specific gas constant of water vapor (462 J/kg K), and T_v is the temperature of water vapor (K).

The density of saturated moist air is the sum of the density of air and the water vapor.

$$\rho_g = \rho_a + \rho_v \qquad \textbf{Equation 3-8}$$

The density of saturated moist air and dry air is plotted in **Figure 3-7**. It is obvious that the difference between dry air and saturated moist air is negligible and that the density of saturated moist air decreases with increasing temperatures.

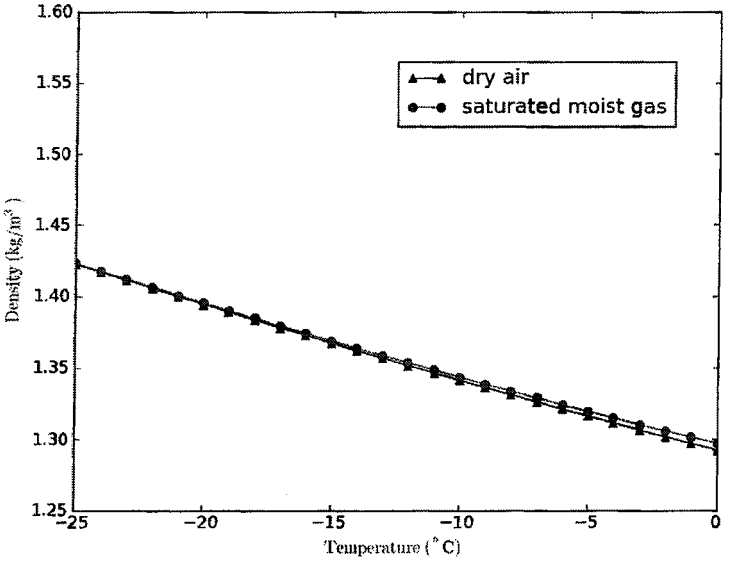

Figure 3-7 Density of air and saturated moist air varies with temperature. ∆, dry air; o, saturated moist air

3.5 Thermal Conductivity Model Development

For the purposes of this study, one micro-structural model was proposed for snow.

1. Parameters

The porosity of snow ϕ as defined below

$$\emptyset = \frac{V_a}{V_s} \qquad \textbf{Equation 3-9}$$

where V_a is the volume of air (void-space) and V_s is the volume of snow.

The density of snow is

$$\rho_s = (1-\emptyset)\rho_i + \emptyset\rho_a \approx (1-\emptyset)\rho_i \qquad \textbf{Equation 3-10}$$

The ratio of conductivity of ice and saturated moist air is defined as

$$m = \frac{k_i}{k_g} \qquad \textbf{Equation 3-11}$$

The ratio ***m*** decreases as temperature increases, and the value is about 48 and 125 at 0°C and -50°C, respectively; it is thus reasonable to assume that m>>0.

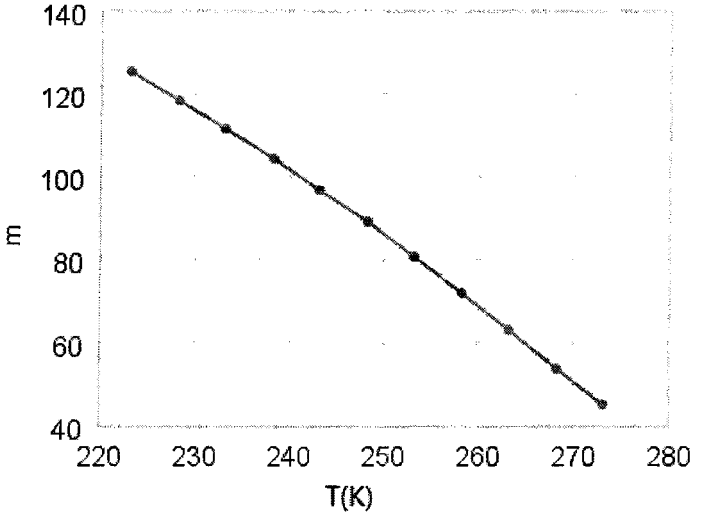

Figure 3-8 Ratio of conductivity of ice and saturated moist air varies with temperature

2. Microstructural Model

For fresh snow, the shapes of snow grains in Figure 3-9 were proposed by Gravner *et al.* (2008).

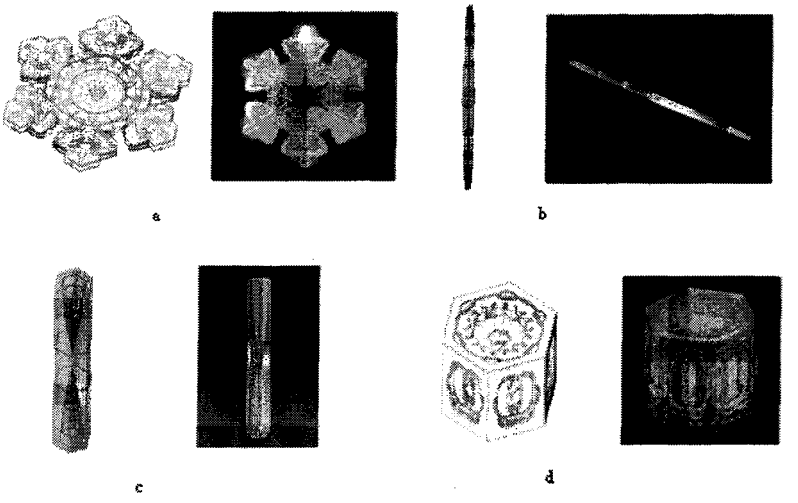

Figure 3-9 (a) sandwich plate, (b) needle, (c) hollow column, and (d) column with hollow prism facets.

For accumulated snow such as that found in a snow sleeve, the basic kind of ice crystal may be used to model a certain type of snow. For example, snow consisting of plate ice crystals can be modeled as two plates plus a connection column. **Figure 3-10** and **Figure 3-11** show a hexagonal plate with bond.

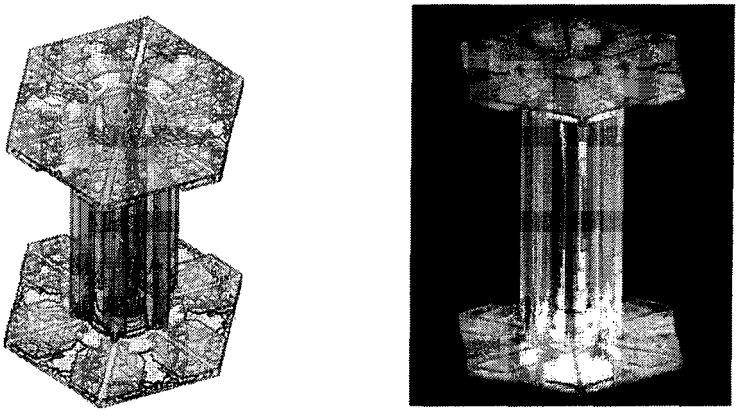

Figure 3-10 A column capped with hexagonal plates

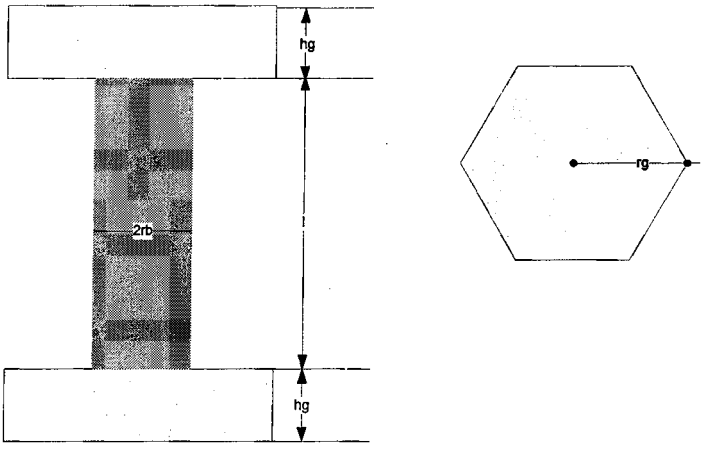

Figure 3-11 Geometrical model for hexagonal plate with bond

The density ratio of snow and ice can be calculated as:

$$n = \frac{\rho_s}{\rho_i} \approx \frac{2h_g A_g + lA_b}{LA} = 2h_g' A_g' + l' A_b' \qquad \textbf{Equation 3-12}$$

where l and h_g are the height of bond and snow grains, respectively; A_b (πr_b^2) and A_g are the intersection area of the bond and snow grain, respectively; the overall height $L = l+2h_g$, the overall area $A = 4r_g^2$; $h_g' = h_g/L$, $l' = l/L$, $A_g' = A_g/A$, $A_b' = A_b/A$.

The intersection area A_g depends on the shape of snow grain, as shown in **Table 3-1**.

The equivalent thermal conductivity of dry snow may be obtained from the following computation:

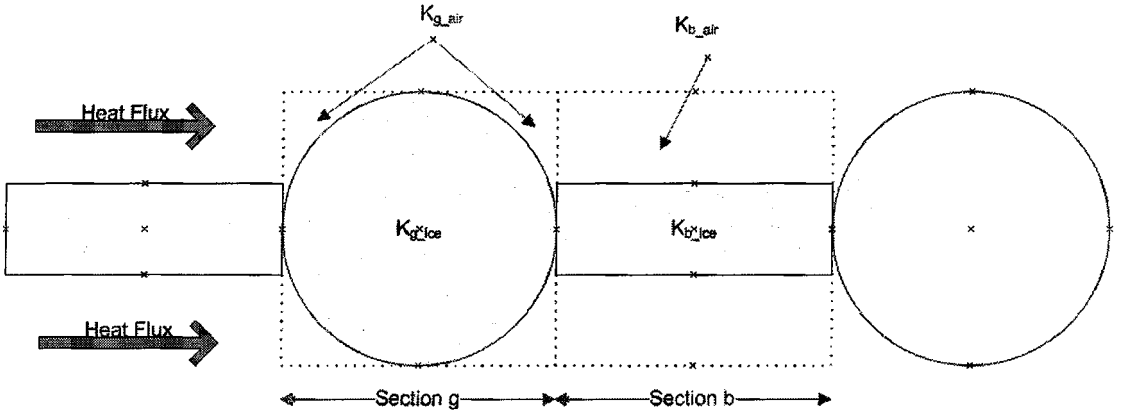

Figure 3-12 Equivalent thermal circuits for snow grain

The thermal conduction of snow grain section ***g***, K_g can be obtained by

$$K_g = K_{g\_air}\frac{A - A_g}{A} + K_{g\_ice}\frac{A_g}{A} = k_g(1 - A'_g + mA'_g) \approx k_g(1 + mA'_g) \quad \textbf{Equation 3-13}$$

The thermal conduction of bond section ***b***, K_b can be obtained by

$$K_b = K_{g\_air}\frac{A - A_b}{A} + K_{g\_ice}\frac{A_b}{A} = k_g(1 - A'_b + mA'_b) \approx k_g(1 + mA'_b) \quad \textbf{Equation 3-14}$$

Therefore, the equivalent thermal conductivity of dry snow can be calculated by

$$k_e = \frac{L}{\frac{2h_g}{K_g} + \frac{l}{K_b}} = k_g\frac{1}{\frac{l'}{1 + mA'_b} + \frac{2h'_g}{1 + mA'_g}} \quad \textbf{Equation 3-15}$$

The ratio of $2h_g$ and l is defined as

$$ra_1 = \frac{2h_g}{l} = \frac{2h_g'}{l'}$$ **Equation 3-16**

The ratio of A_b and A_g is defined as

$$ra_2 = \frac{A_b}{A_g} = \frac{A_b'}{A_g'}$$ **Equation 3-17**

Substituting ra_1 and ra_2 into **Equation 3-13**, it is possible to obtain

$$k_e = k_g(1 + ra_1)\frac{1}{\frac{ra_1}{1 + m\,A_g'} + \frac{1}{1 + m\,ra_2 A_g'}}$$ **Equation 3-18**

A_g and A_g' are a constant for a given shape, as shown in Table 3-1.

Table 3-1 Shape Factors A_g

Shape	A_g	A_g'	Snow Type
Hexagonal plate	$\left(\frac{3\sqrt{3}}{2}\right) r_g^2$	$\frac{3\sqrt{3}}{8}$	Fresh
Spherical plate	$\left(\frac{2}{3}\right) r_g^2$	$\frac{1}{6}$	Rounded grains
Cylindrical plate	πr_g^2	$\frac{\pi}{4}$	Rounded grains
Cubical plate	$4r_g^2$	1	Faceted grains

Thus, for a given shape of snow grain, the equivalent thermal conductivity of snow, k_e, is a function of ra_1, ra_2 and the snow temperature, t_s

$$k_e = f(ra_1, ra_2, t_s)$$ **Equation 3-19**

Substituting ra_1 and ra_2 into **Equation 3-12** it is possible to obtain

$$\rho_s = \rho_i A'_g \frac{(ra_1 + ra_2)}{1 + ra_1} = \rho_i f(A'_g, ra_1, ra_2) \qquad \textbf{Equation 3-20}$$

Kingery (1960) directly determined the ratio of the bonding area between snow grains to the size of the snow grains, as shown in Table 3-2.

Table 3-2 Relationship between temperature and parameter ra_2

Temperature(°C)	ra_2
-5	0.010 - 0.0256
-27	0.007 – 0.018
-88	0.0004 – 0.0001

3.6 Results and Discussion

3.6.1 Comparison with Experimental Data

For comparison, the results obtained from Satyawali *et al.* (2008) and **Equation 3-18** are plotted in **Figure 3-13**, the results obtained from Aggarwal (2004), Sturn *et al.* (1997) and **Equation 3-18** are shown in **Figure 3-14**. The data from this microstructure model is in good agreement considering that the snow density is less than 500 kg/m^3.

For hexagonal plate grain, the value of the equivalent thermal conductivity obtained from **Equation 3-18** increases abruptly when the density is more than 500 kg/m^3. For this model, the density increases as a result of the increase in ra_1. When ra_1 reaches its maximum value, it may be seen that the snow consists of ice cylinders which opposes the assumption that snow is composed of ice particles. In other words, the snow that displays hexagonal plate grain is fresh snow and normally its density is less than 500 kg/m^3.

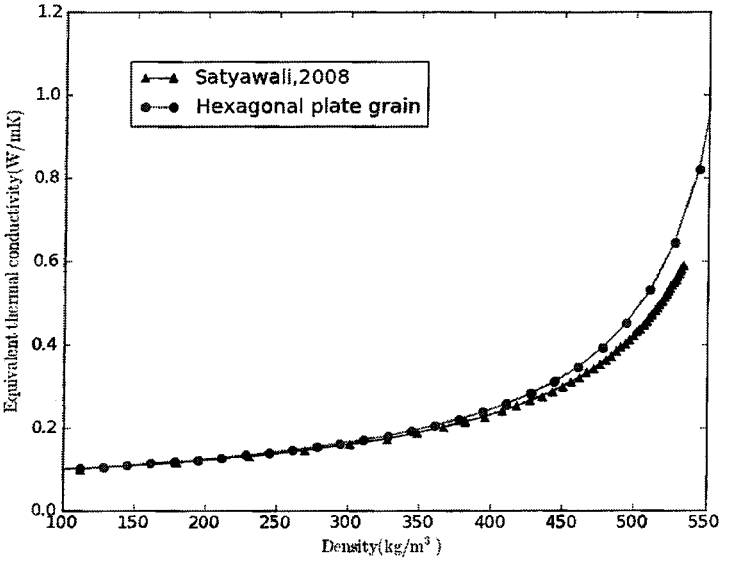

Figure 3-13 Profiles of the equivalent thermal conductivity at -5°C for hexagonal plate grain. Δ, Satyawali *et al.* (2008); o, **Equation 3-18**

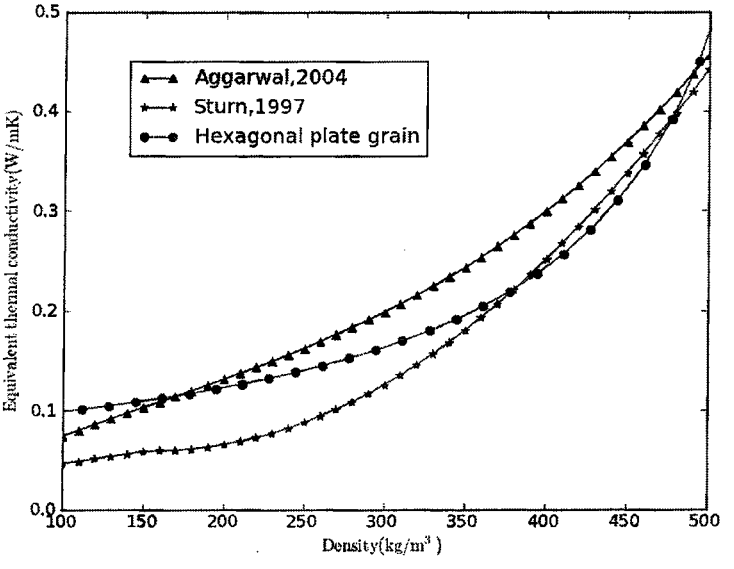

Figure 3-14 Profiles of the equivalent thermal conductivity at -5°C. Δ, Aggarwal (2004); *, Sturn *et al.* (1997); o, hexagonal plate grain from **Equation 3-18**

3.6.2 Effects of Snow Grain Shape

The equivalent thermal conductivity of dry snow for several types of snow grains at -5°C is plotted as a function of density in **Figure 3-15**.

At a higher snow density, there are more snow grains and they are in closer contact, which leads to a higher value of snow thermal conductivity. The plots in **Figure 3-15** corroborate this assumption. The dependency of the thermal conductivity of snow on density is nonlinear as may be observed in this figure.

It also can be found that the equivalent thermal conductivity of dry snow increases as the value of $A_g{}'$ increases.

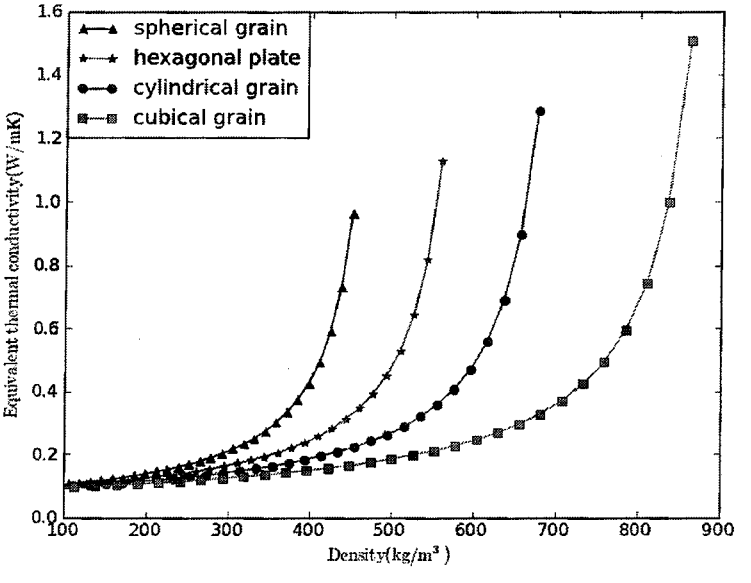

Figure 3-15 Profiles of the equivalent thermal conductivity calculated by **Equation 3-18** for various snow type at -5° C and ra_2 0.0256. Δ, spherical grain; *, hexagonal plate; o, cylindrical grain; □, cubical grain

3.6.3 Effects of Water Vapor

Water vapor plays an important role in the calculation of the equivalent thermal conductivity of dry snow, especially when the temperature is near 0°C. A series of snow conductivity values at -5°C are shown in **Figure 3-16**. Taking the vapor effect into account, snow conductivity is 20% higher than that of dry air, *i.e.* about 20% of the heat moved by vapor.

When the temperature of snow is very low, at about -50°C, the difference between dry air and saturated moist air is only around 1%, implying that the effects of vapor can be disregarded when the temperature is below -50°C.

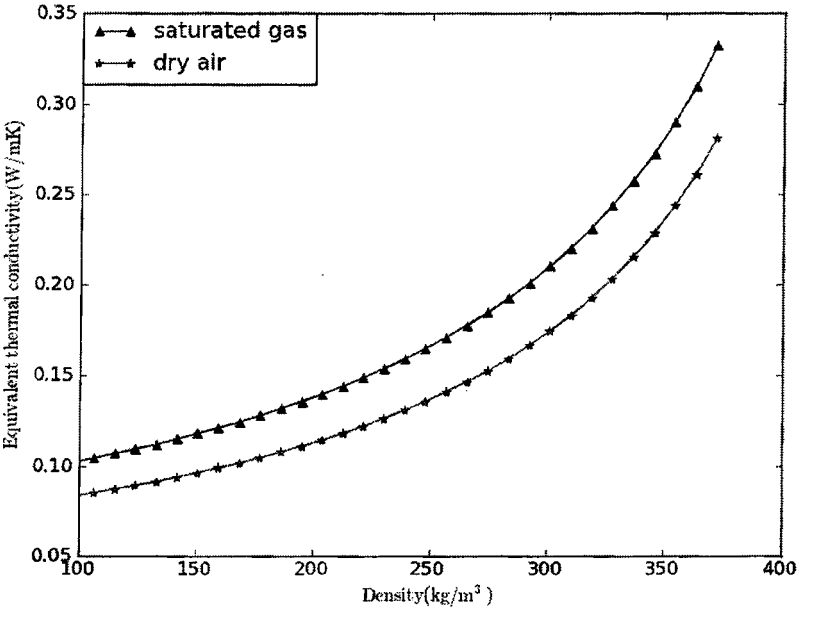

Figure 3-16 Snow conductivity with (Δ) and without the effects of (*) water vapor at -5°C and ra_2 0.0256, calculated by **Equation 3-18**

3.6.4 Effects of Temperature

Figure 3-17 and **Figure 3-18** show a variation of the equivalent thermal conductivity with temperature for cylindrical and hexagonal grain, respectively. Three densities were selected for each figure.

It may be observed that the equivalent thermal conductivity increases with increasing temperatures, especially at temperatures above -5°C. The nonlinear increase in conductivity with increasing temperatures above -5°C is a result of the fact that saturated moist air is more conductive at a higher temperature and that the dependency of saturated vapor pressure with temperature is exponential.

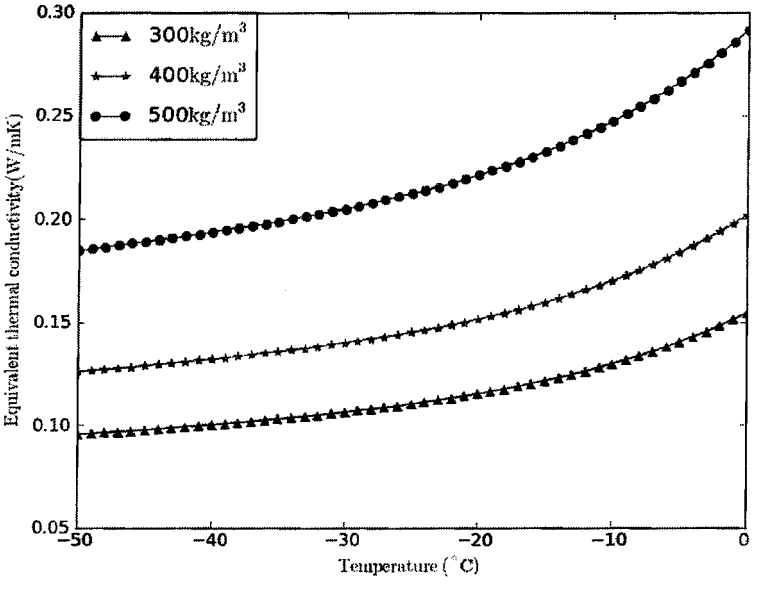

Figure 3-17 Profiles of the equivalent thermal conductivity for snow with cylindrical grain at variable density parameter. Δ, 300 kg/m³; *, 400 kg/m³; o, 500 kg/m³, calculated by **Equation 3-18**

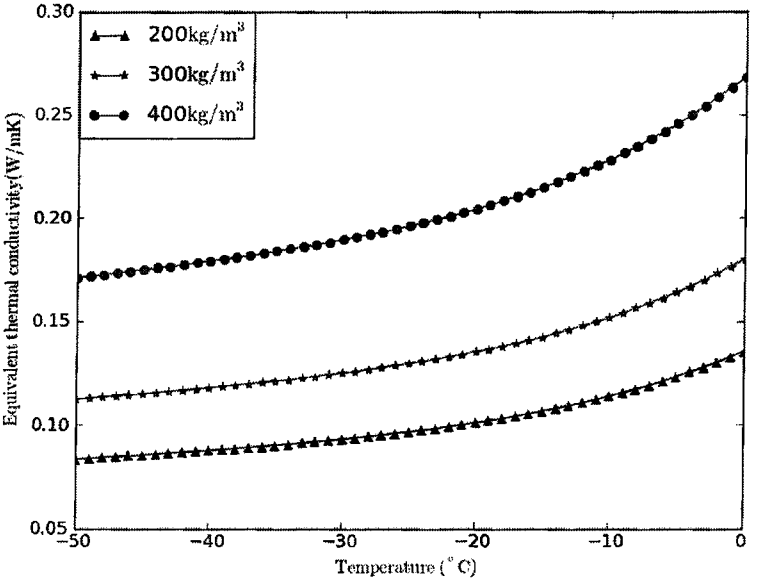

Figure 3-18 Profiles of the equivalent thermal conductivity for snow with plate grain at variable density parameter. Δ, 200 kg/m³; *, 300 kg/m³; o, 400 kg/m³, calculated by **Equation 3-18**

3.7 Snow and Climate

Snow originates in clouds at temperatures below the freezing point. As moist air rises, then expands and cools, water vapor condenses on minute nuclei to form cloud droplets on the order of 10 microns in radius. Once a droplet has frozen, it quickly grows at the expense of the remaining water droplets because of the difference in vapor pressure saturation between the ice and water. The form of the initial ice crystal, whether columnar, platelike, dendritic, and so forth, depends on the temperature upon formation, but subsequent growth and structural details also depend on the degree of supersaturation (Hobbs, 1974). During its fall to earth, a snow crystal may undergo considerable change due to variations in temperature and humidity resulting from changes in altitude.

1. Ice Crystals

By growing snow crystals in the laboratory under controlled conditions, it was found that their shapes depend on both temperature and humidity. This behavior is summarized in the "morphology diagram" shown in **Figure 3-19**, which presents the crystal shape as it occurs under different conditions.

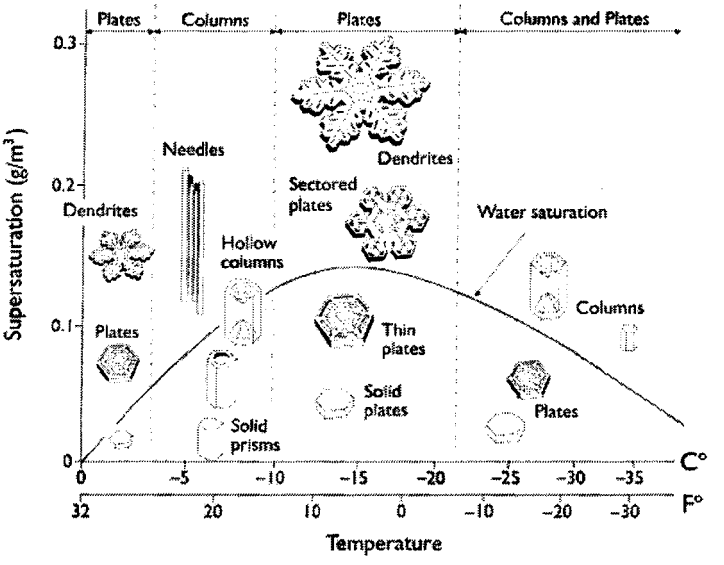

Figure 3-19 Snow crystal morphology diagram showing types of snow crystals that grow at different temperatures and humidity levels, Nakava(1954)

The morphology diagram illustrates the kind of snow crystals and the conditions which govern this formation. For example, it can be seen that thin plates and stars grow at around -2°C, while columns and slender needles appear near -5°C. Plates and stars form near -15°C, and a combination of plates and columns tend to build up at around -30°C.

Six-sided ice crystals that fall to earth in ideal winter conditions, commonly known as snowflakes, exhibit a seemingly endless variety of shapes and structures, often dendritic and strangely botanical, yet highly symmetric and mathematical in their designs.

2. Relationship between the microstructure model and snow grain shape

From **Figure 3-19** it may be observed that:

- the size of the ice crystal and ra_2 increases as the super saturation increases;
- the size of the ice crystal and ra_2 increases as the temperature decreases.

For fresh snow, the shapes of the ice particles include dendrites, plates, solid prisms and needles; these can be modeled mainly as hexagonal, cylindrical, and cubical shapes.

Table 3-3 Weather and models (for fresh snow)

Super saturation	0°C >T>-3°C	-3°C >T>-10°C	-10°C >T>-22°C	T<-22°C
<0.1	M2	M4	M3	M2,M3
0.1<s<0.2	M2	M3,M2	M2	M2,M1
0.2<s<0.3	M1	M2	M1	

Abbreviations of the microstructure models for different grain shape are shown in **Table 3-4**.

Table 3-4 Abbreviation of Models

Abbreviation	Grain shape
M1	Spherical
M2	Hexagonal

M3	Cylindrical
M4	Cubical

The characteristics of the accumulated snow after a snowfall depend on the original form of the crystal as well as on the weather conditions during the deposition event. For example, when a snowfall is accompanied by strong winds, crystals are broken up into smaller fragments favorable to close packing. After deposition, snow will undergo metamorphism and therefore change its grain texture, size, and shape; snow metamorphism will occur primarily as a result of the effects of temperature and overburdened pressure. Snow metamorphism tends to occur rapidly since the crystals remain thermodynamically active due to their large surface-to-volume ratio, or complex shape, and also because their temperature falls at, or proportionally close to, the melting temperature.

With regard to snow which has accumulated for a certain period of time, rounded grains are observed to grow in dry snow at high densities or low temperature gradients within the snow itself, while faceted grains grow in dry snow at low densities or high temperature gradients existing within the snow.

Table 3-5 Weather and models (for accumulated snow)

Grains	model
Rounded	M2,M3
Faceted	M4

For snow accreted around a cable, the snow grains are small, broken, or abraded, closely-packed and well sintered due to the wind (Yukino, 1998). The particle size decreases when the wind speed increases. Model **M4** should be applied to this type of snow.

3.8 Thermal Conductivity Measurement

1. Experimental Set-Up

The experimental setup used to simulate snow shedding is shown in **Figure 4-5**. A wet snow sleeve was reproduced from fresh dry snow collected on the UQAC campus grounds. The dry snow sleeve was produced after wet snow sleeve was exposed in the wind below 0°C for over one hour. The cable used in experiments is ALCAN Pigeon ACSR with 12.75 mm diameter and the electric resistance is 0.0003 Ω /m at 20 °C.

Figure 3-20 and **Figure 3-21** show the instruments needed to measure the thermal conductivity of snow. Two thermal-couples are placed at different positions within the snow. The air temperature is set below 0°C and the electric current at 50-100A.

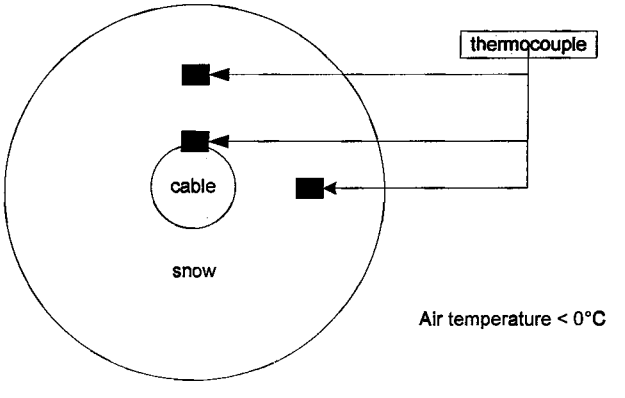

Figure 3-20 Schematic diagram of experimental set-up

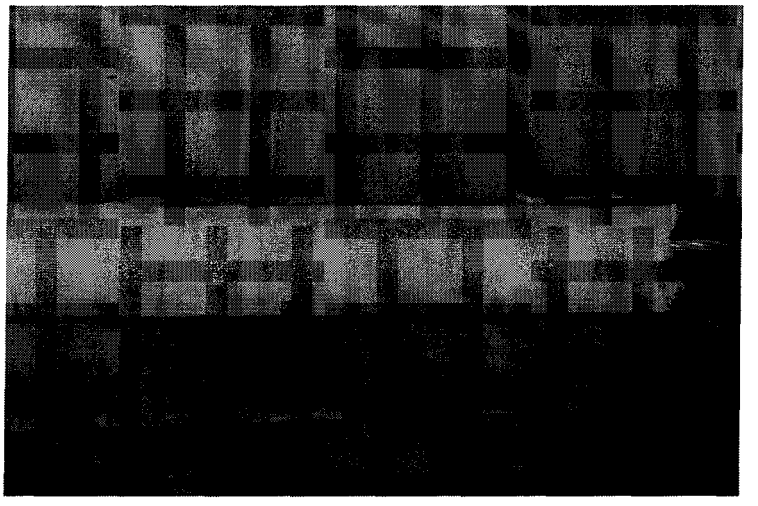

Figure 3-21 Photo of experiment in process

As the heat flux from the cable is constant, snow conductivity is obtained by measuring the temperature gradient within the snow.

2. Calculation Process

The snow sleeve may be regarded as a hollow cylinder, whose inner surface connects to the cable surface and whose outer surface is exposed to air at different temperatures, as shown in **Figure 3-22**. Moreover, it may also be assumed that the snow sleeve is under steady-state conditions with no internal heat generation.

The corresponding form of the heat equation is

$$\frac{1}{r}\frac{d}{dr}\left(k_s r\frac{dT}{dr}\right) = 0 \qquad \textbf{Equation 3-21}$$

where k_s is the conductivity of snow, r is the cylindrical coordinate, and T is the temperature at the r position.

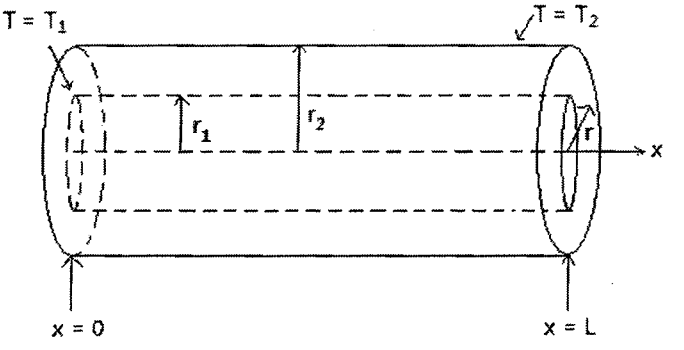

Figure 3-22 Cross-section of a snow sleeve

Assuming the value of k_s to be constant, **Equation 3-21** can be integrated twice to obtain the general solution:

$$T(r) = \frac{T_1 - T_2}{\ln(r_1/r_2)} \ln\left(\frac{r}{r_2}\right) + T_2 \qquad \textbf{Equation 3-22}$$

where r_1 and r_2 are the radii of the inner and outer thermal-couple positions, respectively; and T_1 and T_2 are the temperatures measured by the inner and outer thermal-couples, respectively.

The rate at which energy is conducted across the cylindrical surface in the snow is expressed as:

$$Q_r = -k_s A \frac{dT}{dr} = -k(2\pi L)\frac{dT}{dr} \qquad \textbf{Equation 3-23}$$

Substituting **Equation 3-22** into **Equation 3-23**, we obtain the following expression for a heat transfer rate:

$$Q_r = \frac{2\pi L k_s (T_1 - T_2)}{\ln(r_1/r_2)} \qquad \textbf{Equation 3-24}$$

Therefore, the snow conductivity can be calculated by:

$$k_s = \frac{Q_r \ln(r_1/r_2)}{2\pi L(T_1 - T_2)} \qquad \textbf{Equation 3-25}$$

The resistance (R_T) of the conductor at any temperature (T) will be (Pabla, 2005):

$$R_T = R_{20}[1 + 0.00403(T - 20)] \qquad \textbf{Equation 3-26}$$

where R_T is the resistance at temperature T(°C) and R_{20} is the resistance at temperature 20°C.

The heat transfer rate through the snow sleeve is:

$$Q_r = I^2 R_T = I^2 R_{20}[1 + 0.00403(T_1 - 20)] \qquad \textbf{Equation 3-27}$$

where I is the electric current intensity(A).

Equation 3-25 can be written as:

$$k_s = I^2 R_{20}[1 + 0.00403(T_1 - 20)] \frac{\ln(r_1/r_2)}{2\pi L(T_1 - T_2)} \qquad \textbf{Equation 3-28}$$

3. Results and Discussion

The experimental data is provided in **Figure 3-23**. The equivalent thermal conductivity for a hexagonal grain shape was superimposed on the data for comparison. It may be observed that few results show agreement with experiments. The wide scatter of the

experimental data observed at a given density is a result of the strong influence of the microstructure on thermal conductivity. Considering that the snow used in these experiments was collected from ground accumulation, it was difficult to estimate the shape of the snow grains and it is reasonable to assume that the snow was a mixture of several types.

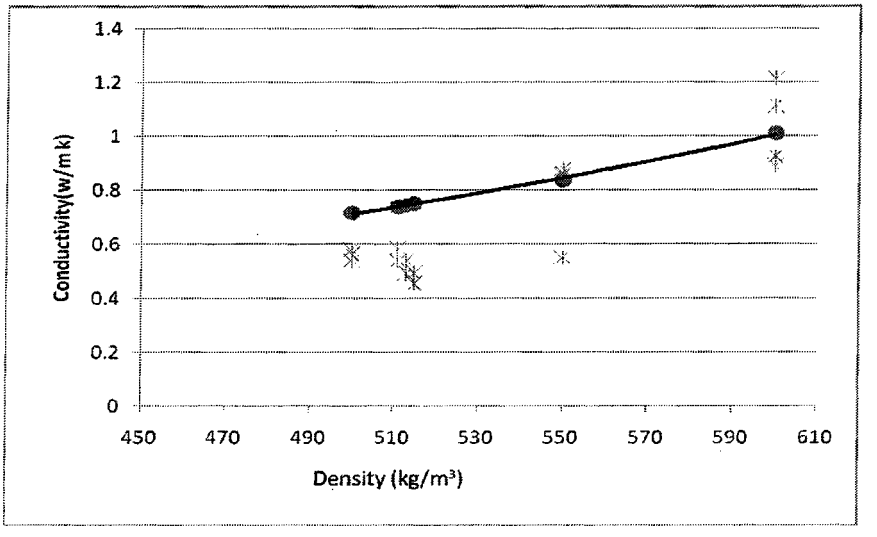

Figure 3-23 Experimental snow conductivity *vs* density at an air temperature of -4°C. *, experimental data; o, result of **Equation 3-18**

Certain experimental data shows higher conductivity values than empirical equations. The snow sleeves used in these particular tests were made up of wet snow. When the test was performed at an early stage, the ambient air temperature was not low enough to keep most of the snow below 0°C, *i.e.* there was wet snow to be found within the sleeve. The presence of water and vapor in wet snow causes the equivalent thermal conductivity of snow to increase.

There are a number of drawbacks in the experiments because of a variety of uncertainty factors. Among them are:

a. the thermo-couples probe simultaneously connects air, ice particles, and water, thereby leading to an unsteady scale reading from the thermocouple;
b. the accuracy of the thermocouple itself;
c. changes in the position of the thermocouple within the snow due to gravity;
d. the occasional tendency of snow sleeves to roll over.

3.9 Conclusions

The equivalent thermal conductivity of dry snow was analyzed and modeled. The thermal characteristics of snow depend upon various factors such as the thermal conductivity of the constituent phases, and the shape and size of the snow grains.

The analytical results were compared with experiments conducted at the CIGELE laboratories. Furthermore, the concept of relationship between the snow conductivity model and the weather was introduced.

CHAPTER 4

SIMULATION OF WATER PERCOLATION WITHIN A SNOW SLEEVE

4.1 Introduction

In order to predict the occurrence of snow shedding events, it is recommended that the flow characteristics of the melted water within snow sleeves be estimated. For this purpose, research must be carried out on the mechanism of snow melting and water percolation within snow sleeves so that improved methods of preventing snow accretion or shedding may be developed.

The study of water percolation poses a genuine challenge, however, since only scant studies are available in the literature for consultation. Water percolation within a snow sleeve depends on the water saturation as well as on the various microstructural parameters of wet snow such as porosity, or the size and shape of the snow grains. Water percolation involves several feedback mechanisms and non-linear relationships between various factors such as water flow within snow which not only depends on the microstructure of the snow

but changes it also. Water percolation may be affected by the concurrent heat exchanged between water, air, and the ice matrix.

4.1.1 Research Objectives

The main objective of this research is to develop a 2D time-dependent numerical model for simulating a water percolation process within a snow sleeve under various meteorological conditions and the prevailing current transmission environment. The effects of wind velocity, air temperature, Joule heating, snow surface roughness, and snow grain size were investigated and analyzed with this objective in mind.

- ***To study the effects of the outer air flow***

This objective implies studying how the forced heat convection affects snow melting and melted water percolation within a snow sleeve as well as comparing the influences from air temperature and velocity.

The cross-air flow around a snow sleeve causes an uneven heat flux distribution at the snow surface. The snow surface roughness also has a significant effect on the heat flux distribution considering that its value is sufficiently great. These effects will lead to uneven melting at the sleeve surface and then proceed to affect melted water percolation subsequently.

- ***To study the effects of Joule heat***

It was found, experimentally, that Joule heat is an effective way of accelerating snow sleeve melting and will thus tend to lead to snow shedding more rapidly. A number of devices using electric heating to eliminate ice accretion on overhead wires have already been invented and are now used in China as well as in other countries.

The objectives relate to the investigation into the manner in which the electric current accelerates melted-water percolation and snow shedding.

- ***To study the effects of snow intrinsic properties on water percolation***

This specific objective is directed towards studying the way in which the intrinsic properties of snow affect the process of snow melting and melted water percolation within a snow sleeve.

Water percolation is governed mainly by two forces: the specific gravity of water and capillary action. The rate of water percolation is affected by snow characteristics through the porosity of snow, as well as the shape and size of the snow grains.

The permeability of snow may be considered as one of the significant parameters when modeling either saturated or unsaturated water flow. It is difficult, however, to obtain this permeability by means of analysis or empirical methods considering that it depends not only on snow porosity and snow grain geometry but also on the water content within the snow per se.

4.1.2 Methodology

This research was carried out by first performing theoretical modeling and then following it with experimental investigation in order to validate the earlier modeling procedure.

- ***Developing a numerical model***

Melted water percolation within a snow sleeve is modeled by means of the two-dimensional Finite Element Method (FEM) and the two-dimensional Finite Volume Method (FVM), under different snow properties and outer environmental conditions.

Most of the previous work was conducted on snow pack and utilized a one-dimensional model. The geometry of the snow sleeve with a hole produced by a line conductor, however, is more complex. The outer heat sources, such as ambient air heating by forced convection, lead to a varying heat flux at the sleeve surface. Therefore, the snow sleeve around a cable is not suitable for a one-dimensional numerical model.

The main purpose of developing the FEM and FVM methods concurrently is to verify the numerical results and by comparing them. A subprogram checks for mass balance error at each step during the FEM and FVM computation process.

- ***Conducting the experiments***

A set of experiments simulating natural snow shedding is to be conducted at the CIGELE laboratories. These tests can be carried out under two main environmental

conditions: forced air convection with varied air velocity and temperature, and Joule heating.

Variations of air temperature, air velocity, and electric current were applied to the experiment and the variations in LWC and density were recorded at intervals. Snow shedding was observed at the end of each test, while the experimental data was compared with the results from the numerical model.

4.1.3 Review of the Literature

Developing numerical models for water flow in the unsaturated or saturated zones has become increasingly popular due to the complexities of geometry and of inhomogeneity, thereby leading to a few analytical solutions being obtained. Most of the numerical models for the fluid flow were developed by using Richard's differential equations.

Work was carried out for water transport in soil. One- and multi-dimensional models of unsaturated water flow in soil were presented by Gottardi *et al.* (1993, 2001), James *et al.* (1983) and Kumer (2002).

Water flow in wet snow is more complex than it is in soil. The simplest theory for the water flow in wet snow disregarded the diffusive effects of capillary pressure (Colbeck 1971, 1972, 1977). In Colbeck's model for simple gravity drainage, capillary is thought to be negligible compared with gravity since the water saturation values are generally in the "mid-range". Sellers (2000) presented a model for the transport of water in melting snow surface where the percolation front was treated as a propagating singular surface and

numerical examples were provided of the propagation of one-dimensional melted water waves in deep snow packs.

The effect of the capillary pressures on the water flow was introduced into the basic gravity flow theory and numerical models were developed for the water flow in wet snow by Colbeck (1974), Gray(1996) and Bengtsson (1982).

Water movement in subfreezing snow occurs under special circumstances and follows extremely complex patterns. Illangasekare *et al.* (1990) and Tseng *et al.* (1994) developed a two-dimensional numerical model which incorporates heat transfer into the process of water flow in the subfreezing snow.

Nearly all of this research focuses on the snowpack accreted on the ground, whereas few studies have been carried out on the water flow in a snow sleeve around a line conductor.

4.2 The Mathematical Model

The model of this research is based on the Richards equation, which describes the movement of water in an unsaturated medium.

4.2.1 Governing Equation

Darcy (1856) proposed a phenomenology derived constitutive equation that describes the flow of a fluid through a porous medium.

$$v_w = -K\nabla h_p \qquad \textbf{Equation 4-1}$$

where v_w is the drainage water velocity (m/s), K is the permeability or hydraulic conductivity (m/s) and h_p is the piezometric head (m).

By regarding the averaged flow field as a continuum and applying the principle of mass conservation, the Eagleson equation (1970) may be derived. The compressibility of water and the ice matrix is fairly small and its effect on the water flow has been disregarded for the purposes of this research; the density of water can thus be considered as a constant at a given temperature, as follows:

$$-\emptyset\frac{\partial S}{\partial t} = \nabla \cdot (q) \qquad \textbf{Equation 4-2}$$

where S is the water saturation. By combining **Equation 4-1** and **Equation 4-2**, the governing Richards equation, for two-dimensional unsaturated flows in a vertical plane within a porous medium, may be obtained as:

$$\frac{\partial}{\partial x}\left[Kk_{rw}\left(\frac{\partial \psi}{\partial x}\right)\right] + \frac{\partial}{\partial z}\left[Kk_{rw}\left(\frac{\partial \psi}{\partial z} + 1\right)\right] + W_v = C\frac{\partial \psi}{\partial t} \qquad \textbf{Equation 4-3}$$

where K is the saturated hydraulic conductivity (m/s), k_{rw} is the relative permeability of water at a given saturation ($1 \leq k_{rw} \leq 0$) and is a function of water saturation, ψ is the pore water pressure head (m), W_v is the positive liquid flow rate into the system (m^3/s), C is the moisture capacity (1/m), and x and z represent the horizontal and vertical coordinates, respectively.

The Richards equation is a non-linear partial differential equation, which is often difficult to approximate since it does not have a closed-form analytical solution.

By the definition of the hydraulic head, h_p, it can be written as $h_p = \psi + z$. Under the atmosphere, $h_p = z$ ($\psi = 0$). For discussing boundary conditions, it is convenient to use h_p instead of ψ and z.

In order to solve the Richards equation, a water retention curve (WRC)–$S(h_p)$, which describes the relationship between the capillary head, h_p, and the moisture content, S is required. Additionally, the dependence of the relative hydraulic conductivity on the moisture content $K_r(S)$ needs to be specified.

4.2.2 Saturated Hydraulic Conductivity

The saturated hydraulic conductivity is defined as

$$K = \frac{k\rho_w g}{\mu_w} \qquad \textbf{Equation 4-4}$$

where k is the intrinsic permeability (m^2), ρ_w is the density of water (kg/m^3), μ_w is the dynamic viscosity of water (Pa s), and g is the local gravitational constant (m^2/s).

The expression most often used to calculate the intrinsic permeability of snow, k, was empirically developed by Shimizu (1970)

$$k = 0.77 d^2 e^{-7.8\rho_s} \qquad \textbf{Equation 4-5}$$

where d is the mean grain size (m), and ρ_s is the bulk density of the snow (kg/m^3).

Equation 4-5 was developed for snow grains of less than 1.0 mm, but Colbeck suggests that it is reasonable to apply it to grains of up to 2.0 mm. It should be noted that its validity

has not been well substantiated for snow that has been subjected to a great deal of melted water refreezing.

4.2.3 Relative Permeability

The relative permeability, k_{rw}, is a function of saturation and saturation varies in a nonlinear fashion with the pore water pressure. In order to solve the governing equation, it has to be known for the intrinsic permeability as well as the functional relationships between relative permeability and saturation and between saturation and pressure head.

Water retention curves, or WRCs are typically determined from laboratory experiments and a subsequent fitting of a particular functional form of $h_p(S)$ to the data. A typical plot of the water retention curve (WRC) is shown in **Figure 4-1** .

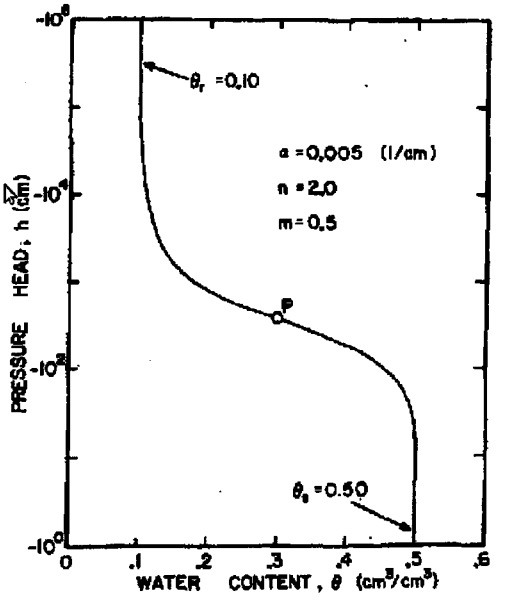

Figure 4-1 Typical plot of the soil-water retention curve from Van Genuchten (1980). The point P on the curve is located halfway between S_r (= 0.10) and S_s (= 0.50)

From among a variety of models, the WRCs proposed by Brook and Corey (1964) and Van Genuchten (1980) are the most popular for determining relative permeability.

1. The Brook and Corey model

The relationship between saturation and the pressure head is usually presented in terms of the effective saturation S_e

$$S_e = \frac{S - S_r}{1 - S_r} \qquad \text{Equation 4-6}$$

where S_r is the residual saturation.

For wet snow at 0°C, Colbeck *et al.* (1978) determined S_r to be 0.07, Bengtsson (1982) reported it to be 0.05, whereas Ambach *et al.* (1981) confirmed a value of 0.03.

Traditionally, the relative permeability is written as an empirical power function of effective saturation.

$$k_{rw} = S_e^{\varepsilon} \qquad \textbf{Equation 4-7}$$

The constant, ε, is unique to the particular combination of fluid and porous medium.

2. The Van Genuchten model

Van Genuchten (1980) proposed a relatively simple equation for the soil water content-pressure head curve h_p.

$$S_e = \left[\frac{1}{1+(ah_p)^n}\right]^m \qquad \textbf{Equation 4-8}$$

The parameters ***a***, ***m***, and ***n*** in **Equation 4-8** remain to be determined. Taking the value of ***m*** as 1 has been successfully applied in a number of studies. With the help of results obtained from the Brook and Corey models, the values of ***a*** and ***n*** can be obtained by applying a data-fitting method. Using a set of experimental data for snow in this research, ***a*** = 2.8963 and ***n*** = 3 were obtained.

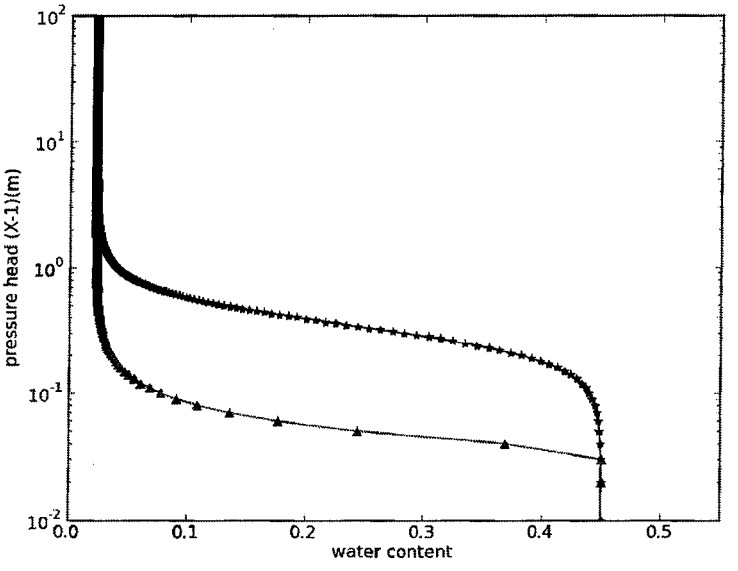

Figure 4-2 Snow-water retention curve based on the Brook and Corey model (Δ) and the Van Genuchten (*) model applied to snow

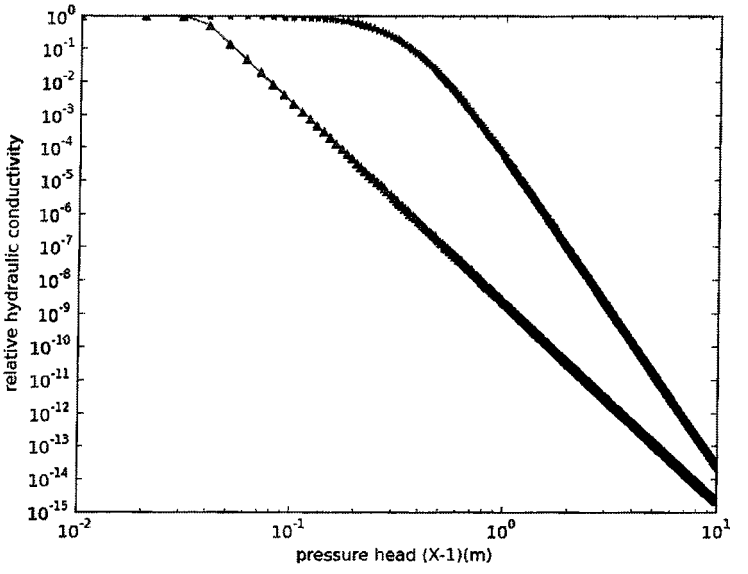

Figure 4-3 Relative hydraulic conductivity *vs.* pressure head as predicted by the Brook and Corey model (Δ) and the Van Genuchten model (*) applied to snow

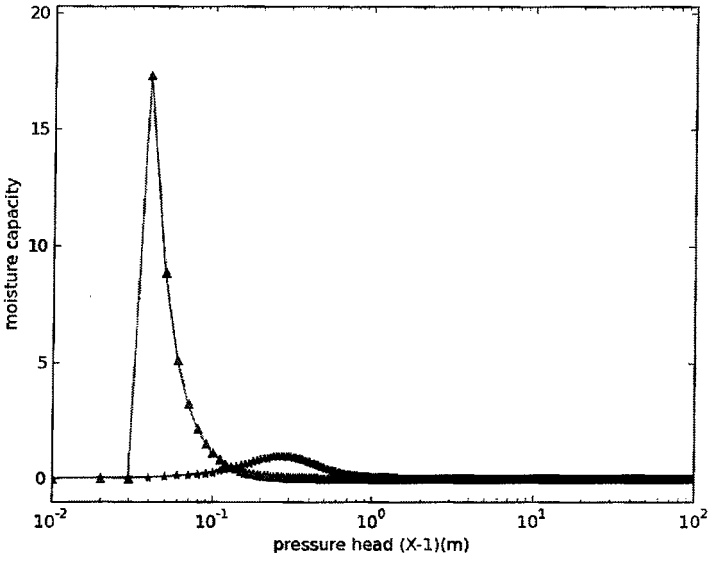

Figure 4-4 Moisture capacity *vs.* pressure head as predicted by the Brook and Corey model (Δ) and the Van Genuchten model (*) applied to snow

3. Discussion and Conclusion

Results presented diagrammatically in **Figure 4-2, Figure 4-3**, and **Figure 4-4** may be obtained from empirical snow data, using the Brooks and Corey followed by the Van Genuchten models, respectively. The accurate predictions for the Brooks and Corey model were obtained for water flow in soil. There is a discontinuity in the slopes of the curves shown in these figures, however, which is especially obvious in **Figure 4-4**. This discontinuity is susceptible to preventing the numerical modeling of saturated-unsaturated flow from rapid convergence when the snow involved in the numerical modeling approaches a saturated state. For a fully unsaturated water flow in snow, similar results may be obtained with the Brooks and Corey, and the Van Genuchten models. The influence of discontinuity, however, especially in the numerical modeling, cannot be disregarded in favor of the water flow in the saturated state The Van Genuchten model was chosen for this particular research because both unsaturated and saturated snow were dealt with the numerical modeling of the water percolation within a snow sleeve.

4.3 Experimental Study

The aim of the experimental study was to investigate the water percolation within a snow sleeve, and to validate the water-percolation model discussed in the preceding section. The experimental conditions including the temperature, the air velocity and the electric current were used as input parameters for the modeling in this research.

A series of tests was conducted at the CIGELE during the winters of 2008, 2009, and 2010. Wet snow sleeves were reproduced from fresh dry snow collected on the UQAC

campus grounds. Most of experiments were carried out in climate room (**Figure 4-5**A). A few tests was also carried out using the CIGELE Atmospheric Icing Research Wind Tunnel (CAIRWT) by means of which stronger air flow can be provided (**Figure 4-5**B). A snow sleeve with a maximum length of 0.9 m can be produced in the wind tunnel.

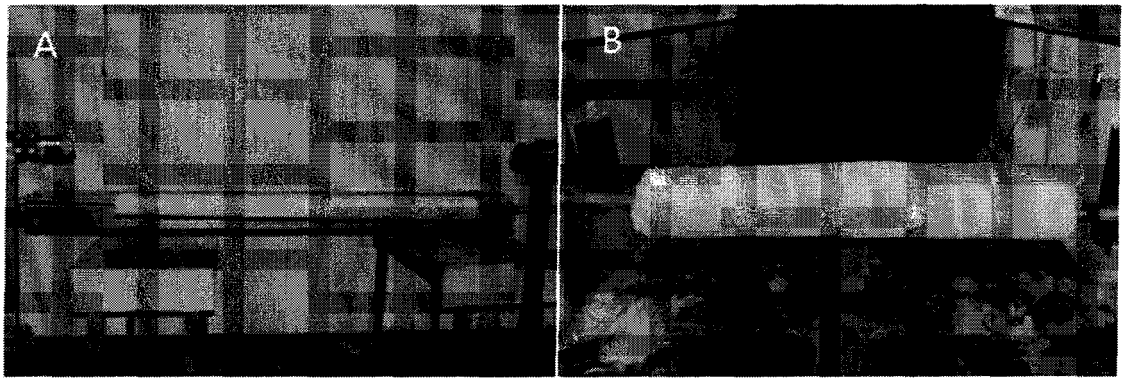

Figure 4-5 Experiments conducted at the CIGELE laboratories. A, in a cooling room; B, in wind tunnel

Before any observations were made, the instruments were carefully calibrated so that the experimental conditions would accord as closely as possible with those observed under natural conditions.

It should be noted that all the models developed in this thesis and all the experiments conducted at CIGELE were only valid for one kind of line conductor and one type of snow sleeve. Only forty tests were carried out successfully in this PhD study because the experiments were time consuming and not all the snow suited for experiment. Moreover, sometimes I had to sharing experimental equipment with other researchers. Therefore, all

the experiments concentrate on only one kind of line conductor and snow sleeve to achieve better validation and support for the models in this thesis.

4.3.1 Experimental Set-Up

The experimental setup used to simulate snow shedding is shown in **Figure 4-6** and **Figure 4-5**.

- One 5 meter long ground wire (ALCAN Pigeon ACSR, 12.75 mm diameter) was installed approximately 1 meter above the floor and tensioned by cable-hoists to remove most of the sag due to the snow load.
- A power supply provided Joule heat.
- A wind generator provided forced convection around the sleeve.

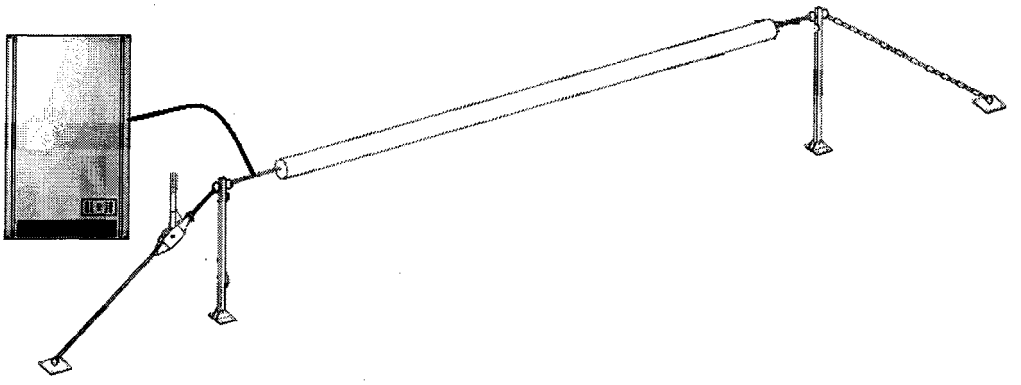

Figure 4-6 Schematic drawing of the experimental set-up in a controlled climate room

4.3.2 Experimental Procedure

1. Wet Snow Sleeve Molding

Fresh dry snow was collected from the ground and exposed to air at 5°C to allow it to turn into wet snow. This method produced an adequate wet snow material with good LWC uniformity.

An experiment technique proposed by Roberge (2006) utilized simple tools to reproduce wet snow sleeves. **Figure 4-7** shows the tools used for snow sleeve fabrication. A ground wire was placed just over a semi-cylindrical mold. Wet snow was laid inside the mold and compacted evenly with a semi-cylindrical hand tool. Snow sleeves having a 0.1 m diameter were thus obtained.

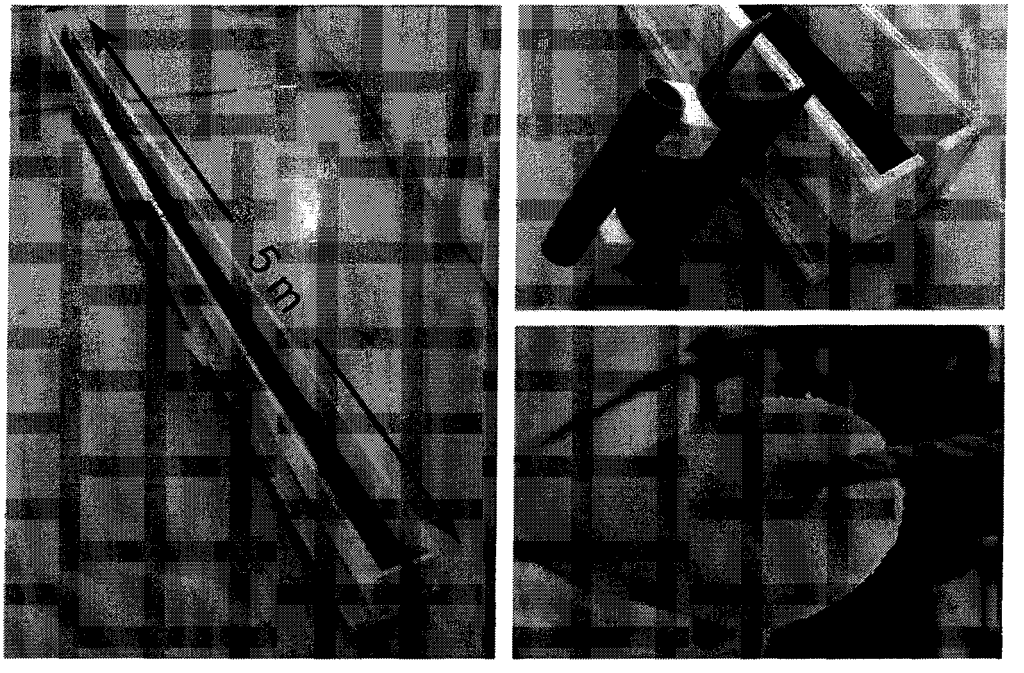

Figure 4-7 Tools for snow sleeve fabrication

2. Test Conditions

The following are the test conditions required for the experiment:

- air temperature varying from 1°C to 5°C;
- air velocity varying from 1~5 m/s in the climate room and 1~10 m/s in the wind tunnel.
- electric current varying from 25 A to 100 A.

3. Observation and Data Recording

The snow properties, bulk density and Liquid Water Content (LWC), were recorded at intervals of 20~30 minutes.

As proposed by Roberge (2006), the hot calorimetry method was used to measure LWC within snow sleeve. The tools needed for this measurement method is shown in **Figure 4-8**.

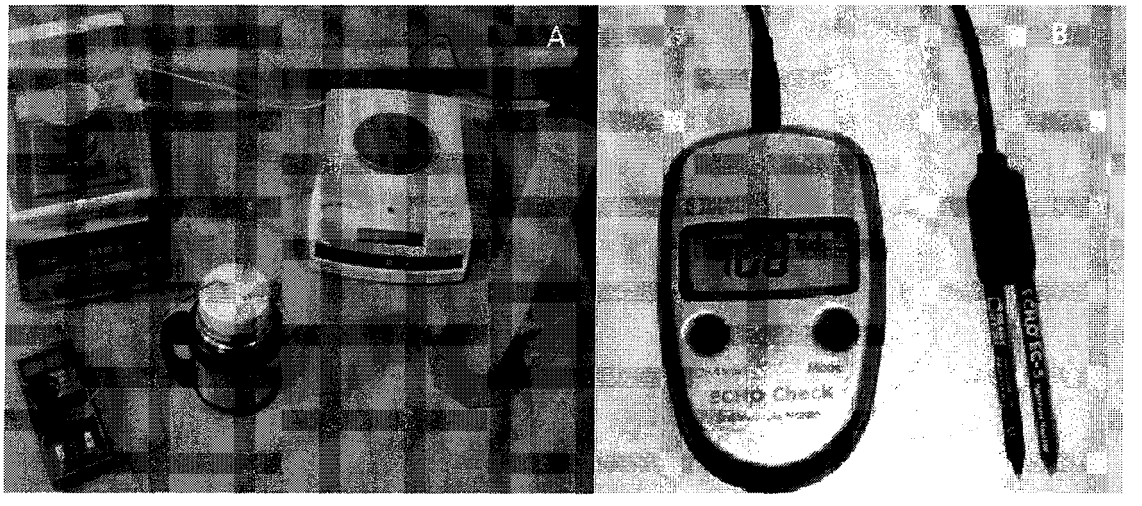

Figure 4-8 Tools for LWC measurement (A from Roberge, 2006)

The measurement procedure is illustrated in **Figure 4-9**:

- Flush the calorimeter with warm water, empty and dry
- Weight mass of hot water m_1
- Put hot water into the calorimeter, close lid, stir and let sit for one minute
- Measure the temperature T_1 of hot water
- Weight the mass of snow sample, m_2; the temperature of wet snow, T_2 was assumed as 0°C
- Put snow sample into the calorimeter , close lid and wait until snow melted thoroughly
- Measure the temperature T_3 of mixture

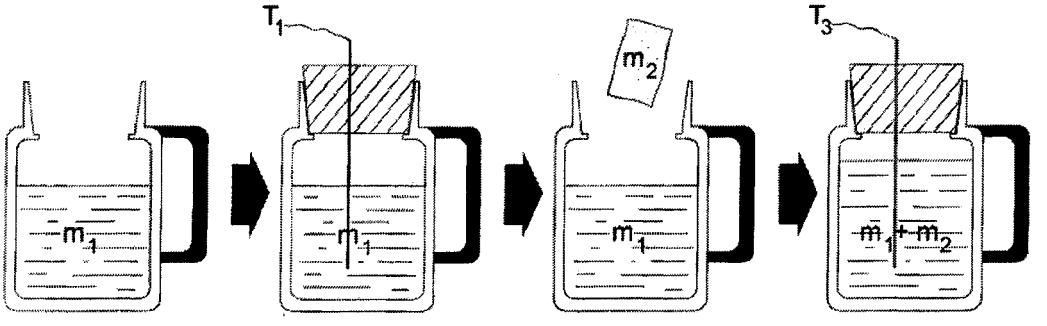

Figure 4-9 LWC measurement using a fusion calorimeter (Roberge, 2006)

The LWC of the snow sample can calculated :

$$LWC = \frac{m_2\left(\frac{L}{c_w} + T_3\right) + \left(m_1 + \frac{c_c}{c_w}\right)(T_3 - T_1)}{m_2\left(\frac{L}{c_w}\right)} \times 100\% \qquad \textbf{Equation 4-9}$$

where L is specific latent heat of fusion of water, C_w, C_c are specific heat capacity of water and container, respectively.

It took at least 5 minutes to complete one hot calorimetry method measurement. A new device, known as the Decagou model EC-5 moisture sensor (**Figure 4-8**B) which was built to measure water content in any soil or soil-less media, proposed by Dr. Kollar of the CIGELE, was also used in this research in 2009.

4.3.3 Discussion and Conclusion

The experiments were time consuming as well as laborious. It took more than five hours to carry out one test. About 30 experiments were performed at the CIGELE laboratories. Melting was observed in each test case.

1. Water Percolation

Melted water migrated to the bottom of the snow sleeve and a saturated zone appeared within the space of a few hours. Measurements showed that, at the beginning of the test, the density and LWC values in the upper region of a snow sleeve increased with the passage of time and then subsequently both decreased. In the majority of measurement cases, water seepage was discernible before snow shedding occurred.

The snow sleeve also became slightly elliptical with time. Snow shedding was observed at each test and tended to progress slowly, occurring in a section 0.15 m long at one end of the snow sleeve. This sleeve portion dropped abruptly after bending under its own self-weight after the cable melted its way through, as shown in **Figure 4-10** and **Figure 4-19**.

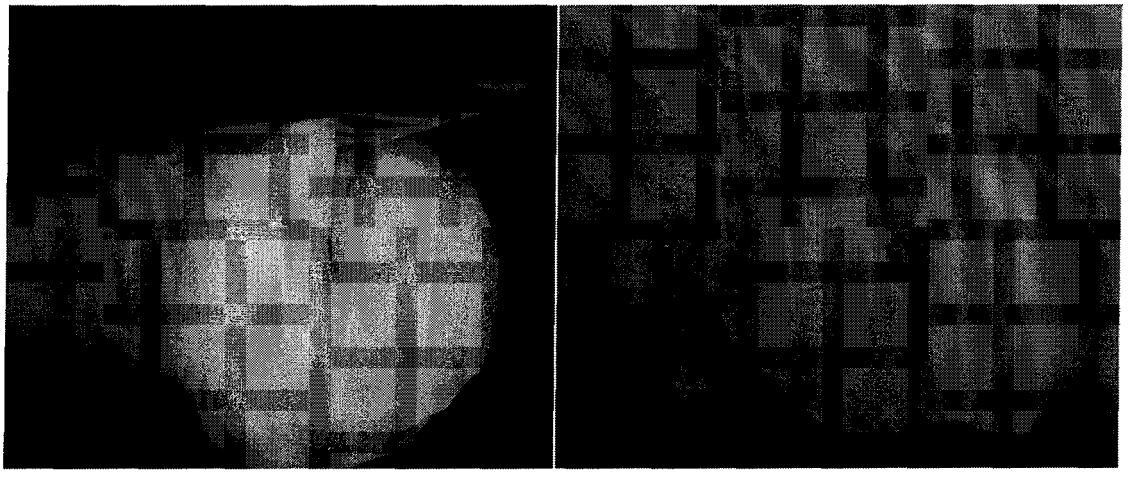

Figure 4-10 Photo of snow shedding taken at the CIGELE

2. Effects of Wind and Air Temperature

Theoretically, wind will increase forced convection and allow snow to melt quickly. This fact was corroborated by a number of experiments in this research. The tests also illustrated that snow melting increased as the air temperature increased.

A snow sleeve can, however, be eroded dramatically by strong winds. As may be seen from **Figure 4-11,** there are numerous holes and gaps apparent in the snow sleeve.

3. Effects of Joule Heating

Joule heat is produced when an electric current flows through a cable. It was experimentally proven that an electric current can effectively accelerate snow shedding. Snow shedding occurred within the space of one hour when the electric current was higher than 75 A.

Figure 4-11 Snow sleeve eroded by strong wind

4.4 Numerical Approach

4.4.1 Summary of Assumptions

Since water flows through a snow sleeve in a highly complex and irregular manner, a number of assumptions may be made for describing the water percolation process.

1. The cable sag is neglected because the model proposed here is two-dimensional. The snow sleeve is assumed as perfect circle cylinder with a cable in the center.
2. Only wet snow is dealt with in this modeling. No refreezing phenomena occur during the whole water flow process.
3. It is assumed that there is no channel flow or fingering due to the local concentration of water even though instability of the water flow has been observed under a variety of natural conditions. The Richards equation can thus be applied.
4. Snow in small volumes is considered homogeneous and isotropic, and therefore the

saturated hydraulic conductivity and the relative hydraulic conductivity of snow are only functions of the density and of the water content, respectively.

5. The deformation of the ice matrix on the snow sleeve boundary is negligible.
6. The mass loss of ice due to melting should be disregarded.
7. The effects of hysteresis resulting from thawing, or wetting, need not be taken into account in the modeling.
8. There is no transfer of momentum due to the viscous effects and frictional forces between phases.

4.4.2 Numerical Approach

Two numerical methods, FEM and FVM were developed and implemented in high-level programming language PYTHON. The main purpose of developing these two methods concurrently is to verify the numerical results and by comparing them, because few results can be found in published papers.

1. Discrediting the Continuum
    a. FEM

The solution region should be divided into non-overlapping elements or sub-regions. The simplest geometric shape which can be employed to approximate irregular surfaces is the triangle, and it is one of the popular elements currently used in finite element calculations. The equilateral triangle was chosen to facilitate the computation of the

modeling of water percolation within a snow sleeve. The element used in this study may be seen in **Figure 4-12**(A).

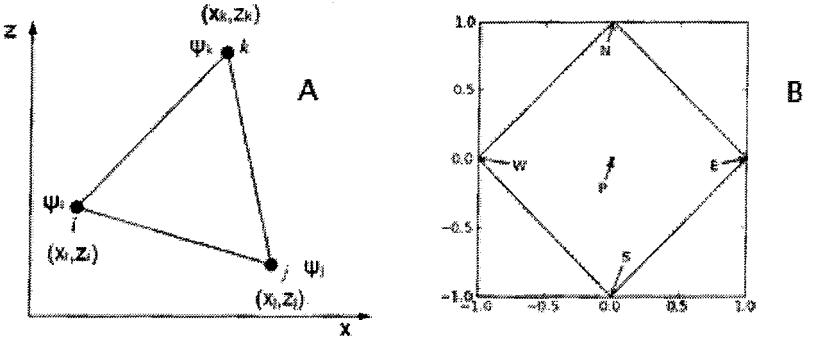

Figure 4-12 Schematic of element used in FEM (A) and FVM (B)

Creating right triangles, such as **b** in **Figure 4-13**, is easier than creating equilateral triangles, such as **c** in **Figure 4-13,** while constructing a mesh for a cylinder-like geometry. The shape of the equilateral triangle, however, was chosen in this study to benefit the steady computation.

The mesh of the whole domain is shown in **Figure 4-14.**

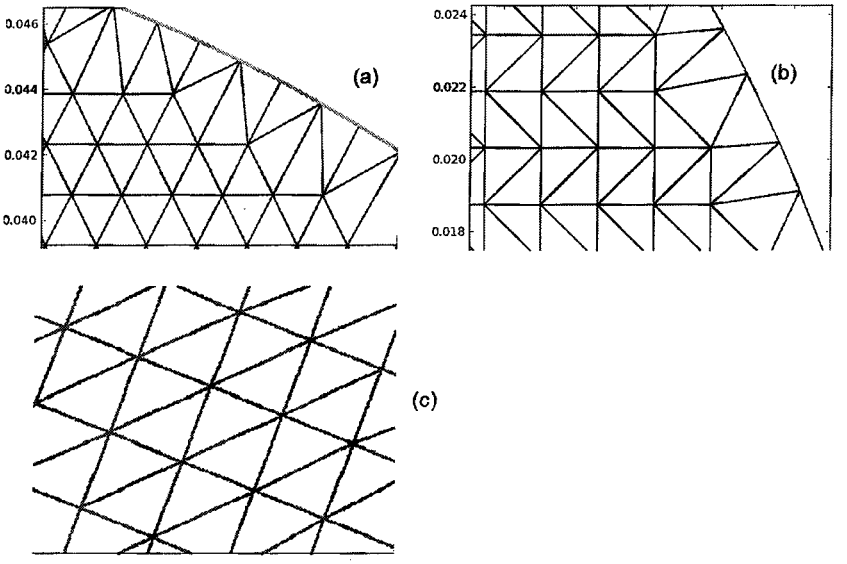

Figure 4-13 Triangle-shape used for FEM mesh

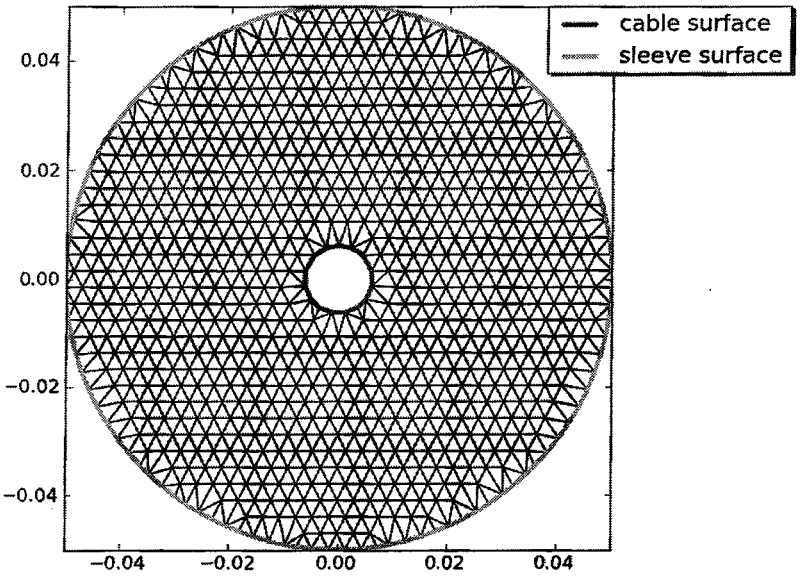

Figure 4-14 Mesh of the snow sleeve used in FEM

b. FVM

The element used for FVM is shown in **Figure 4-12**(B). To calculate a vector for a given node, however, the four adjacent nodes must be known. It may be assumed that there exists a virtual element, usually a rhombic shape, consisting of five nodes for each node which is in the process of being solved.

2. Select Interpolation or Shape Functions

- FEM

The next step is to determine the matrix equations which express the properties of the individual elements by forming an element Left Hand Side (LHS) matrix and load vector. For a liner element shown in **Figure 4-12** A,

$$\bar{\psi} = [N_i \quad N_j \quad N_k]\begin{Bmatrix}\psi_i \\ \psi_j \\ \psi_k\end{Bmatrix} \qquad \textbf{Equation 4-10}$$

the governing **Equation 4-3** can be written as

$$f(\psi) = \frac{\partial}{\partial x}\left[Kk_{rw}\left(\frac{\partial \psi}{\partial x}\right)\right] + \frac{\partial}{\partial z}\left[Kk_{rw}\left(\frac{\partial \psi}{\partial z} + 1\right)\right] - C\frac{\partial \psi}{\partial t} = 0 \qquad \textbf{Equation 4-11}$$

The Galerkin method requires that the following expression is satisfied.

$$\int_{\Omega} w_k f(\bar{\psi})\, d\Omega = 0 \qquad \textbf{Equation 4-12}$$

where the weight $\mathbf{w_k}$ is replaced by the shape functions at the nodes. Integration by parts is often essential when dealing with second-order derivatives.

$$-\int_{\Omega} Kk_{rw}\left(\frac{\partial N_l}{\partial x}\ \frac{\partial N_m}{\partial x}+\frac{\partial N_l}{\partial z}\ \frac{\partial N_m}{\partial z}\right)\{\overline{\psi_m}\}\,d\Omega-\frac{Kk_{rw}}{2}[c_i\quad c_j\quad c_k]$$
$$+\int_{S} N_l\left[Kk_{rw}\left(\frac{\partial\bar{\psi}}{\partial x}\right)\right]dS+\int_{S} N_l Kk_{rw}\,dS-\int_{\Omega} N_l\,C\frac{\partial\bar{\psi}}{\partial t}d\Omega \qquad \textbf{Equation 4-13}$$
$$=0$$

- FVM

FVM can be considered a further refined version of FDM and has become widely used in computational fluid dynamics. The vertex-centered finite volume technique is very similar to the linear finite element method.

FVM requires that the following expression is satisfied

$$\int_{\Delta V} f(\psi)\,dV=\int_{\Delta V}\left\{\frac{\partial}{\partial x}\left[Kk_{rw}\left(\frac{\partial\psi}{\partial x}\right)\right]+\frac{\partial}{\partial z}\left[Kk_{rw}\left(\frac{\partial\psi}{\partial z}+1\right)\right]-C\frac{\partial\psi}{\partial t}\right\}dV \qquad \textbf{Equation 4-14}$$
$$=0$$

where V refers to a control volume.

For a volume element, the local equation can be written as:

$$a_p\psi_P-a_W\psi_W-a_E\psi_E-a_N\psi_N-a_S\psi_S=S \qquad \textbf{Equation 4-15}$$

where

a_W	$\frac{Kk_{rw}}{\delta x_{WP}}$	a_N	$\frac{Kk_{rw}}{\delta z_{PN}}$
a_E	$\frac{Kk_{rw}}{\delta x_{PE}}$	a_S	$\frac{Kk_{rw}}{\delta z_{SP}}$
a_P	$a_W+a_E+a_S+a_N$		

S	$-[(Kk_{rw})_n - (Kk_{rw})_s] + \int_{\Delta S} \left\{C\frac{\partial \psi}{\partial t}\right\} dS$

3. Time Discretization

Choosing an integration method for extrapolating the state variables is an extremely important task, and may prove overly difficult for such non-linear systems as the one observed. It must be ensured that the system is stable over time as well as physically correct while keeping the storage requirements and computational costs down. Unfortunately, it is difficult to find an effective way for two- or three-dimensional modeling.

Using the Taylor series, the pressure head ψ can be written as

$$\psi^{n+1} = \psi^n + \Delta t\frac{\partial \psi^n}{\partial t} + \frac{\Delta t^2}{2}\frac{\partial^2 \psi^n}{\partial t} + \cdots \qquad \textbf{Equation 4-16}$$

If second- and higher- order terms in the above equation are disregarded, then

$$\frac{\partial \psi^n}{\partial t} \approx \frac{\psi^{n+1} - \psi^n}{\Delta t} + O(\Delta t) \qquad \textbf{Equation 4-17}$$

which is the first accurate order in time. If weighting parameter β is introduced to the above equation, then

$$\psi^{n+\beta} = \beta\psi^{n+1} + (1-\beta)\psi^n \qquad \textbf{Equation 4-18}$$

- FEM

Substituting **Equation 4-18** into **Equation 4-13**, the following expression may be obtained as

$$[C_m]\left\{\frac{\psi^{n+1}-\psi^n}{\Delta t}\right\}+[K_{km}]\{\psi\}^{n+\beta}=\{f\}^{n+\beta} \qquad \textbf{Equation 4-19}$$

Thus,

$$[C_m]\left\{\frac{\psi^{n+1}-\psi^n}{\Delta t}\right\}+[K_{km}]\{\beta\psi^{n+1}+(1-\beta)\psi^n\} = \beta\{f\}^{n+1}+(1-\beta)\{f\}^n \qquad \textbf{Equation 4-20}$$

The above equation can be rearranged as:

$$([C_m]+\beta\Delta t[K_{km}])\psi^{n+1} = ([C_m]-(1-\beta)[K_{km}]\Delta t)\psi^n + \Delta t(\beta\{f\}^{n+1}+(1-\beta)\{f\}^n) \qquad \textbf{Equation 4-21}$$

where

$$C_m^{n+\beta} = \beta C_m^{n+1}+(1-\beta)C_m^n$$
$$K_{km}^{n+\beta} = \beta K_{km}^{n+1}+(1-\beta)K_{km}^n \qquad \textbf{Equation 4-22}$$

- FVM

Substituting **Equation 4-18** into **Equation 4-15** the matrix equation may be given as:

$$[K_m]\{\psi\} = \{f\} \qquad \textbf{Equation 4-23}$$

where

$$[K_m] = \left[\left(a_p-\frac{\psi_P}{\Delta t}[C_m]\right) \quad -\beta a_W \quad -\beta a_E \quad -\beta a_S \quad -\beta a_N\right]$$
$$\{\psi\} = [\psi_P \quad \psi_W \quad \psi_E \quad \psi_S \quad \psi_N]^T$$
$$\{f\} = (1-\beta)\left(a_W\psi_W^0+a_E\psi_E^0+a_N\psi_N^0+a_S\psi_S^0-a_P\psi_P^0\right)+\beta[(Kk_{rw})_n-(Kk_{rw})_s] + (1-\beta)[(Kk_{rw}^0)_n-(Kk_{rw}^0)_s]-\frac{\psi_P^0}{\Delta t}[C_m]$$

$$C_m^{n+\beta} = \beta C_m^{n+1} + (1-\beta)C_m^n$$

4. Solution to the system of equations

The nodal values of the field variable may now be found using the algebraic equations obtained from **Equation 4-21** or **Equation 4-23**.

4.4.3 Boundary Conditions

1. Outer Surface of Sleeve

As discussed in a previous chapter, the heat flux along the snow sleeve surface is not a constant but a continuous variation affected by air velocity, shape of the sleeve, surface roughness, and so forth. A typical Heat Transfer Coefficient (HTC) distribution is provided in **Figure 2-8**.

There is heat flux along the snow surface and the heat for an element resulting from this heat flux, Q_e, is calculated by

$$Q_e = h_{ae}A_e(T_a - T_m) \qquad \textbf{Equation 4-24}$$

where h_{ae} is the forced convection heat transfer coefficient of air for an element (W/m^2K), A_e is the surface area of this element (m^2), T_a is the air temperature (°C), and T_m is the melting point of ice, which is 0°C in this study.

Snow melts due to the heat flux

$$m_w = \frac{Q}{L_w} \qquad \textbf{Equation 4-25}$$

where m_w is the mass flow of melted water (kg/s), and L_w is the latent heat of water (334,000J/kg).

The specific discharge v_w (m/s) of melted water can be obtained by

$$v_w = \frac{m_w}{\rho_w A} = \frac{h_a(T_a - T_m)}{L_w \rho_w} \qquad \textbf{Equation 4-26}$$

where ρ_w is the density of water (1000kg/m^3). A sample of water flux data for an air flow at 2°C and at 4m/s velocity is shown in **Figure 4-15**.

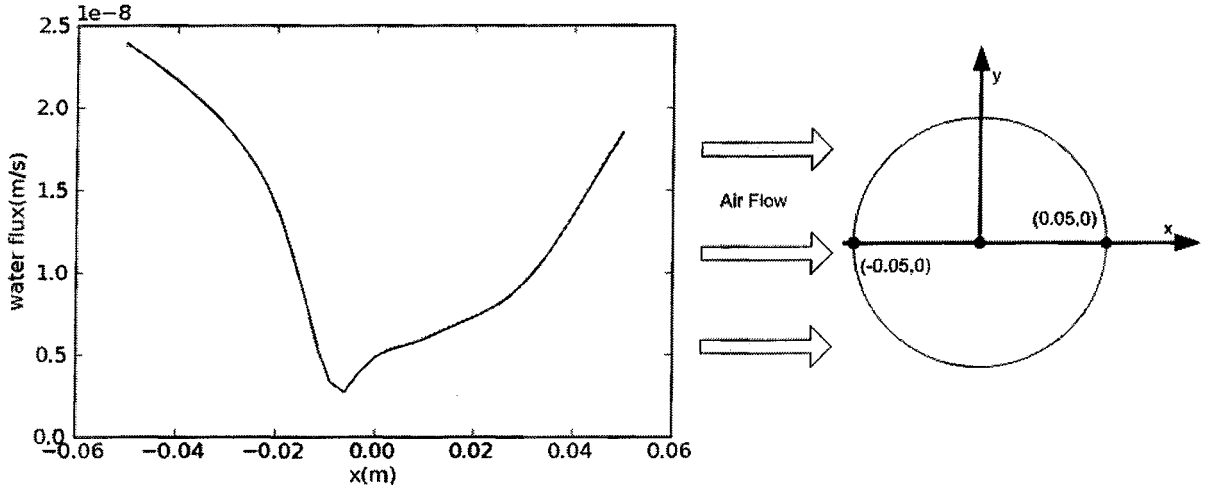

Figure 4-15 Water flux at an air temperature of 2°C and a velocity of 4m/s (the origin coordinates are at the sleeve center point)

2. The inner surface of a snow sleeve

Joule heat, Q_J for a line conductor carrying electric current I can be obtained through **Equation 3-27**.

The specific discharge v_w (m/s) at the inner surface of a snow sleeve can be obtained by

$$v_w = \frac{Q_j}{L_w \rho_w} \frac{1}{\pi d_c} \qquad \textbf{Equation 4-27}$$

where d_c is the diameter of the cable.

A constant heat flux from a cable surface is assumed in this study. The diameter of the cable is 12.5 mm.

Table 4-1 Heat and water flux at the conductor surface

Current (A)	Heat flux on cable surface (W/m)	q (m/s)
25	0.188	1.43E-8
50	0.75	5.72E-8
75	1.688	1.29E-7
100	3.0	2.29E-7

4.4.4 Residual Water Height

The residual water pressure within the snow is caused by the interaction between the contacting surfaces of water and ice particles.

The porosity of snow can be calculated using the following equation:

$$\phi = \frac{V_s - V_i}{V_s} = \frac{\rho_i - \rho_s}{\rho_i} \qquad \textbf{Equation 4-28}$$

where ρ_s and ρ_i are the density of snow and ice, respectively, and V_s and V_i are the volumes of snow and ice particle, respectively. The inter gaps between snow grains may be considered rectangular holes, as shown schematically in **Figure 4-16**. When snow and ice display densities of 500 kg/m^3 and 900 kg/m^3 and the porosity is 0.45 for the snow and ice

mixtures, the length ratio of air gap l_a and snow grains l_i is 0.9, as determined from **Equation 4-28**.

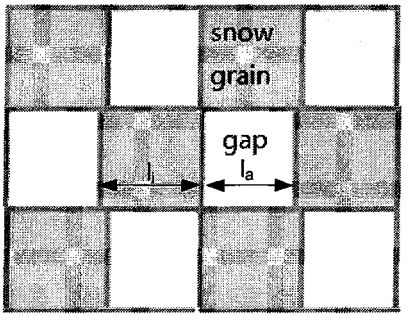

Figure 4-16 Schematic of air gap within snow

The height of water, h_c, rises due to the capillary force in the gap hole and may be computed as

$$h_c = \frac{2(l_i + l_a)\gamma\cos\vartheta}{\rho_w g l_i l_a} \qquad \textbf{Equation 4-29}$$

where γ is the liquid-air surface tension (J/m^2), ϑ is the contact angle between ice and water, ρ_w is the density of liquid water (1000 kg/m^3), g is the acceleration due to gravity (9.81 m/s^2), l_i and l_a are the lengths of the snow grain and gap (m), respectively. Height h_c for different types of snow is shown in **Table 4-2**.

Table 4-2 Microstructure of snow and residual water height

Length of snow grain (mm)	Length of gap hole (mm)	Height (mm)
0.5	0.45	57.3
0.8	0.72	35.8

1	0.9	28.6
2	0.18	14.3

The second type with h_c = 35.8 mm was widely used for most of the previous research into melted water percolation within snow. Values between -30 mm to -40 mm for hydraulic head were proposed by Wankiewicz (1979) for h_c used in the Brooks and Corey model. The range of the values is consistent with the one presented in this study.

4.5 Water Percolation without Heat Exchange

Two methods, FEM and FVM were implemented and their results show a good agreement. Therefore, only results from FEM were shown in subsequent sections.

For this typical simulation sample, it is assumed that neither water flow nor heat flux occurs on the outer and inner surfaces of the snow sleeve.

4.5.1 Initial State

A snow sleeve can be considered to be in a steady-state when it is available for testing.

- Snow is homogeneous and isotropic in its initial state.
- A certain amount of melted water exists and is distributed evenly within the snow.

Parameters of snow in its initial state are shown in **Table 4-3.**

Table 4-3 Snow properties in the initial state

Parameter	Value
Density (kg/m3)	500

Porosity	0.5
Residual saturation S_r	0.05
Air entity pressure head, h_c (mm)	36
Liquid water content (kg/kg)	10%
Volume water content (VWC) (m^3/ m^3)	5%

4.5.2 Water Percolation within Snow

Theoretically, melted water may move upward in porous media. The size of the air gap holes in the snow is usually big enough to prevent the melted water from moving upward in a snow sleeve.

The variation in water content, with respect to time, at a given location within a snow sleeve, is shown in **Figure 4-17**. It may be observed that there is an appreciable change in the value of the water content in the early stages beyond which point the value remains virtually unchanged.

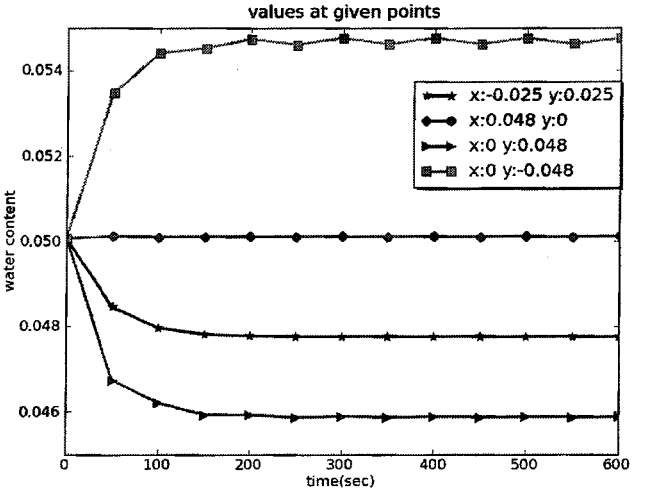

Figure 4-17 Volume water content varies with time at given locations

Two-dimensional variations of volume water content in a FEM simulation process are shown in **Figure 4-18**. The following phenomena may be observed from the figure.

- Water flow is symmetrical along the vertical orientation due to the geometry of the snow sleeve.
- Water tends to move downward continually and accumulates in the lower portion of a snow sleeve.
- Horizontal water flow occurs as a result of the geometry of the cable in this particular simulation.

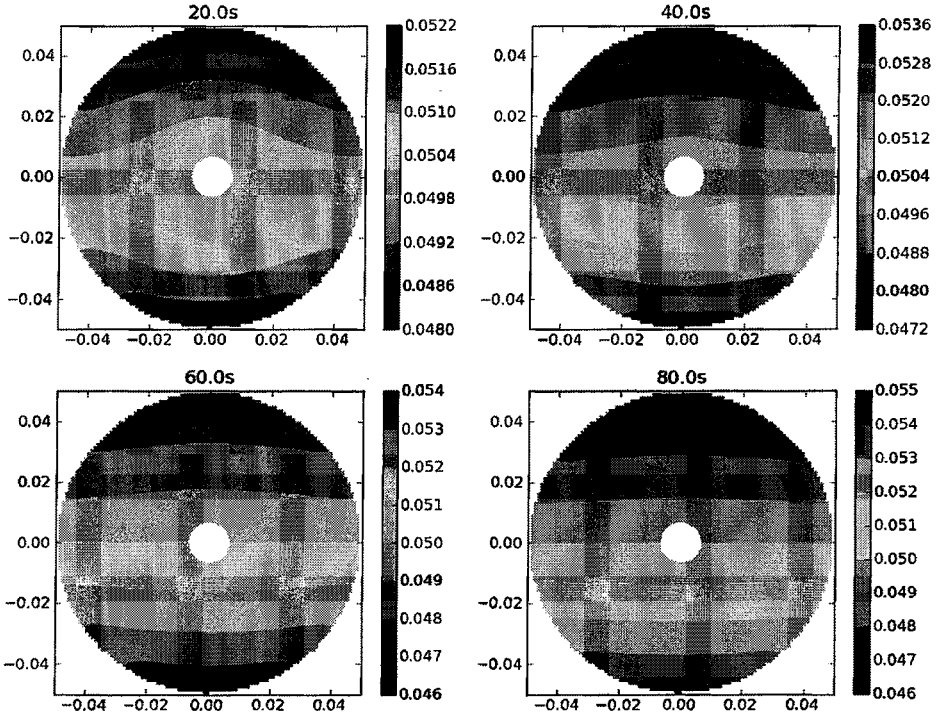

Figure 4-18 VWC distribution with respect to time. No water flows into or out of the sleeve

4.5.3 Quasi-Steady State

A quasi-steady state may be attained considering that either no water flow at all occurs or that all the water flow in the snow maintains a constant rate. In other words, a quasi-steady state will be reached as water begins to seep out of the snow sleeve if ice particle and ice matrix metamorphism is disregarded. In the quasi-steady state, a saturated snow zone will clearly be observed during experiments. **Figure 4-19** shows the saturated snow zone within a snow sleeve.

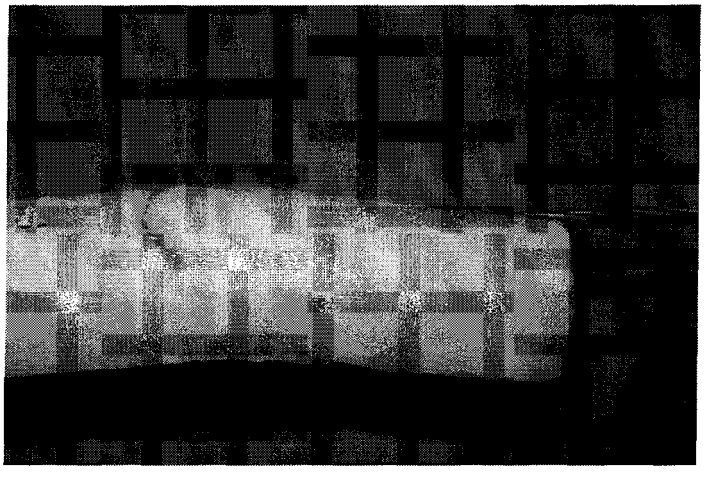

Figure 4-19 Saturated zone: lower portion of sleeve. Photo taken at CIGELE, 26 January, 2009.

Water residua occur due to both the capillary action and the water pressure gradient. The residua water distribution along a vertical orientation is shown in **Figure 4-20**.

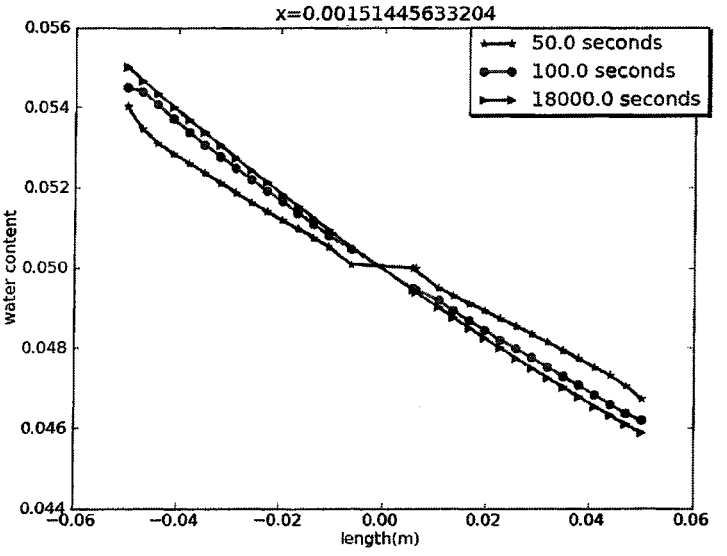

Figure 4-20 Volume water content distribution at a vertical orientation

4.6 Effects of Wind Speed and Temperature

In this section, a snow sleeve with a smooth surface is modeled and solved by FVM and FEM. The HTC distribution comes from a previous chapter. An example of HTC distribution around a smooth cylinder is shown in **Figure 2-8.**

A set of air velocities and temperatures were applied in modeling.

Air velocity (m/s)	2, 4, 6, 8
Air temperature (°C)	1, 2, 3, 4

4.6.1 Water Percolation in a Snow Sleeve

Variations in the volume water content occurring with time are shown in **Figure 4-21**. The variations and the rates of the water content at some locations are shown in **Figure 4-22** and in **Figure 4-23**, respectively.

It may be observed that

- the water flux varies at different positions on the surface of a snow sleeve.

  The value of melted water varies along the snow surfaces because of the uneven distribution of the heat flux, as shown in **Figure 4-15**. It may be observed that the melted water flux reaches its maximum near the front stagnation point.
- the water flow decreases with time.

The water contour becomes flat, as shown in **Figure 4-20**, and it may be seen that the water content increases with time until quasi-steady state is attained in **Figure 4-23**. Under windy conditions, water percolation in a snow sleeve is a combination of two types of water flow: the initial water flow, as discussed in Chapter 4.5, and the melted water flow due to forced convection.

- The overall water percolation also reaches a quasi-steady state eventually, and the lower part of the snow sleeve becomes saturated while the surplus water seeps out of the sleeve.

  This quasi-steady state looks like the final state under no wind conditions, but these two states are totally different. A constant water percolation exists as wind causes

continuous snow melting, while no water percolation exists under the latter condition.

- The lower portion of the snow sleeve became saturated with water as a result of water accumulation as shown in **Figure 4-22**, and the saturated water level in snow rose with time until surplus water began to seep out. Then the water flow in snow sleeve reached quasi-steady state: the water content within snow sleeve remained constant as well as all the water flow in the snow maintains a constant rate (shown in **Figure 4-22** and **Figure 4-23**).
- It may be observed in **Figure 4-22** that the water flow increases slightly before the quasi-steady state was reached.

  As the water level in snow rises, the hydro conductivity increases due to the increasing of local density and water content, and then leads to a slight increase in the water flow.
- It may be found that water migrates faster in a lower location than it does in an upper location most of time (**Figure 4-23**).

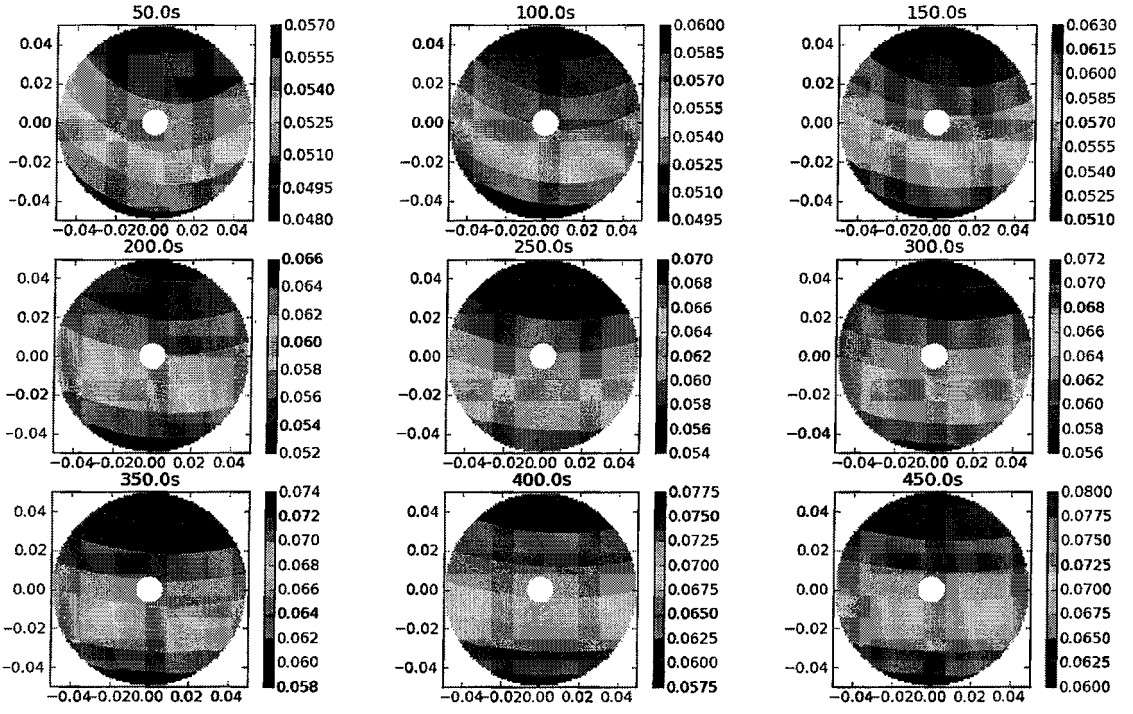

Figure 4-21 VWC distributions vary with time at an air velocity of 4m/s and an air temperature of 2°C

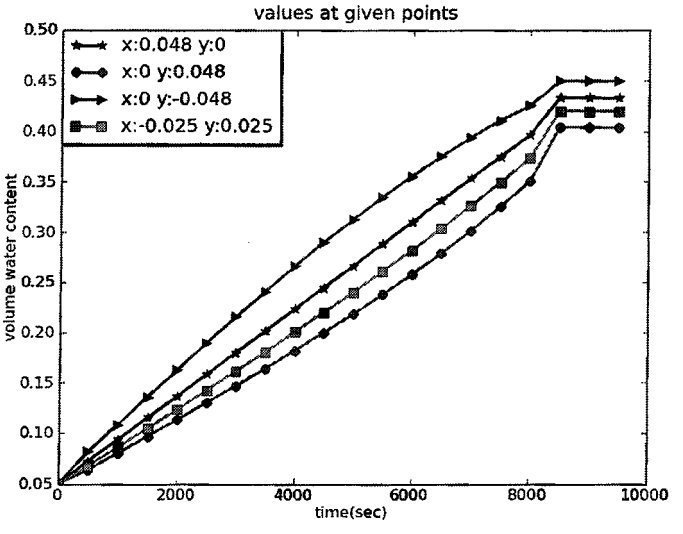

Figure 4-22 VWC at given locations vary with time at an air velocity of 4m/s and an air temperature of 2°C

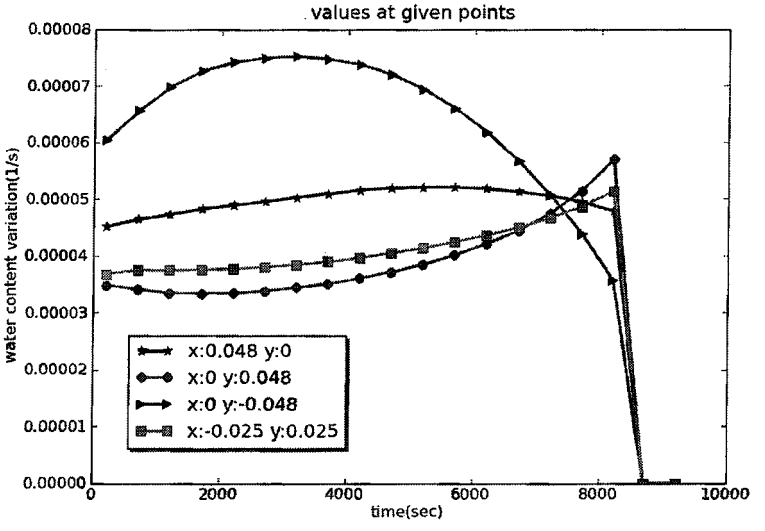

Figure 4-23 Water content variation at given locations at air velocity of 4m/s and an air temperature 2°C

4.6.2 Effects of Air Velocity

Figure 4-24 shows the water content distribution at 50 s and various air velocities. Water content variations at a given location are plotted in **Figure 4-25**. It may be observed that water flow increases with air velocity, which is consistent with the hypothesis. It may be seen that the water content increases almost linearly until it reaches the maximum value, as shown in **Figure 4-25**.

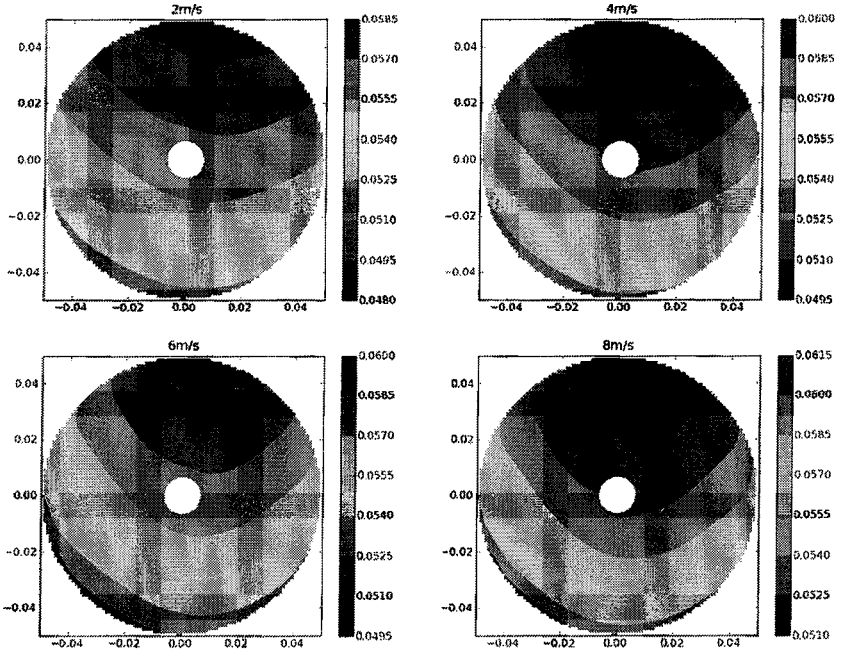

Figure 4-24 VWC distribution at 50 s at a series of air velocities and an air temperature of 3°C

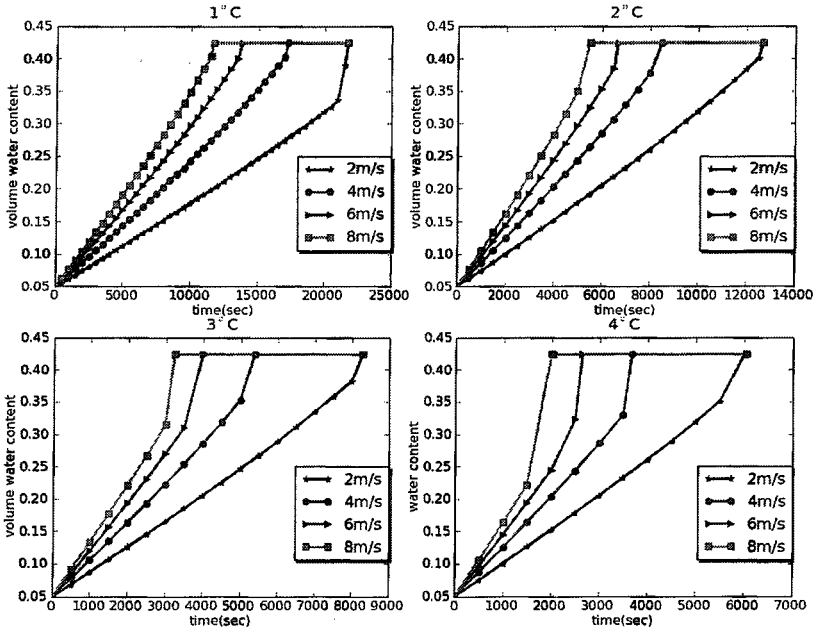

Figure 4-25 Water content at a given location (x = 0.025, y = 0.025) varies at different air velocities and temperatures

Figure 4-26, below, shows the time required for water percolation to reach a quasi-steady state at a given set air temperature. It may be found that:

- at the same temperature, the time needed to reach quasi-steady state decreases with the air velocity.
- at higher temperatures, the effects of the air velocity on water percolation become more obvious. The time needed to attain quasi-steady state decreases to 48% and 66% of its initial value when the air velocity increases from 2m/s to 8m/s at 1°C and 4°C.
- at lower air velocities, the effects of air velocity become more evident.

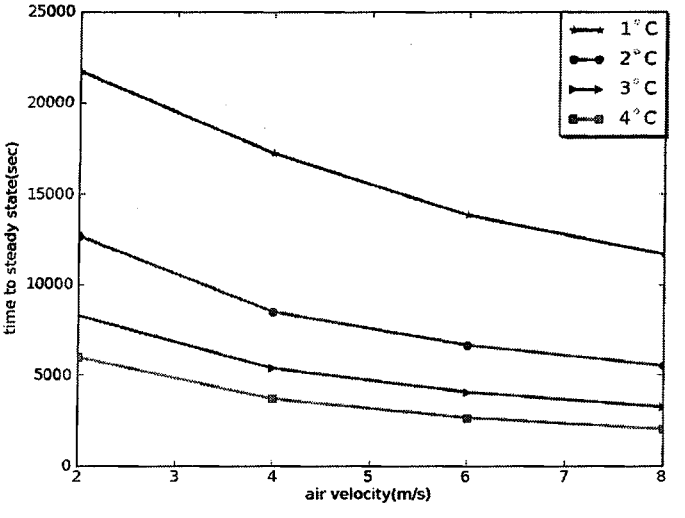

Figure 4-26 Time required to reach quasi-steady-state under different air velocities

4.6.3 Effects of Air Temperature

The melting rate of snow is proportional to the air temperature. **Figure 4-27** shows the water content distribution at different air temperatures at 100 s. It may clearly be seen that higher air temperatures cause an increasingly uneven water distribution.

It may be observed in **Figure 4-28** that, at a given location, the water content increases more rapidly with the air temperature, that is to say, there is a stronger water flow.

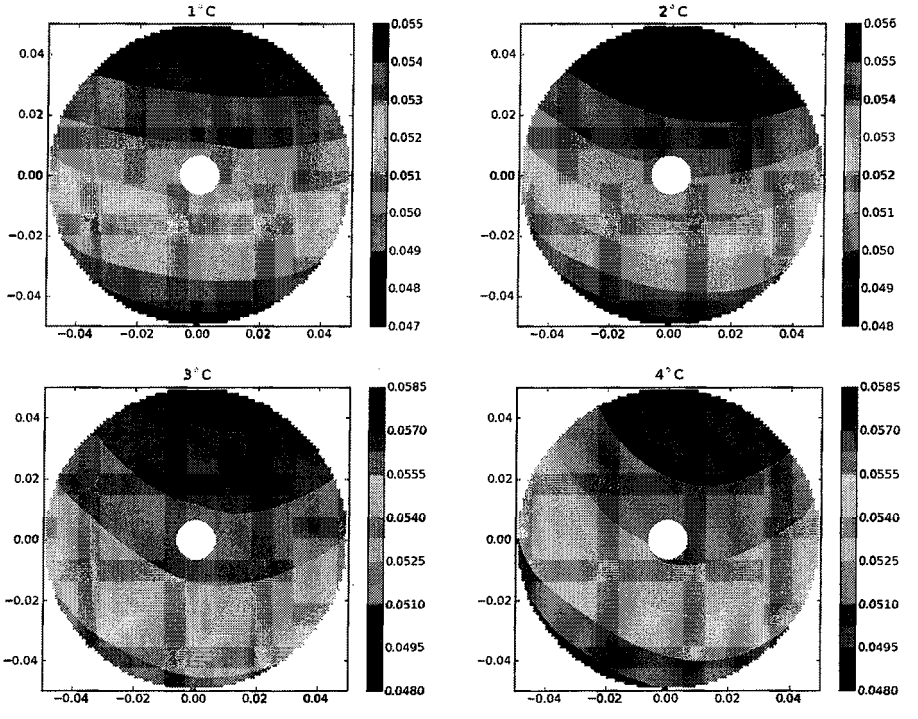

Figure 4-27 VWC distribution at 50 s under a series of air temperatures and an air velocity of 2m/s

Figure 4-29 shows the time required for water percolation to reach a quasi-steady state at set air velocities. It may be found that:

- at the same air velocity, the time required to reach a quasi-steady state decreases with the temperature;
- at a higher air velocity, the effects of the air temperature become more obvious, thus the time decreases to 73% and 83% of its initial value, respectively, when the air temperature increases from 1°C to 4°C at an air velocity of 2 m/s and 4 m/s;
- at a lower air temperature, the effects of the air velocity also become more evident.

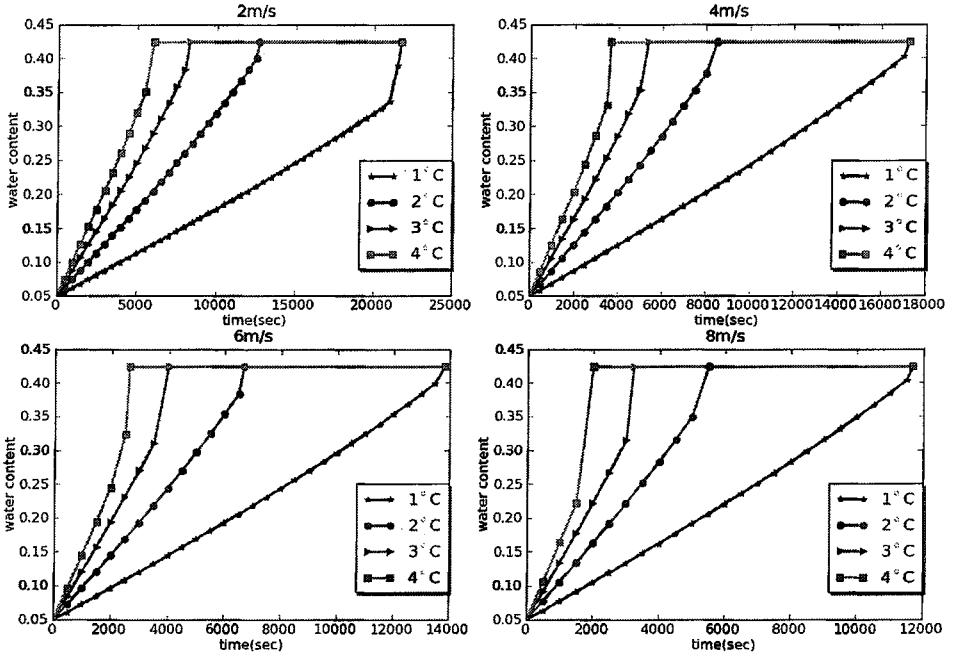

Figure 4-28 VWC at a given location (x = 0.025, y = 0.025) varies at different air temperatures and air velocities

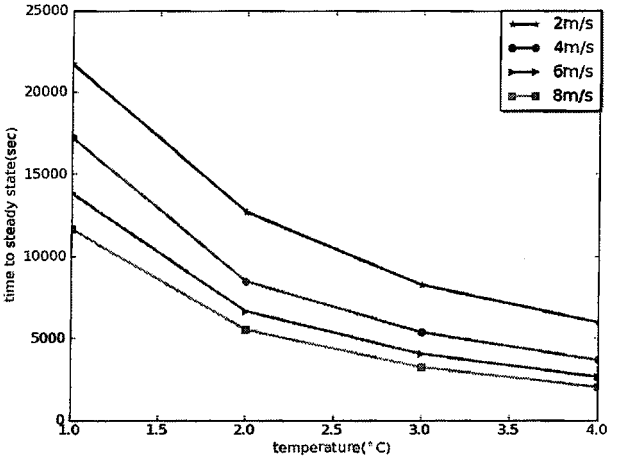

Figure 4-29 Time required to reach quasi-steady-state in different temperature conditions

4.7 Effects of Electric Current

A conductor with electric current exposed in quiescent air will be the subject of discussion in this subsection.

4.7.1 Water Flow in a Snow Sleeve

The variation with time in volume water content distribution is shown in **Figure 4-30**. The variation rates at some locations are plotted in **Figure 4-31**. It will thus be seen that:

- water percolation occurs mostly in the centre area close to the cable surface;
- the rate of the water content variation has the higher value at an early stage due to the effect of initial water flow;
- water percolation only occurs in the lower part of a snow sleeve when the initial and the melted water flows reach a quasi-steady-state;

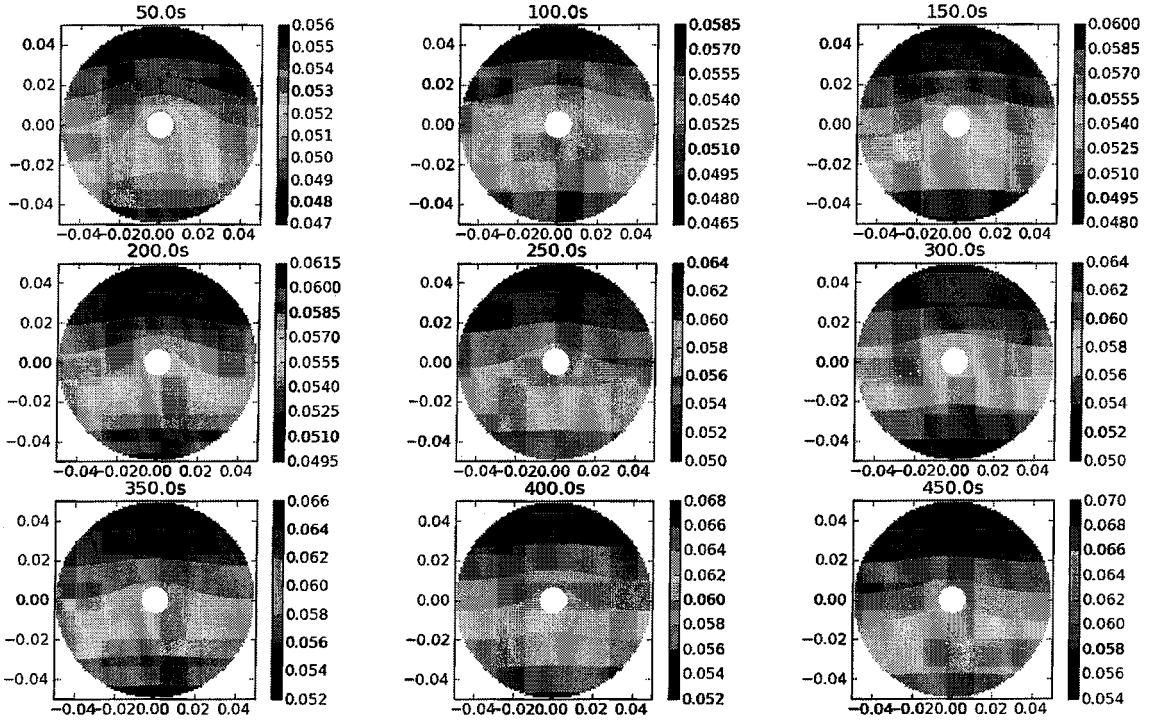

Figure 4-30 Volume water content distribution varies with time in seconds at air temperature of 0°C and electric current of 50A

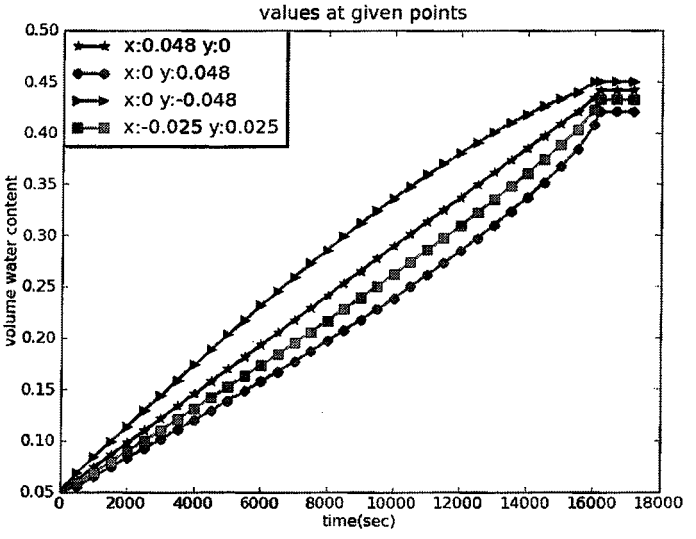

Figure 4-31 VWC at a given locations varies with time at an air velocity of 0m/s, air temperature 0° and electric current 50A

- the water content in the lower part of a snow sleeve increases at a faster rate than it does in the upper portion, as shown in **Figure 4-31**.

4.7.2 Effects of Electric Current

Figure 4-32 shows VWC distribution at 50 s when a cable carries different electric currents. The VWC variations with time at some locations are plotted in **Figure 4-33,** from which the following may be observed:

- the larger the value of the electric current is, the more intense is the water flow within the snow;
- the water content is almost linearly proportional to the electric current as the electric current is greater than 50 A.

From **Table 4-4** it may be seen that the time required to reach the quasi-steady state decreases non-linearly with respect to the electric current.

Table 4-4 Time to quasi-steady state under electric heating

Electric current (A)	Time to quasi-steady state (seconds)
25	55914
50	16420
75	7068

In an experimental observation, snow shedding occurred fairly quickly when the electric current was high. It was possible for several snow-shedding events to be observed in one hour in view of the fact that the electric current was higher than 75 A.

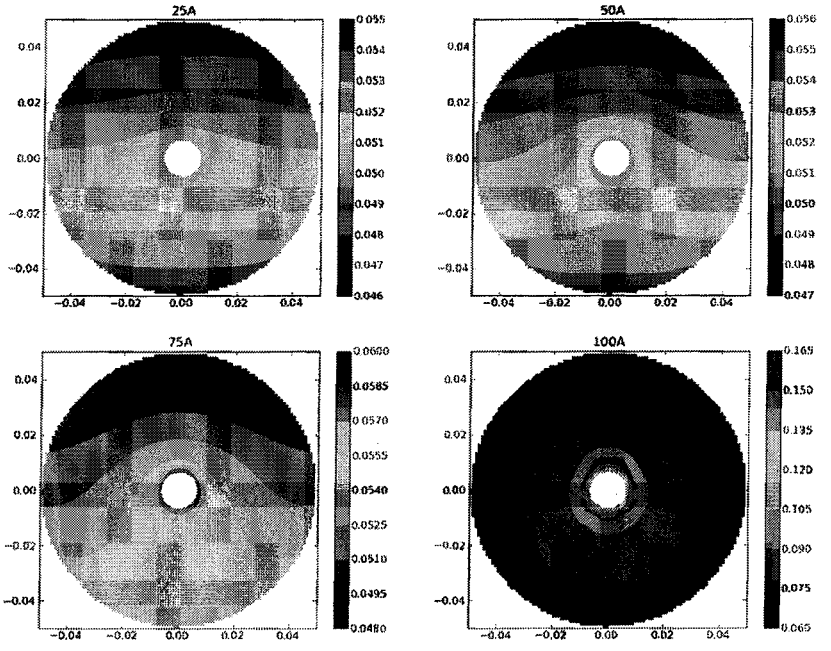

Figure 4-32 VWC distribution at 50s under a series of electric currents, an air temperature of 0°C and air velocity of 0m/s

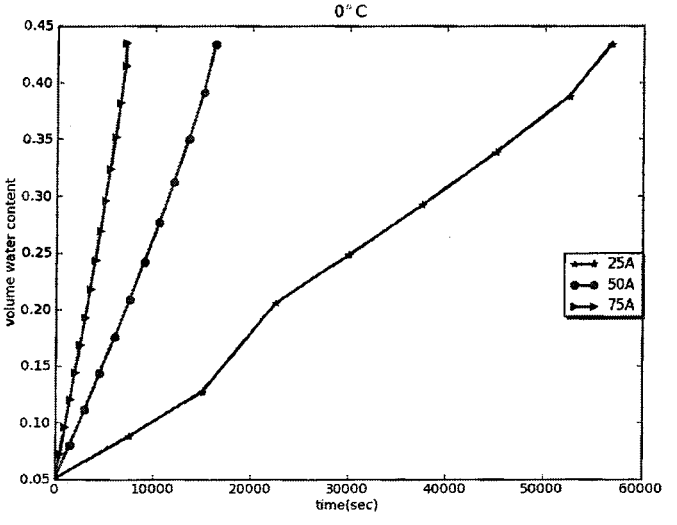

Figure 4-33 VWC at a given location (x = 0.0318, y = 0.0227) varies with time for different electric currents at an air velocity of 0m/s and air temperature of 0°C

4.8 Comprehensive Effects of Wind and Electric Heating

If Joule heat is chosen to get rid of snow from a line conductor, the forced heat convection and the electric heating are always concurrent and will affect the process of snow melting and water percolation. In this subsection, the comprehensive effects of wind and Joule heat may be shown modeled and solved by FEM.

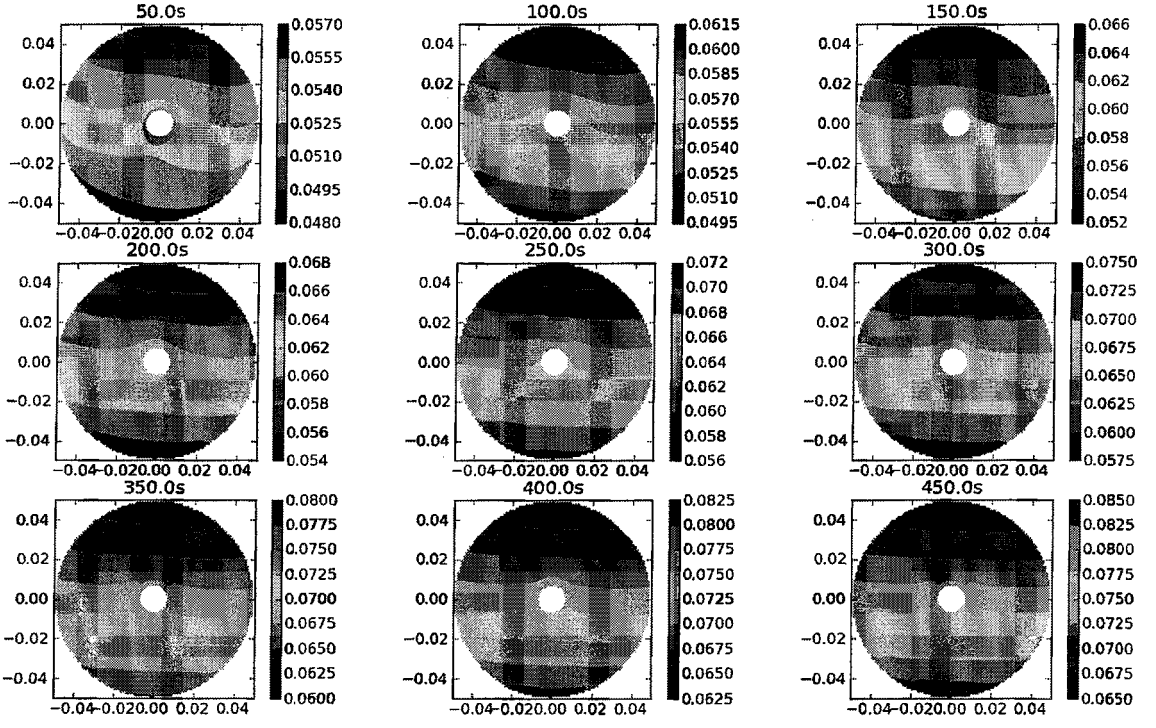

Figure 4-34 Water content distribution varies at a set of time interval in seconds at an air temperature of 2°C, an air velocity of 2m/s and an electric current of 50A

A typical water percolation can be seen in **Figure 4-34** and **Figure 4-35**. The effect of electric heating concentrates on the cable surface. The uneven water distribution can be seen clearly in the first several plots shown in **Figure 4-34**. Water distribution eventually

becomes horizontally even because the permeability of snow is extensive enough to let the entire water content move downwards. It will also be seen from **Figure 4-35** that the water content at a given location varies nonlinearly.

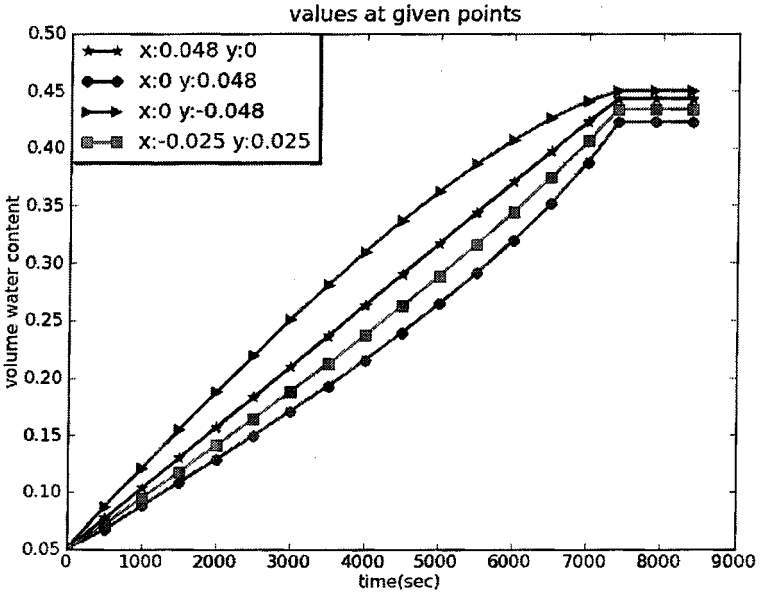

Figure 4-35 The water content at a given location varies with time at an air velocity of 2m/s, an air temperature of 2°C and an electric current of 50A

The time for water percolation to reach a quasi-steady state at an air temperature of 2°C with a series of air velocities and electric currents (are/is) shown in **Figure 4-36** and **Table 4-5**. It may be seen that the time required to attain a quasi-steady state decreases as and the electric current, the air temperature and velocity increase.

The time required to reach a quasi-steady state drops to approximately one hour for an electric current of 75 A.

Table 4-5 Time required for quasi-steady-state at given air temperatures and a given set of air velocities and electric currents

Temperature	Velocity	0A	25A	50A	75A	100A
1°C	2m/s	21724.59	18230.19	10420	5325.439	365.0972
	4m/s	17233.99	13780.44	8900	4728.439	341.0972
	6m/s	13826.86	11458.19	7622.606	4353.171	326.0972
	8m/s	11661.17	9942.194	6832.194	4054.171	313.0972
2°C	2m/s	12675.47	10665.77	7186.194	4197.439	321.0972
	4m/s	8474.439	7496.194	5583.194	3501.439	286.0972
	6m/s	6637.439	6022.775	4693.194	3097.439	263.0972
	8m/s	5504.439	5051.775	4075.194	2805.097	246.0972
3°C	2m/s	8260.171	7342.775	5496.194	3458.439	284.0972
	4m/s	5348.171	4948.439	3997.194	2767.439	247.0972
	6m/s	4036.171	3783.439	3190.194	2329.439	220.0972
	8m/s	3220.171	3055.439	2637.194	2030.439	205.0972
4°C	2m/s	5962.742	5462.439	4339.194	2956.097	257.0972
	4m/s	3658.742	3454.171	2959.775	2211.439	215.0972
	6m/s	2628.813	2508.171	2212.439	1830.439	193.0972
	8m/s	1998.194	1917.171	1723.439	1460.194	175.0972

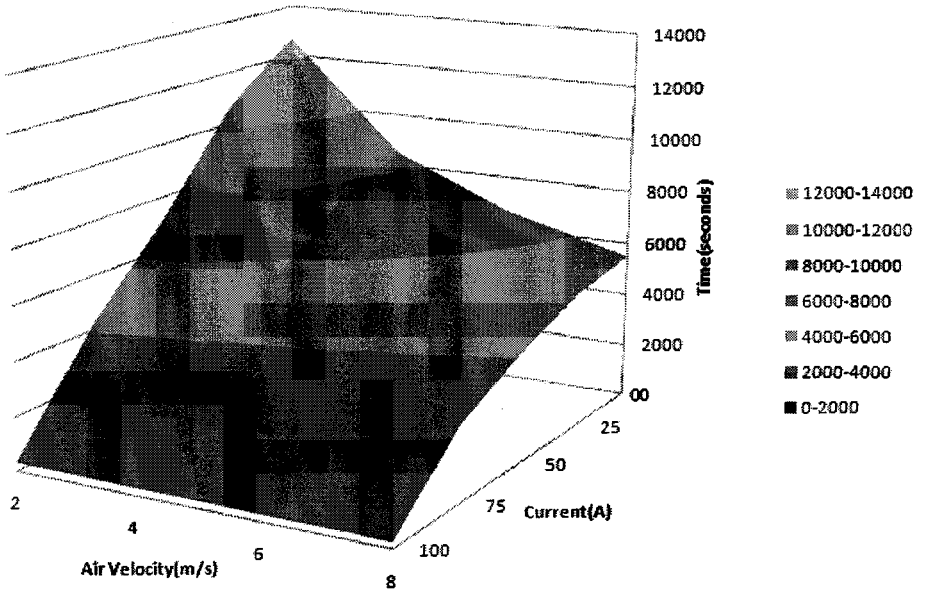

Figure 4-36 Time required for quasi-steady state at an air temperature of 2°C and a given set of air velocities and electric currents

4.9 Effects of Rough Surface

The roughness of a snow surface is caused by wind, uneven evaporation or uneven melting. Lacroix *et al.* (2008) investigated a snow pack and found that the roughness of snow largely varied due to the weather and geographical conditions. A typical example of the local heat-transfer distribution around a rough surface cylinder was plotted for Reynolds number 22222 in **Figure 2-13**.

Typical water content variation for rough surfaces is shown plotted in **Figure 4-37**. The water concentrates in the 40° ~70° range from the front stagnation point.

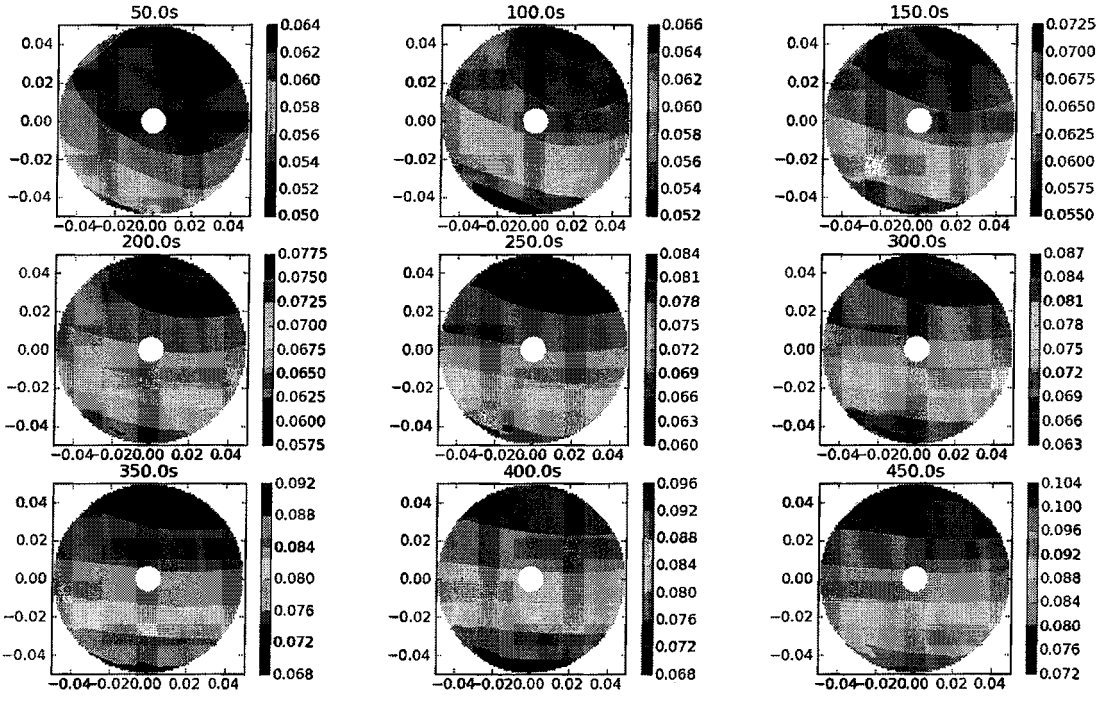

Figure 4-37 VWC variation with time in seconds at roughness 0.035 at an air velocity of 3 m/s and a temperature of 2°C

Figure 4-38 shows water distribution at 100 s for a snow sleeve with various surface roughnesses. It may be seen from the figure that the water distribution becomes more uneven as the surface roughness increases.

The time required to reach the quasi-steady state under a set of roughness values is listed in Table 4-6. It may be observed that the time decreases as the surface roughness increases. The variation is small considering that the roughness is less than 0.025. The time required to reach the quasi-steady state decreases sharply as the roughness grows greater than 0.03 as a result of the abrupt increase in the heat transfer as shown in **Figure 2-13.**

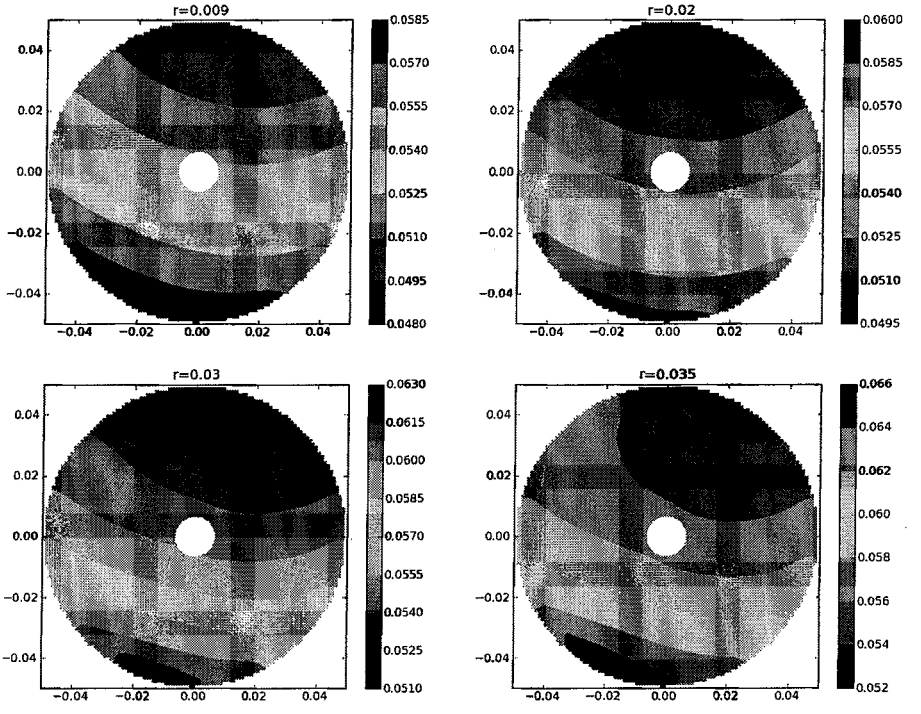

Figure 4-38 Water content variation at 100 s for different roughness ***r*** at an air velocity of 3 m/s and a temperature of 2°C

Table 4-6 Time required to reach a quasi-steady-state under different roughnesses (at a velocity of 3 m/s and a temperature of 2°C).

Roughness (10^{-3})	Time to steady-state (seconds)
0	10822
9	10179
20	9457
25	9551
30	4144
35	2551

4.10 Effect of Snow Types

The shape of snow grains in the snow which had accreted on the cable surface is different from those in fresh snow because of the compacting force resulting from wind.

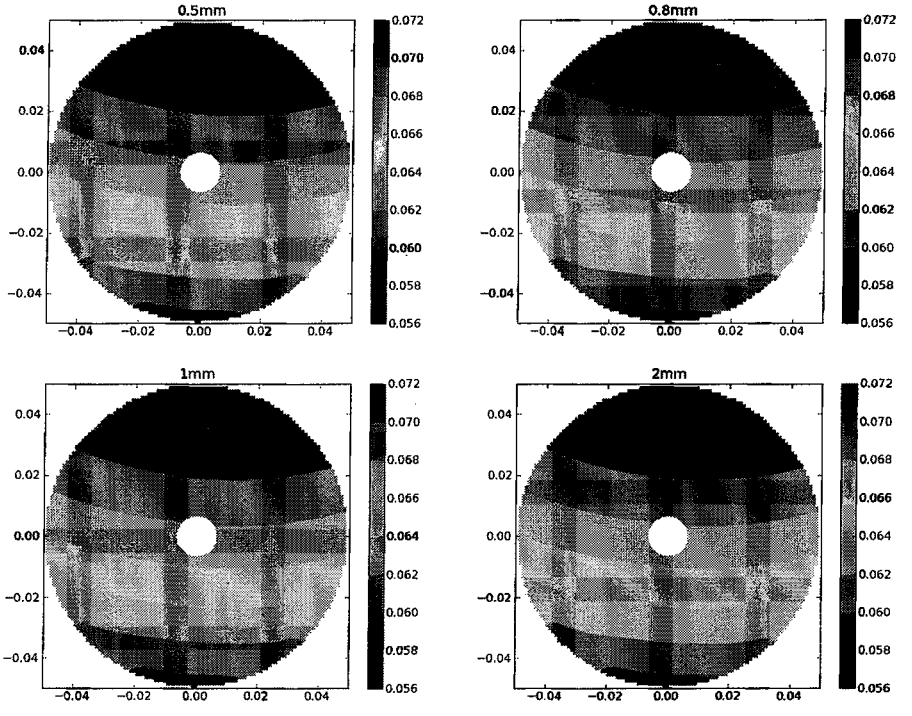

Figure 4-39 VWC distribution at 300s for different snow grain size at an air temperature of 2°C and a velocity of 4 m/s

The water distribution for different snow types at 300 s is shown in **Figure 4-39**.

The data provided in **Table 4-7** include the diameters of four kinds of snow grains, the residual water level of the quasi-steady state and the time required to reach the quasi-steady

state. It should be concluded from this that this required time decreases as the diameter of the snow grains increases. It will also be seen that the difference between such times is non-significant. Thus, the effects due to snow properties may be disregarded in most cases.

Table 4-7 Time to quasi-steady state at an air velocity of 4 m/s and a temperature of 2°C

Diameter of snow grain(mm)	Height(mm)	Time to quasi-steady state
0.5	57.3	8501
0.8	35.8	8481
1	28.6	8474
2	14.3	8465

4.11 Comparison of Numerical and Experiment Results

1. Effects of Wind

The initial properties of snow in the experiments are listed in **Table 4-8**. This test lasted for several hours as a result of lower wind speeds. The initial properties obtained by using FEM were integrated into this modeling.

Table 4-8 Initial values for the experiment

Item	Value
Air velocity	1.5m/s
Air temperature	4°C
Density	536kg/m^3
LWC	7.2%
VWC	3.9%
Porosity	0.45
Initial water pressure head (m)	-0.997

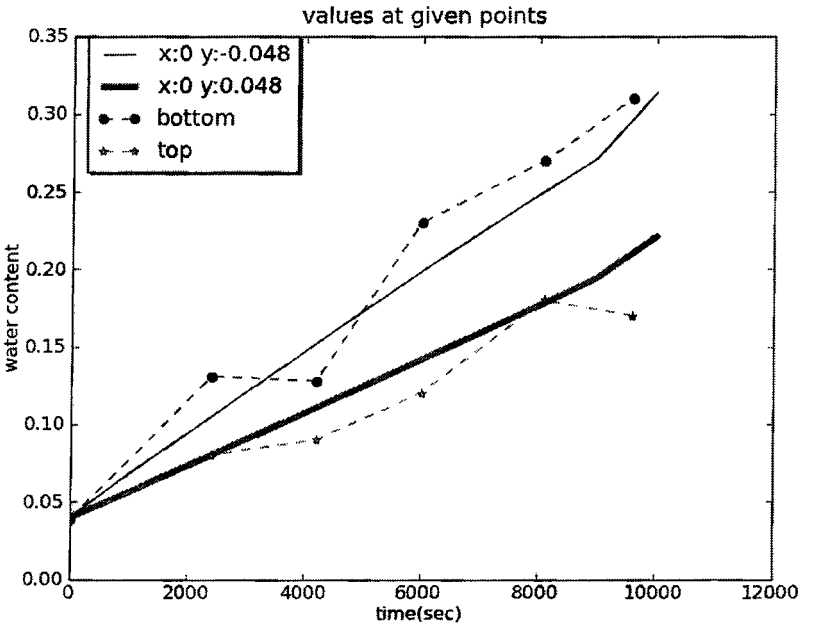

Figure 4-40 Comparison of numerical and experimental results for an air velocity of 1.5 m/s and a temperature of 4°C

The numerical and experimental results are shown in **Figure 4-40**. Satisfactory agreement may be observed between the numerical and the experimental results in the upper portion and in the lower portion of a snow sleeve.

2. Effects of Electric Heating

The initial properties of snow during the test are listed in **Table 4-9**. This experiment took a relatively long time to carry out due to the weak electric current. The same condition was modeled in FEM.

Figure 4-41 shows the numerical and experimental results for the water content and its

time variations. It may be seen that, at an early stage, the values from a numerical simulation and from experiments are in good agreement. The numerical results show obvious divergence from those of the experiments.

Table 4-9 Initial values for the experiment

Item	Value
Density	513kg/m^3
LWC	13%
VWC	6.67%
Porosity	0.50
Initial water pressure head	-0.76

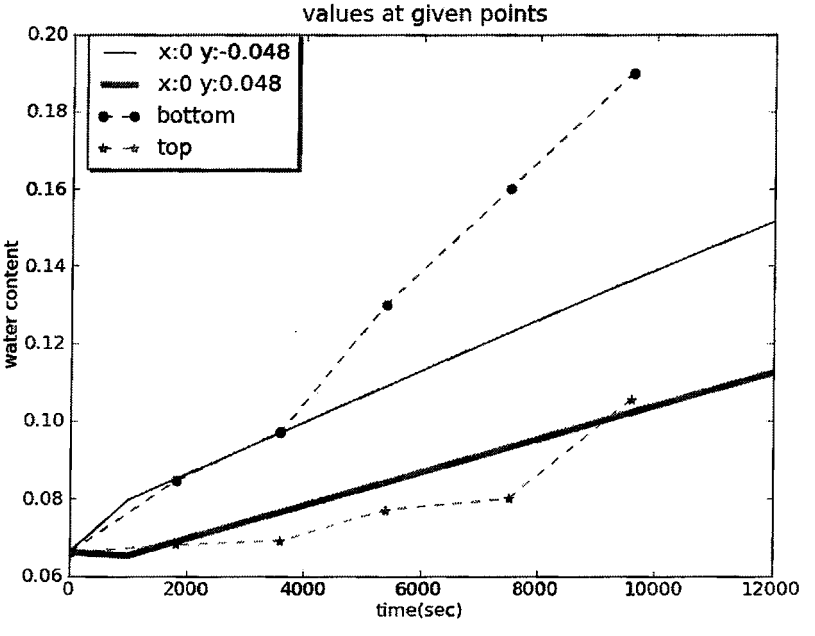

Figure 4-41 Comparison of numerical and experimental results at an electric current of 25A

3. Discussion

Only a tolerable degree of agreement was found to exist between the experimental and the numerical data. The divergence may have come from the degree of accuracy in measuring during the experiments or otherwise from the limitations of the numerical model.

- The data regarding the metamorphism of snow grains was not included in the numerical model. These grains change their shape for several reasons: grain melting, water flow, radiation from within or from the environment, and so forth. It should be mentioned that attempting to model snow grain deformation in simulation has proved to be problematic thus far.
- Numerical modeling was carried out in a two-dimensional space and the water flow along the length direction of a cable was not taken into account. The cable always sagged due to the effects of the gravitational force on the cable-snow sleeve system.
- Factors such as snow surface roughness were excluded in the numerical method, since the numerical results may differ from the experimental results. There is a visibly rough surface on certain snow sleeves. This rough surface may cause uneven snow melting and lead to greater water accumulation at the bottom of a snow sleeve, as shown in **Figure 4-40**. Unfortunately, it is difficult to measure the dynamic variation in roughness during the snow melting process.
- Natural convection was not taken into account in this modeling considering that it might lead to higher experimental data at the bottom of a snow sleeve than those from the modeling as shown in **Figure 4-41**.

4.12 Conclusions

A new numerical model and code designed specifically for simulating the water percolation within a snow sleeve around an overhead line conductor was developed for the purposes of this experiment. The elaborated model takes into account the effects of ambient air convection and Joule heating. Snow properties, such as the snow grain geometry and surface roughness, have an observable effect on melted water percolation.

A set of experiments simulating natural snow shedding conditions was conducted at the CIGELE laboratories. The experimental data was compared with the results from the numerical model and shows satisfactory agreement.

CHAPTER 5

A WET SNOW FAILURE MODEL FOR PREDICTING SNOW-SHEDDING FROM AN OVERHEAD CONDUCTOR

5.1 Introduction

The snow shedding from overhead cables may create potential safety risks, considering that it may cause line cable oscillation and unbalanced loads. Thus, being able to predict-the time of the occurrence of snow shedding, or failure, is a particularly important engineering concern.

Observation of snow shedding from overhead cables is relatively rare and not well-documented. Very few people have actually witnessed the phenomenon and observation of the event has been varied and scattered. It is, therefore, not surprising that sophisticated theoretical models of wet-snow failure have not been fully developed over time.

The modeling discussed in previous sections utilized a fixed mesh to perform an FEM or FVM computation on water percolation within snow. It is recommended that an adapted mesh having moving boundaries, however, should be developed to simulate the processes

of snow-shedding. Furthermore, the dynamic effects resulting from water flow in conjunction with the intrinsic properties of snow present certain difficulties when attempting to model precisely.

The aim of this study is to develop an analytical model based on empirical results in order to predict the occurrence time of wet snow shedding.

5.2 Review of the Literature

A considerable number of dry snow failure models was developed on the basis of avalanche research, even though, certain types of avalanches may be related to wet snow. To date approximately, the existence of a weak snow layer or an imperfection slab has always been assumed to trigger the start of snow failure.

Experimental results also indicate that the mechanical behavior of snow varies with the rate of loading (Schweizer, 1998 and 1999; Navarre *et al.*, 2007; Glen, 1955). Snow displays nonlinear viscous behavior in the low rate range. At high rates, however, the elastic properties tend to dominate and snow failure was observed after extremely limited deformation, namely brittle failure.

Most of the dry snow models were based on the ice failure theory and derived from empirical models. The mechanism of visco-elastic flow, of heat transfer by vapor, and of surface and volume diffusion all lead to a stress distribution balance after a sufficient period of time, thereby making the snow failure process much more complex than that of ice failure. Ballard et al. (1965, 1966) proposed a general dry snow failure model based on the

ice strength and laboratory tests. Despite the large scatter in experimental data, they summarized certain regular principles of the failure strength for medium- and high-density snow.

Water in wet snow has an evident effect on snow shedding, but little work has been carried out in this field. Former models calculated only the variation of the average liquid water content (LWC) in the snow sleeve. Admirat *et al.* (1988) suggested that snow shedding occurred following an increase of the LWC of a snow sleeve, governed by its thermal equilibrium.

Kollár *et al.* (2010) proposed a theoretical model based on heat balance and simulated water migration in the cross-section.

5.3 Experimental Study Carried Out at the CIGELE

A set of experiments was carried out at the CIGELE laboratories and were described in previous chapters.

At the beginning of each test, the snow sleeve was fabricated as a homogeneous circular cylinder around a suspended cable at the center of the sleeve. As the snow which was in contact with the cable surface melted, a hole was formed by the cable moving through the snow sleeve, as shown in **Figure 5-1**.

When the wet snow sleeve is at a higher temperature than the melting point, water migrates towards the bottom of the sleeve with time, and the bottom part of the sleeve

becomes saturated. Experimental observations showed that the LWC at the bottom increased with time, and then remained approximately constant during a relatively longer period during which the water seeped out of the sleeve.

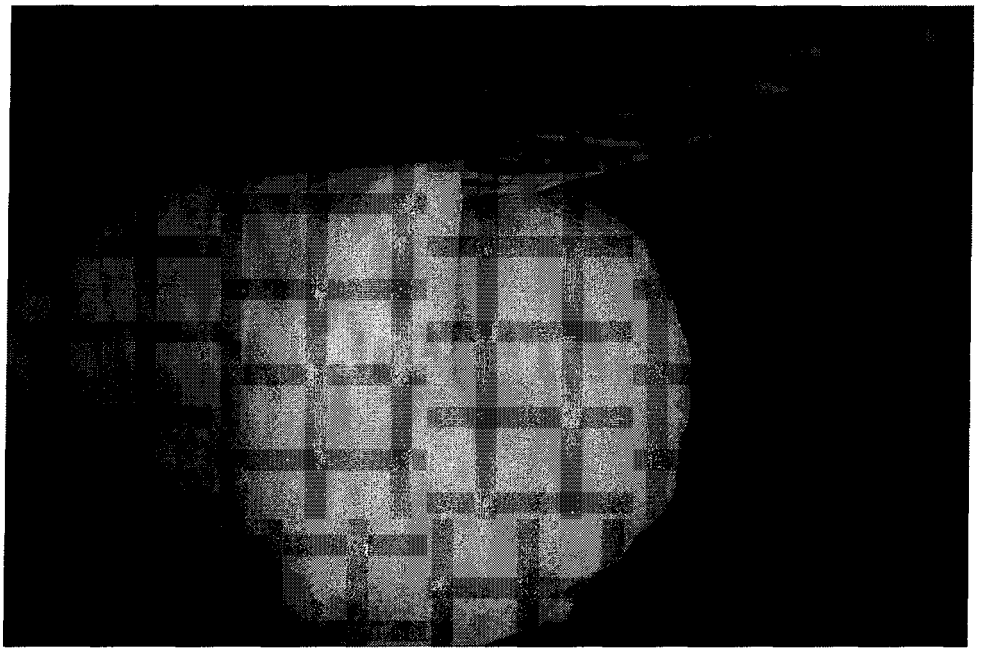

Figure 5-1 A hole during the snow melting period (Photo taken at CIGELE, Jan.27, 2009)

When the temperature of snow reads below the melting point, melted water refreezes rapidly after it is produced. However, a hole with a smooth surface is also formed inside the sleeve by the cable at the same time.

The photos taken at the CIGELE laboratory (**Figure 5-2**) indicate that most of the shedding occurs in the upper section of a snow sleeve. Photos A, B and D in **Figure 5-2** show the wet snow shedding and photo C shows dry snow shedding.

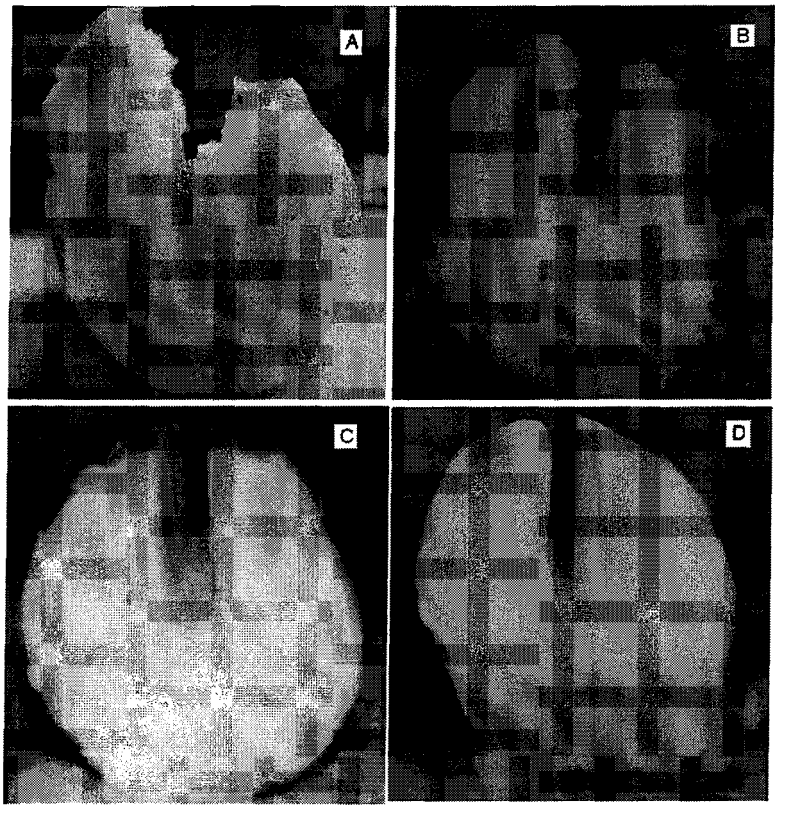

Figure 5-2 Wet snow failure photos taken at the CIGELE laboratories

5.4 Snow-Shedding Mechanism

As shown in **Figure 5-2**, the upper section of the snow sleeve above the cable became detached from the snow sleeve as the shedding occurred. The weakest part of the sleeve leading to snow shedding may thus be shown as area **F** in **Figure 5-3**.

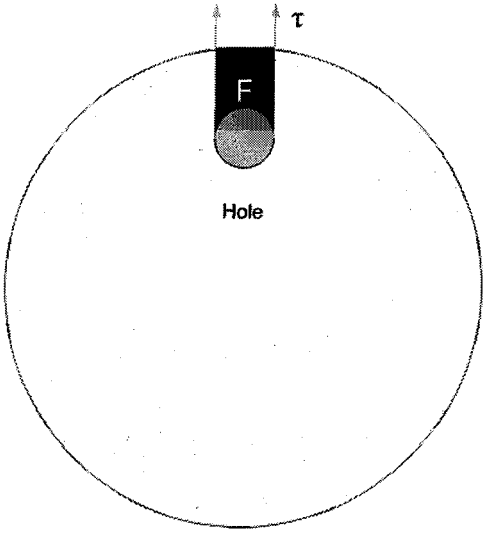

Figure 5-3 Schematic of the weakest area of a snow sleeve

1) Snow Sleeve Variation

Snow-shedding is triggered by a double shear stress, τ, applied to the sleeve section **F**. This shear stress is caused by the gravity force of a snow sleeve combined with the wind pressure. Compared to the volume loss of ice matrix due to the environmental heat flux, however, the deformation caused by the outer force is small enough to be disregarded.

2) Wet Snow Sleeve

The snow which accumulates on overhead cables is not dry snow. One of the prerequisites of snow accretion on overhead cables is the presence of liquid water within the snow, considering that this factor is responsible for the strong adhesion of wet snow to the cable and the cohesiveness of snow grains. A further increase of liquid water content

(LWC), however, results in the weakening of the cohesive and adhesive forces, leading to snow shedding.

Water in wet snow has an obvious effect on snow-shedding, although it is difficult to measure or predict this influence with any degree of precision. Even for dry snow without the effects of water, the irregular and uneven pores within the snow prevent an accurate model from being easily built. Furthermore, snow failure or shedding always starts from a weak part of the snow sleeve. Such weakness may come from the sleeve creation process, but is more likely to be formed by the melted water flow or wind-induced cable vibration. These random factors cannot be simulated and predicted in any accurate way.

The most obvious difference between the dry and wet snow is the initial existing water and the continuous production of melted water. Natural processes such as free or forced convection due to the presence of air temperature above the freezing point, and other artificially controlled conditions such as Joule heating, may cause the solid ice matrix to melt in wet snow and thus increase the LWC. Water percolation through the snow may cause heat transportation within snow and then lead to snow grain melting:

(a) it changes the size and shape of the snow grains;

(b) it changes the size and shape of the bond between neighboring snow grains;

(c) it produces one or more fissures, or imperfections.

Effects (a) and (b) lead to changes in the microstructure and the stiffness of the ice matrix. Effect (c) always results in the development of weakness within the sleeve, helping

to trigger shedding. It is, however, relatively difficult to predict, with any precision, the occurrence of such weakness or the failure in strength of the ice matrix as a result of the uncertainty of the water flow and the irregularity and uneven distribution of pores within the snow itself.

5.5 Assumptions

Since predicting snow shedding is a highly complex activity, a number of assumptions are needed to describe the governing water percolation process. These assumptions include the following:

1) The deformation of the ice matrix on the snow sleeve boundary is disregarded.
2) Snow tended to melt at the surface only at a uniform rate.
3) Though instability of water flow has been observed under a variety of natural conditions, it is still assumed that there is no channel flow or fingering due to the local concentration of water. Thus for any small piece of snow, it is assumed that the snow is homogeneous and isotropic.
4) No heat conduction occurs within the snow.

5.6 Wet Snow Failure Model

Most of the previous models calculated only the variation of the average LWC in the snow sleeve. They assumed snow shedding occurred following an increase of the LWC in the sleeve. The exact LWC at which shedding occurs is difficult to predict: it depends on the snow density and external factors, as for example, a sudden vertical jump which may

trigger shedding at a lower LWC. The range of LWC values reported at the time of shedding varies between 20% and 40% by mass (Admirat and Sakamoto 1988). As discussed in previous chapters, the residual water distribution is not homogeneous and depends on many factors such as snow microstructure and melted water production rate. This method may thus be seen to provide a crude way of predicting the occurrence of snow shedding.

Kollár *et al.* (2010) proposed a theoretical model based on experiments, which assumed that shedding occurred while the entire end section turned below the centerline.

A number of research projects were carried out on the topic of ice or dry snow failure. It is reasonable to assume that some correlation exists between dry and wet snow. As a result, an analytical model based on dry snow failure and experimental data is being developed at present.

1. Dry Snow Failure

Ballard *et al.* (1965) proposed a correlation between the failure strength, σ_f, and the ultimate strength of ice matrix within snow, σ_i,

$$\sigma_f = \sigma_i(1 - \phi_e) \qquad \textbf{Equation 5-1}$$

where ϕ_e is the effective porosity and its value is generally higher than the bulk porosity.

In **Figure 5-2** and **Figure 5-3**, it can be seen that snow shedding occurs due to the double shear stress along the vertical direction. The empirical equation for the double shear, τ_f (Pa), in Ballard's model is

$$\tau_f = 38.8\left(\frac{\rho_s}{\rho_i} - 0.444\right) \times 10^5 = 2.16 \times 10^5 \times \left(1 - \frac{\phi_{ds}}{0.556}\right) \times 10^5 (\text{Pa}) \quad \textbf{Equation 5-2}$$

where ϕ_{ds} is the porosity of dry snow, and ρ_s and ρ_i are the density of snow and ice, respectively. The maximum of snow density is around 730 kg/m^3 in Ballard's study.

The correlation between the failure strength, σ_f, and the snow density is plotted in **Figure 5-4**, from which it may be observed that the snow failure strength increases as the snow density increases.

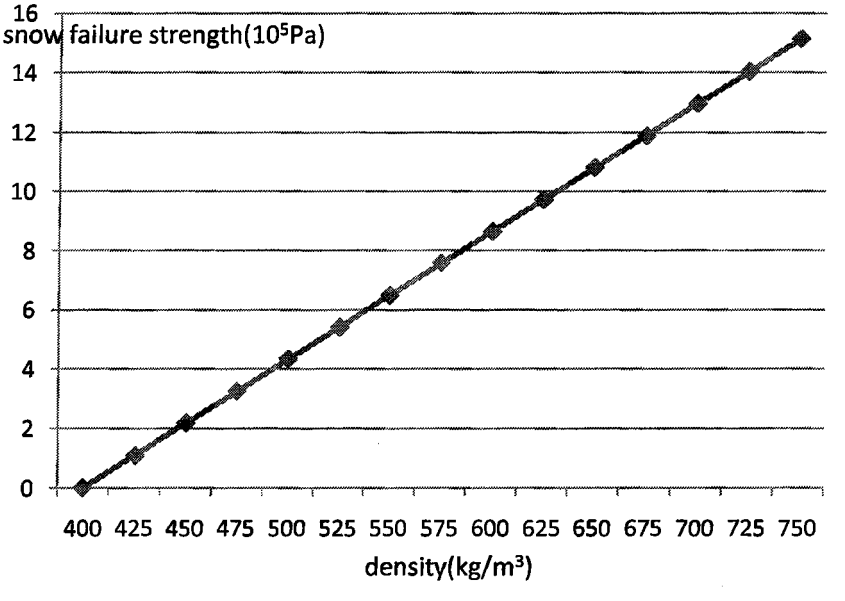

Figure 5-4 Correlation between the failure strength and the snow density

It is clear that the failure strength occurs as snow porosity approaches the critical value ϕ_{sc} 0.556. The time required for the occurrence of snow shedding, t_s, can thus be expressed by the following equation

$$t_s = \frac{\phi_{sc} - \phi_{\text{ini}}}{V_v} \qquad \textbf{Equation 5-3}$$

where ϕ_{ini} is the snow porosity at the initial state and V_v is the volume variation rate.

2. Wet Snow Failure

It is not surprising that the results obtained from **Equation 5-3** show much divergence from the data observed relating to wet snow shedding considering that this equation is only valid for dry snow. In order to be applicable to wet snow, **Equation 5-3** must be modified and extended.

For this purpose, parameter ϕ_{es}, is introduced to describe the effect of the water flow. Thus the time of the occurrence of wet snow shedding is given by

$$t_s = \frac{\phi_{\text{sc}} - \phi_{\text{es}}}{V_v} \qquad \textbf{Equation 5-4}$$

The effective initial porosity, ϕ_{es}, of wet snow can be obtained as a result of multiplying initial porosity, ϕ_{ini}, by the function f_{vp}.

$$\phi_{es} = f_{vp}\phi_{\text{ini}} = f(\text{Q}, \text{G})\phi_{\text{ini}} \qquad \textbf{Equation 5-5}$$

The function f_{vp} represents the effect of the water flow and its value depends on geometry G of the wet snow sleeve as well as the outer heat flux condition Q.

Only one kind of snow sleeve was studied here: the diameter of the snow sleeve and cable was 0.1m and 0.0127m, respectively.

Two types of water flow were considered in this study: the initial residual water flow and the melted water flow. As discussed in a previous chapter, the initial residual water flow was completed in a very short time, but the melted flow is likely to continue for a long period of time before snow shedding occurs. As shown in **Figure 4-22**, the initial residual water maintains a water content gradient due to the effects of capillarity. The quantity of the initial water has a major influence in triggering the melted water flow. These two types of water flow may thus be seen as two interrelated processes.

The function f_{vp} is assumed as below

$$f_{vp} = a + be^{cW_{ini}+dQ_l} \qquad \textbf{Equation 5-6}$$

where a, b, c, and d are constants, w_{ini} is the initial volume water content (IVWC) and Q_l is the heat flux at the snow surface per unit length of cable (w/m).

5.7 Snow Melting Rate

5.7.1 Heat Flux

The ambient air or Joule heating (**Figure 5-5**) may be considered the heat sources for triggering the snow-melting process. The heat flux Q (w) is defined as

$$Q = Q_a + Q_j + Q_c \qquad \textbf{Equation 5-7}$$

where Q_a is the forced or natural heat convection from the ambient air, and Q_j is the Joule heat from an electric conductor; Q_c is the heat exchange by condensation or evaporation on the sleeve-atmosphere interface, which was neglected in this study.

1. Forced Air Convection

Heat transfer coefficient was computed in CHAPTER 2. A sample result is shown in **Figure 2-8** and **Figure 2-9**. It should be noted that the numerical results are approximately 15% lower than those determined by the empirical equations; the major cause of this is that these simulations were carried out under a constant surface temperature condition, whereas most of the empirical equations work better for a constant heat flux at the surface. It is reasonable to assume that the surface keeps at 0°C due to liquid water within wet snow.

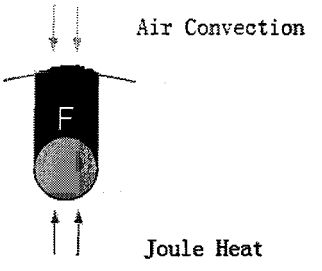

Figure 5-5 Heat transfer at the snow and cable surfaces

2. Joule Heat

Joule heat, Q_j, was produced in a carrying-current conductor, and it can be determined by **Equation 3-27**. Sample data is shown in the following table.

Table 5-1 Heat flux at the conductor surface at 0°C (ACSR diameter 12.7 mm)

Current (A)	Heat flux on cable surface (W/m)
25	0.2
50	0.8
100	3.2

3. Natural Air Convection

The natural convection heat flux, Q_{an}, may be calculated by

$$Q_{an} = h_a(T_a - T_s) \qquad \textbf{Equation 5-8}$$

where T_s and T_∞ are the temperatures at the snow surface and of the air, respectively. The average natural convection coefficient h_a and Nu may be obtained by following equations

$$h_a = \frac{NuK}{D}$$

$$Nu = \left\{0.60 + \frac{0.387Ra^{1/6}}{[1+(0.559/Pr)^{9/16}]^{8/27}}\right\}^2$$

Sample data is shown in Table 5-2.

Table 5-2 Heat flux at the snow sleeve surface (diameter 0.1 m)

Air Temperature (°C)	Heat flux on snow surface (W/m)
1	0.63
2	1.51
3	2.53

4	3.65
5	4.85

5.7.2 Volume Variation Rate

The volume loss rate of ice grains, V_q (m^3/s), can be obtained by

$$V_q = \frac{m_q}{\rho_s} = \frac{Q}{H_f \rho_s} \qquad \textbf{Equation 5-9}$$

where H_f is the fusion heat of water (334×10^3J/kg).

The average volume variation rate, V_v (1/m s), is

$$V_v = \frac{V_q}{\pi(r_s^2 - r_c^2)} \qquad \textbf{Equation 5-10}$$

where r_s and r_c are the diameters of the snow sleeve and the cable, respectively.

5.8 Data Fitting

The data-fitting was carried out based on Equation 5-6 and the results of experiments conducted at the CIGELE laboratories.

Where the melted water percolation is concerned, the outer conditions were subdivided into two types: Joule heating with natural air convection, and forced air convection. Under the former conditions, melted water concentrates in the lower section of the snow sleeve, remembering that water flow is almost symmetrical. Under latter the conditions, melted water percolates throughout all the areas within the snow sleeve; it should be noted that the

rate of snow melting is not consistent as a result of the variations in the local heat transfer coefficient along the snow sleeve surface, as shown in **Figure 2-8.**

1. Electric Heating with Natural Air Convection

- Water Flows

Melted water flows as a result of the concentration of Joule heating near the upper surface of the line conductor, as shown in **Figure 5-6**. Natural air convection occurs all around the snow sleeve surface and is preponderant in the heat flux if the temperature of the ambient air is high enough.

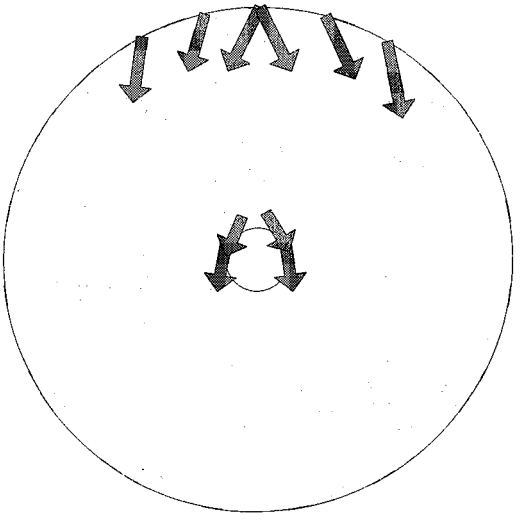

Figure 5-6 Schematic of water flow under electric heating

- Data Fitting

The following equation is obtained by data fitting based on the experimental

$$f_{vp} = 3.74 - 3.15e^{-0.5W_{ini}-0.03Q_l} \qquad \textbf{Equation 5-11}$$

The relationship between f_{vp}, W_{ini} and Q_l is shown in **Figure 5-7**. It can be seen that f_{vp} increases with W_{ini} or Q_a. Furthermore, f_{vp} is less than 1 when W_{ini} or Q_l is small enough. For example, f_{vp} is approximately 0.89 and W_{ini} and Q_l are 0.3 and 3 w/m. The time required to attain wet snow shedding is longer than it is for dry snow when f_{vp} is less than 1. This result is in agreement with the hypothesis that a small quantity water consolidates the cohesive force of wet snow but that a further increase of liquid water weakens the cohesive and adhesive forces consequently leading to snow shedding.

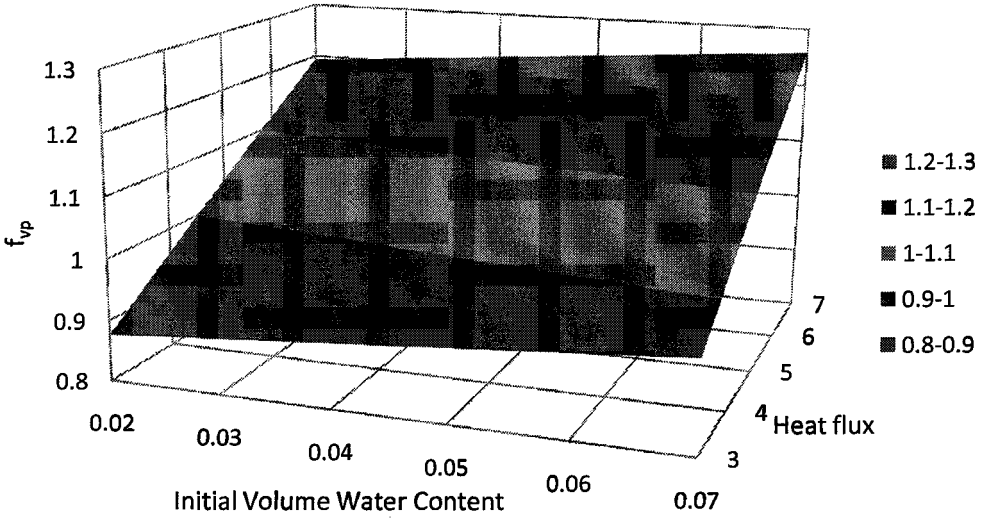

Figure 5-7 The relationship between f_{vp}, IVWC, and the heat flux

Figure 5-8 shows that the function f_{vp} increases in a nonlinear fashion with the initial volume water content (IVWC) at a given heat flux and that, therefore, the time required to wet snow shedding, T_s, increases nonlinearly with respect to the IVWC.

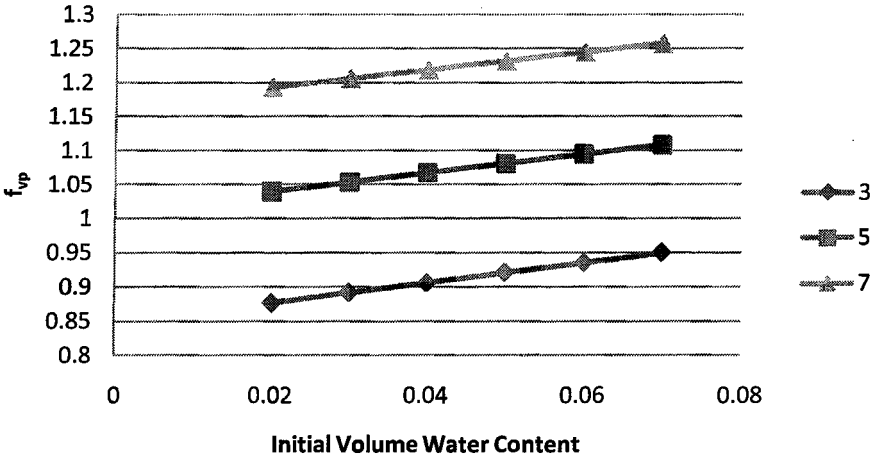

Figure 5-8 f_{vp} increases with increasing IVWC at a given heat flux

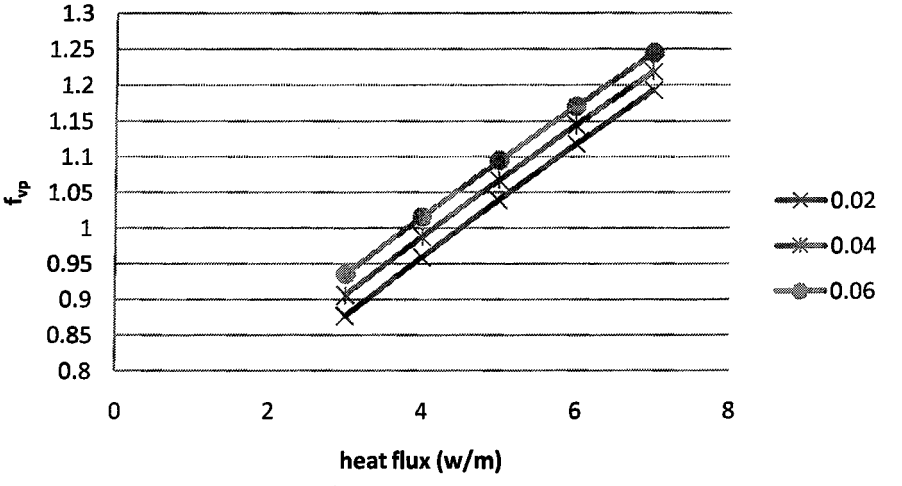

Figure 5-9 f_{vp} increases with increasing heat flux at a given IVWC

Similarly, at a given IVWC, the function f_{vp} increases in a nonlinear manner with the heat flux, as shown in **Figure 5-9** and, therefore, the time required to wet snow shedding, T_s, increases nonlinearly as the heat flux increases.

2. Forced Air Convection

- Water Flow

Melted water is produced by forced air convection and the water flow concentrates near the top surface of a snow sleeve, as shown in **Figure 5-10**. It should be noted that the water flow is uneven due to the uneven distribution of the heat convection.

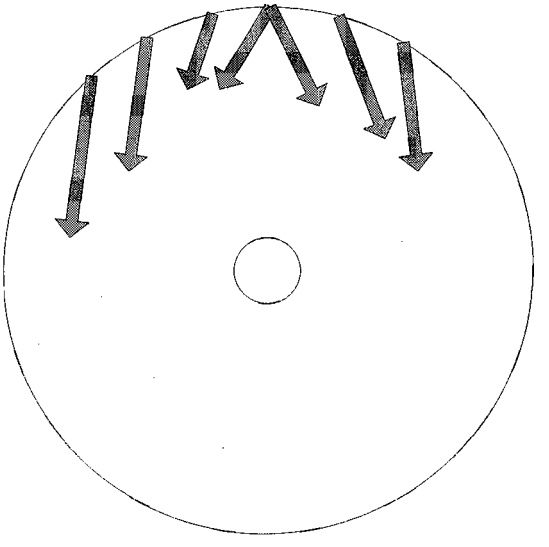

Figure 5-10 Schematic of the water flow under forced convection

- Data Fitting

The following equation is obtained by data-fitting based on the experimental results.

$$f_{vp} = 1.19 - 0.263e^{-1.14W_{ini}-0.0656Q_l} \qquad \textbf{Equation 5-12}$$

It can be seen in **Figure 5-11** that f_{vp} increases when W_{ini} or Q_l is increased. Compared to the prior equation under Joule heating, f_{vp} is always larger than 1. Therefore, the time

required to wet snow shedding is shorter than that of dry snow shedding. Considering that the values of the heat flux resulting from forced convection are much higher than those of the previous type, the effects from a forced convection become dominant in determining the effective initial snow porosity.

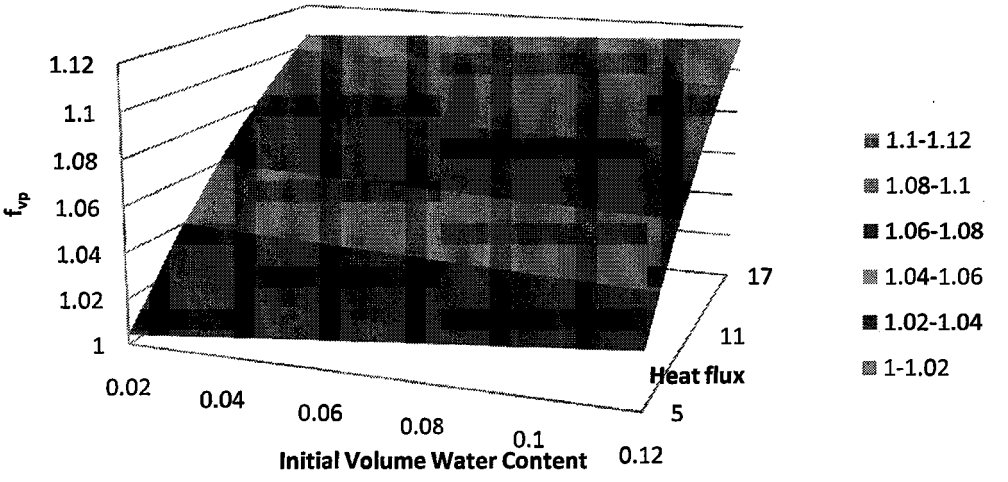

Figure 5-11 The relationship between f_{vp} and IVWC, forced air convection

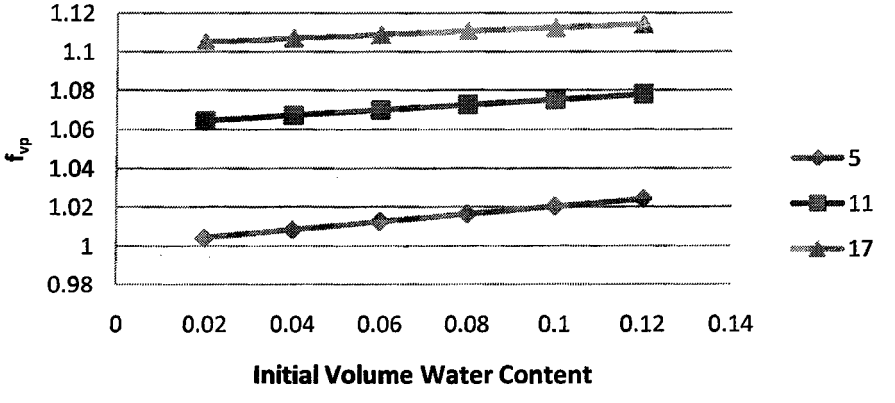

Figure 5-12 f_{vp} increases with increasing IVWC at a given heat flux

In **Figure 5-12** and **Figure 5-13** it can be seen that the function f_{vp} increases nonlinearly with the initial volume water content (IVWC) or heat flux and, therefore, the time required to wet snow shedding, T_s, increases nonlinearly with respect to the IVWC or heat flux.

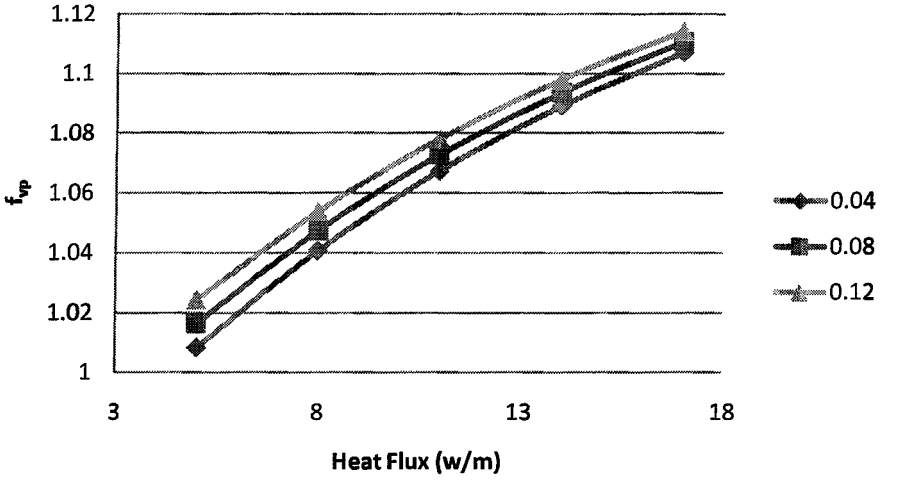

Figure 5-13 f_{vp} increases with increasing heat flux at a given IVWC

5.9 Conclusions

The water flow inside a snow sleeve influences its shedding process in a number of ways, such as changing the shape and size of the snow grains. Generally, snow shedding starts at a weakness, or imperfection, caused by the water flow. These random factors, however, cannot be predicted in any accurate way.

Under certain assumptions, an analytical model was developed to predict the occurrence of the snow shedding. This model is based on a modified empirical dry snow model in conjunction with experiments carried out at the CIGELE laboratories. This model provides

a rapid estimation of the required Joule heat or wind speed to trigger snow shedding on an overhead conductor.

CHAPTER 6

CONCLUSIONS AND RECOMMENDATIONS

6.1 Conclusions

1. Forced Convection around a Snow Sleeve

A numerical study of forced convection around a snow sleeve in a cross flow of air was conducted by using the computational fluid dynamic (CFD) code known as FLUENT. This investigation was carried out on the effects of the special characteristics of a snow sleeve, including surface roughness and its non-circular shape, on the local HTC distribution and on the overall HTC under different wind conditions.

(a) For a smooth circular snow sleeve, all cases indicate the correct characteristic shape of the local Nusselt number (***Nu***) and show agreement with previous research. In the subcritical range ($Re<10^5$), a local maximum of the ***Nu*** is located at, or close to, the stagnation point, where the ***Nu*** decreases as a result of the laminar boundary layer development. A minimum ***Nu*** attained a point close to the top of the cylinder at $\theta \approx 80°$, which is associated with separation. Moving further into the wake region, ***Nu*** increases with θ as a result of mixing associated with the vortex formation.

(b) For a smooth circular snow sleeve, the overall average Nusselt numbers obtained from numerical simulations are approximately 15% less than those obtained from the empirical equations. The major cause of this is that where these simulations are carried out under constant surface temperature conditions, most of the experiments are conducted within the constant heat flux from the surface.

(c) For an elliptical snow sleeve, the ***Nu*** distribution reveals a curved shape approaching that of a circular shape except that the ***Nu*** value near the front stagnation point decreases with an increase in the -eccentricity of the ellipse, *i.e.* there is an increase in deformation.

(d) From the results obtained on the elliptically shaped cylinder, the effects from sleeve deformation may be disregarded if the eccentricity of the ellipse is < 0.6. Snow shedding from overhead cables will occur when the eccentricity reaches a critical value, which is usually non-significant in real climatic situations. In most cases, therefore, the effects of the sleeve shape on snow shedding will be negligible.

(e) This investigation demonstrates that roughness has a significant effect on the heat transfer rate.

At a given Reynolds number, it may be seen that:

- The higher the roughness value, the closer the laminar-turbulent transition point approaches the front stagnation point.
- The peak value of ***Nu*** increases as the roughness parameter increases.
- The heat-transfer within the wake region increases with increasing roughness.

Unfortunately, it is difficult to measure the variation in roughness during the snow melting process. The sleeve will not melt at a uniform rate as a result of snow inhomogeneity and uneven heat flux due to outer wind. Also, it was found that the roughness increases more rapidly on the upper part than on the lower part of the snow sleeve.

(f) The numerical results, upon taking the roughness effects into account, are in good agreement with the theoretical analyses and experimental data from the literature in the field.

2. Water Percolation within a Snow Sleeve

A new numerical model and code designed specifically for simulating water percolation within a snow sleeve around an overhead line conductor was successfully developed here. The rate at which water melted was subjected to prior thermal research.

(a) This study is considered to be pioneer research in that a complete numerical model was developed and corroborated by laboratory experiments for melted water percolation within a snow sleeve around an overhead line conductor. The elaborated model takes into account the effects of ambient air and Joule heating heat fluxes.

(b) Under windy conditions, the value of melted water varied along the snow surfaces because of the uneven distribution of the heat flux. It may be observed that the melted water flow attains its maximum near the front stagnation point.

The water flow decreases with time and the overall water percolation reaches a quasi-steady state eventually, while the lower part of the snow becomes saturated

and surplus water seeps out of the sleeve.

(c) This study reveals the effects of air velocity.

- At the same temperature, the time required to attain the quasi-steady state decreases as the air velocity increases.
- At higher temperatures, the effects of the air velocity on water percolation become more obvious. The time needed to reach the quasi-steady state decreases to 48% and 66% of its initial value when the air velocity increases from 2m/s to 8m/s at 1°C and 4°C, respectively.
- At lower air velocities, the effects of air velocity become more evident.

(d) This study reveals the effects of air temperature.

- At the same air velocity, the time required to attain the quasi-steady state decreases as the temperature increases.
- At a higher air velocity, the effects of air temperature become more obvious. The time decreases to 73% and 83% of its initial value when the air temperature increases from 1°C to 4°C at air velocity 2 m/s and 4 m/s, respectively.
- At a lower air temperature, the effects of air velocity become more evident.

(e) Joule heat has been approved as an effective and valid way of disposing of accumulated snow from overhead conductors; it is widely used in several countries. The proposed model provides a complete simulation, and can thus be used to estimate water percolation and snow shedding.

Joule heat is more effective when the electric current is higher than 50A. One should be aware, however, that strong electric currents may cause serious damage to line conductors including cable breakdown due to overheating.

(f) Snow properties, such as the snow grain geometry, have an effect on melted water percolation. Only the snow grain size, however, was taken into account in the numerical model. The numerical results show that the time required to attain the quasi-steady state increases as the snow grain diameter decreases, although in the majority of cases the effects of the snow grain may be disregarded.

(g) Water percolation increases with an increase in the snow surface roughness. The time required to reach the quasi-steady state is only 1/4 or 1/5 of that required by a smooth surface when the surface roughness exceeds a critical value. This critical value depends on the surface roughness, the air velocity and the geometry of the snow sleeve.

3. Equivalent Thermal Conductivity of Dry Snow

The equivalent thermal conductivity of dry snow was analyzed and its value was estimated by means of a microstructure model. Besides snow density, the strong influences of microstructure and vapor on thermal conductivity were taken into account in this model.

(a) A microstructure model was developed to estimate the equivalent thermal conductivity of dry snow. The equivalent thermal conductivity is a function of the snow temperature and the shape factors, ra_1 and ra_2.

(b) The equivalent thermal conductivity of dry snow increases with increasing density

due to the fact that the conductivity of pure ice is at least 100 times greater than that of saturated moist air.

(c) The snow was classified into four types by grain shape: spherical, cylindrical, hexagonal, and cubical. Considering that snow has the same density values, cubical grains have the largest values of equivalent thermal conductivity.

(d) The results of this model show concord with previous investigations.

(e) The equivalent thermal conductivity of dry snow increases with increasing temperatures, especially temperatures which rise above -5°C. The nonlinear increase in conductivity with snow temperatures above -5°C may be ascribed to the fact that saturated water vapor is more conductive at higher temperatures and that the dependency of the saturated vapor pressure on the temperature is exponential.

About 20% of the heat is moved by vapor when the temperature is near 0°C. When the temperature of snow is very low, around -50°C, the difference in thermal conduction between the dry air and the wet air is only approximately 1%, which means that the effect of vapor can be disregarded when the temperature is below -50°C.

(f) The relationship between the snow conductivity model and the weather was established and may be used to estimate the equivalent conductivity through weather conditions.

(g) A set of experiments was conducted at the CIGELE laboratories. The large scatter observed in the experimental data is due to the strong influence of the microstructure on the thermal conductivity and the snow sleeve as reproduced in the laboratory

consisting of multiple types of snow grain.

4. Prediction of Wet Snow Shedding

The water flow inside a snow sleeve influences the snow shedding in a number of ways, such as changing the shape and size of the snow grains. Generally, snow shedding starts at a weak part, or imperfection, caused by the water flow although it cannot be simulated and predicted in any accurate way.

Under certain assumptions, an analytical model was developed for predicting the time of the snow shedding occurrence. This model is based on a modified empirical dry snow model as well as on relevant experiments carried out at the CIGELE laboratories. The main results are the following ones:

(a) A parameter, namely the effective initial porosity, was introduced to describe the effects resulting from the water flow within a wet snow sleeve. Its value depends on the properties of wet snow such as the geometry and size of the snow grains.

(b) Concerning the melted water percolation, the outer conditions were subdivided into two types: forced air convection and Joule heating with natural air convection.

(c) The parameter values were calculated from experiments conducted at the CIGELE laboratories.

(d) The effective initial porosity increase with increasing air velocity and electric current intensity, so that the time of snow shedding occurrence decreases in a nonlinear way with increasing air velocity and the intensity of the electric current.

(e) At given initial snow porosity and heat flux values, the effective initial porosity

increases nonlinearly with the initial volume water content (IVWC) and, therefore, the time required to wet snow shedding, T_s, decreases nonlinearly with respect to the IVWC.

(f) At a given initial snow porosity and IVWC, the effective initial porosity increases nonlinearly with the heat flux and, thus, the time for wet snow shedding, T_s, decreases nonlinearly as the heat flux increases.

(g) Upon comparing dry snow failure, the existing water tends to delay the occurrence of snow shedding at lower melting rates due to the water-strengthened adhesion force between neighboring grains. A further increase in the melting rate produces more water then weakens the cohesive and adhesive forces, while accelerating the occurrence of snow shedding.

6.2 Recommendations for Future Research Directions

It is to be recommended that further work may confidently be carried out on the following subjects.

1. Comparative study of different type of line conductor and snow sleeve

More experiments should be carried out for different type of line conductor and snow sleeve. The comparative study could reveal these effects and help to develop a model with widely suitability and accuracy.

2. A full heat transfer model for the snow sleeve

The heat transfer at the surface of snow sleeve is neither a constant temperature nor a constant heat flux if the effects of the Joule heat are taken into account in the numerical model. As sample results from numerical simulation by FLUENT shown in **Figure 6-1**, surface temperature may not remain constant at the surface of the snow sleeve. Thus, in **Figure 6-2** it will be observed that the heat flux near the front stagnation point is less than it is for the cylinder with a constant surface temperature as a result of heat conduction and the temperature gradient within the snow sleeve.

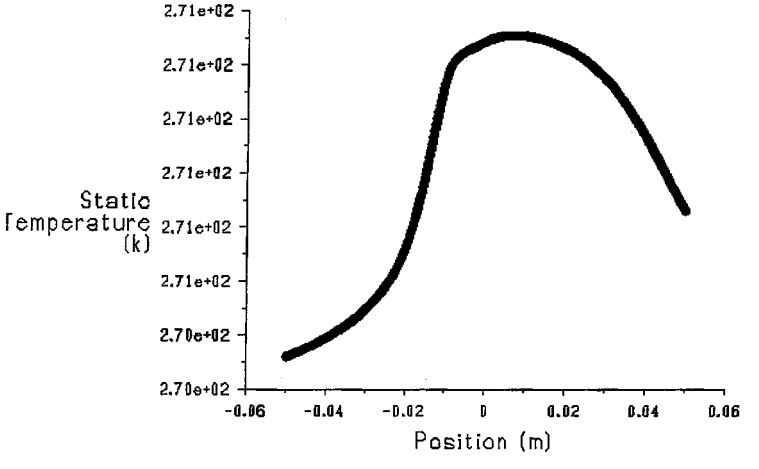

Figure 6-1 Temperature distribution along the surface of the sleeve

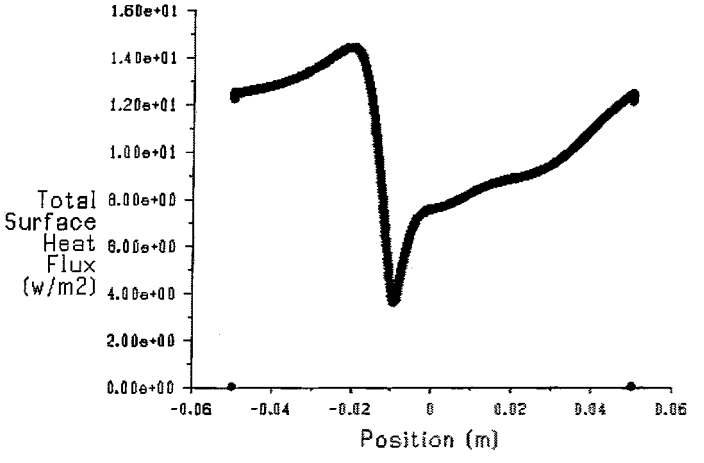

Figure 6-2 Heat flux around the surface of the sleeve

3. Water percolation within a Snow Sleeve

(a) To extend this numerical model with other concurrent physical processes.

- Heat transfer within the snow. Heat transportation in wet snow is more complex than it is in dry snow. The effective heat transfer includes heat conduction through the ice matrix and air, internal radiation as well as dynamic heat transportation as a result of the movement of vapor and water.
- Snow metamorphism. The bulk density and hydraulic conductivity were already considered in this model. The melted-water percolation or heat transfer alter such regional snow properties as the shape and size of the snow grain and ice matrix, and then lead to the variation in the hydraulic conductivity.

(b) To extend the two-dimensional model proposed here into a three-dimensional snow model. A study on a new three-dimensional model should be assigned priority among all other necessary updating projects, since it may serve to overcome the

main drawbacks of a two-dimensional model because water always flows to the sagging portion of the cable.

4. Prediction of snow shedding

The occurrence time of snow shedding depends on several factors including geometry $\boldsymbol{G}$ of snow sleeve, outer heat flux $\boldsymbol{Q}$ and snow intrinsic properties $\boldsymbol{P_s}$.

$$t = f(G, Q, P_s) \qquad \textbf{Equation 6-1}$$

Only one kind of snow sleeve was investigated in this study. More research could be carried out on snow sleeve with different size and shape. The geometry of snow grain also has effect on the snow shedding as it influences the heat transportation and water percolation within snow. The outer heat flux includes Joule heating and air convection. The air convection depends on air velocity and air temperature.

BIBLIOGRAPHICAL REFERENCES

1. Achenbach, E., "Total and local heat transfer from a smooth circular cylinder in cross-flow at high Reynolds number", Int. J. Heat Mass Transfer, Vol.18, pp.1387-1396, 1975.
2. Achenbach, E., "the effect of surface roughness on the heat transfer from a circular cylinder in cross-flow at high Reynolds number", Int. J. Heat Mass Transfer, Vol.20, pp.359-369, 1977.
3. Adams, E. E. and Sato A., "Model for Effective Thermal Conductivity of a Dry Snow Cover Composed of Uniform Ice Spheres", Annals of Glaciology, Vol.18, pp.300-304, 1993.
4. Admirat, P., "Wet Snow Accretion on Overhead Lines" In "Atmospheric Icing of Power Networks" by M. Farzaneh, 2008.
5. Ambach, W., Blumthaler, M., Kirchlechner, P., "Application of the Gravity Flow Theory to the Percolation of Melt Water through Firn", Journal of Glaciology, Vol.27, No 95, pp. 67-75, 1981.
6. Andrews, T., "Observations on Pure Ice and Snow", Proc. R. Soc. Lond., Vol.40, pp.544-549, January 1, 1886.
7. Armstrong, R. L. & Ives, J. D., Editors, "Avalanche Release and Snow Characteristics", Institute of Arctic and Alpine Research, University of Colorado, 1976.
8. Armstrong, R. L., Brun, E., "Snow and Climate: Physical Processes, Surface Energy Exchange and Modeling", Published by Cambridge University Press, 2008.
9. Assouline, S. and Tartakovsky, D. M., "Unsaturated hydraulic conductivity function based on a soil fragmentation process", Water resources research, Vol.37, No.5, pp.1309-1312, May 2001.
10. Baevay M., Baevz, P. and Kaplanx, A., "An analysis of the heat transfer from a moving elliptical cylinder", J. Phys. D: Appl. Phys., Vol.30, pp.1190–1196, 1997.
11. Ballard, G. E. H. and Mcgaw, R. W., "A theory of snow failure", U.S. Army Cold

Regions Research and Engineering Laboratory, Research report, Vol.137, 1965.

12. Ballard, G. E. H. and Feldt, E. D., "A theoretical consideration of the strength of snow", J. Glaciology, Vol.6, pp.159-170, 1966.
13. Barlow, J., "Mathematical Modelling of Snow", http://www.enm.bris.ac.uk/teaching/projects/2002_03/jb8355/index.html, 2002.
14. Bengtsson, L., "Percolation of meltwater through a snowpack", Cold regions science and technology, Vol.6, pp.73-81, 1982.
15. Bonelli, P., Lacacalla, M., "Trends in snow deposition on overhead electric lines: Using synoptic data to investigate the relationship black-out risk/climate change", Troccoli (ed.), Management of Weather and Climate Risk in the Energy Industry, pp 3-12, 2009.
16. Brooks, R. H. and Corey, A. T., "Hydraulic properties of porous media", Hydrol. Pap. 3, Colo. State Univ., Fort Collins, 1964.
17. Brun, E., Pahaut, E., "An efficient Method for a delayed and accurate characterization of snow grains from Natural snowpacks", Journal of Glaciology, Vol.37, No. 127, 1991.
18. Bryruk, E., "Heat Transfer and Flow Structures Around Circular Cylinders in Cross-Flow", Int. J. of Engineering and Environmental Science, Vol. 23, pp.299-315, 1999.
19. Cengel, Y. , "Heat and mass transfer", 3th edition, McGraw Hill, 2007.
20. Colbeck, S. C., "One-dimensional water flow through snow", U. S. Army, CRREL, pp319-327, 1971.
21. Colbeck, S. C., "A theory of water percolation in snow". Journal of Glaciology, Vol.11 (63), pp.369–385, 1972.
22. Colbeck, S. C., and Davidson, G., "Water flow through homogeneous snow, In The Role of Snow and Ice in Hydrology", (Proceedings of the Banff Symposium, September, 1972), Vol.1, pp. 242-257, 1973.
23. Colbeck, S. C., "Water Flow Through Snow Overlying an Impermeable Boundary", Water Resour. Res., Vol.10 (1), 119–123, 1974.
24. Colbeck, S. C., "The Physical Aspects of Water Flow through Snow", Adv. Hydrosci., Vol.11, pp.165-206, 1978.
25. Colbeck, S. C., Ackley, S. F., "Mechanisms for ice bonding in wet snow accretions on

power lines", Proceedings of the 1st International Workshop on Atmospheric Icing – IWAIS 1982, pp. 25-30, 1982.

26. De Quervain, M.R., "On Metamorphism and Hardening of Snow under Constant Pressure and Temperature Gradient", IUGG General Assembly of Toronto, IASH Publication No. 46, pp 225-239, 1958.
27. De Quervain, M.R., "Snow Structure, Heat and Mass Flux Through Snow" (Theme paper), International Symposia on the Role of Snow and Ice in Hydrology, Symposium on Properties and Processes, Banff, 1972.
28. Dozier, J., Davis., R. E. and Perla, R., "On the Objective analysis of snow microstructure", Avalanche Formation, Movement and Effects (Proceedings of the Davos Symposium, September 1986). IAHS Publ. no. 162, 1987.
29. Durbin. P., "A Reynolds-stress model for near-wall turbulence", J. Fluid Mech. Vol.249, pp. 465-498, 1993.
30. Durbin P. A., On the k-e Stagnation Point Anomaly, Int. J. of Heat and Fluid Flow, Vol.17, pp.89-90, 1996.
31. Fluend Inc., "Flow Over a Cylinder", April 16, 2007.
32. Glen, J. W., "The creep of polycrystalline ice", proc. Roy. Soc. A228, pp.519-528, 1955.
33. Gottradi, G., Venutelli, M., Richards: "Computer program for the numerical simulation of one-dimensional infiltration into unsaturated soil", Computer & Geosciences, Vol. 9, pp.1239-1266, 1993.
34. Gottradi, G., Venutelli, M., "UPF: two-dimensional finite-element ground water flow model for saturated-unsaturated soils", Computer & Geosciences, Vol. 27, pp.179-189, 2001.
35. Gravner, J. and Griffeath, D., "Modeling snow crystal growth: a three-dimensional mesoscopic approach", 2008.
36. Gray, J. M. N. T., "Water Movement in Wet Snow", Philosophical Transactions: Mathematical, Physical and Engineering Sciences, Vol.354, No. 1707, pp.465-500, Mar. 15, 1996
37. Hamdami, N., Monteau, J.-Y. and Le Bail, A., "Effective thermal conductivity of a high

porosity model food at above and sub-freezing temperatures", International Journal of Refrigeration Vol.26, pp. 809-816, 2003.

38. Harris, D. K., Goldschmidt, V. W. "Measurements of the overall heat transfer from combustion gases confined within elliptical tube heat exchangers", Experimental Thermal and Fluid Science, Vol.26, pp.33–37, 2002.
39. Illangasekare, T. H., Walter, R. J., Meter, JR. M. F. and Pfeffer, W. T., "Modeling of meltwater infiltration in subfreezing snow", water resources research, Vol.26, pp.1001-1012, May 1990.
40. Incropera, Frank P. and DeWitt, David P., "Introduction to Heat Transfer", fourth edition, 2002.
41. Incropera, Frank P., "Fundamentals of heat and mass transfer", 6th ed., Hoboken, N.J. J. Wiley, 2007.
42. James, A. Liggett, Philip, L. F. Liu, "The boundary integral equation method for porous media flow", pp.1-3, 1983.
43. Kingery, W. D. "Regelation, surface diffusion and ice sintering", J. appl. Phys., Vol.31, pp.833-838, 1960.
44. Kollár, L. E., Olqma, O. and Farzaneh, M., "Natural wet-snow shedding from overhead cables", Cold Regions Science and Technology, Vol.60, pp.40–50, 2010.
45. Kumar, C.P., "Modelling of unsaturated flow", National Conference on "Modern Trends in Water Resources Development and Environmental Management", 7-8 March 2002, Vellore Institute of Technology, Vellore (Tamil Nadu), pp.1-9, 2002.
46. Lacroix, P., Legrésy, B., Langley, K., Hamran, S. E., Kohler, J., Roques, S. , Rémy, F., Dechambre, M., "Instruments and Methods In situ measurements of snow surface roughness using a laser profiler", Journal of Glaciology, Vol.54, Number 187, pp.753-762(10), December 2008.
47. Lewis, R. W., Nithiarasu, P., Seetharamu, K., "Fundamentals of the Finite Element Method for Heat and Fluid Flow", 2004.
48. Makkonen, L., "Heat transfer and icing of a rough cylinder", Cold Regions Science & Technology, Vol.10, pp.105 - 116, 1985.

49. Margarita Baevay, Plamen Baevz and Alexander Kaplanx, An analysis of the heat transfer from a moving elliptical cylinder, J. Phys. D: Appl. Phys., Vol.30, pp.1190–1196, 1997.

50. Maroulis Z. B., Krokida, M. K., Rahman, M. S., "A structural generic model to predict the effective thermal conductivity of fruits and vegetables during drying", Journal of Food engineering, Vol.52, pp.47-52, 2002

51. Menter, F. R., "Two-Equation Eddy-Viscosity Turbulence Models for Engineering Applications", AIAA Journal, Vol.32 (8), pp.1598-1605, August 1994.

52. Navarre, J. P., Meyssonnier, J. and Vagnon, A., "3D numerical model of snow deformation without failure and its application to cold room mechanical tests", Cold Regions Science and Technology, Vol.50, Issues 1-3, November 2007.

53. Pabla, A. S., "Electric Power Distribution", published by McGraw-Hill companies, Inc., pp.843-844, 2005.

54. Péter, Z., "Modeling and simulation of the ice melting progress on a current-carrying conductor", PhD thesis in Engineering, UQAC, 2006.

55. Pitman, D., Zuckerman, B., "Effective thermal conductivity of snow at -88°C, -27°C and -5°C", 1966.

56. Poots, G., "Ice and snow accretion on structures", Research Studies Press (England) and John Wiley and Sons Inc., New York, NY, USA, 330 p, 1996.

57. Poots, G., "Introductory Remarks", Philosophical Transactions: Mathematical, Physical and Engineering Sciences, Vol. 358, No.1776, Ice and Snow Accretion on Structures, pp. 2803-2810, Nov. 15, 2000.

58. Rahman, S., "Food properties handbook", pp.225-338.

59. Roberge, M., "A study of snow shedding from an overhead cable", Master's Thesis, UQAC, 2006.

60. Sakamoto, Y., "Snow accretion on overhead wires", Philosophical Transactions of the Royal Society, Vol.358, pp.2941-2970, 2000.

61. Sakamoto, Y., Tachizaki, S. and Sudo, N. "Snow accretion on overhead wires". Proceedings of the 11th International Workshop on Atmospheric Icing IWAIS'2005, pp.

3-9, 2005.

62. Satyawali, P. K., Singh, A. K., "Dependence of thermal conductivity of snow on microstructure", 2008.
63. Scholten, J. W. and Murray, D. B., "Unsteady heat transfer and velocity of a cylinder in cross flow- I. Low freestream turbulence", Int. J. Heat Mass Transfer, Vol.41, No. 10, pp.1139-1148, 1998.
64. Schweizer, J., "Laboratory experiments on shear failure of snow", Ann. Glaciol., Vol.26, pp.97–102. 1998.
65. Schweizer, J., "Review of dry snow slab avalanche release", Cold Reg. Sci. Technol., Vol.30 (1–3), 43–57. 1999.
66. Sellers, S., "Theory of water transport in melting snow with moving surface", Cold regions science and technology, Vol.31, pp.47-57, 2000.
67. Shimizu, H., "Air Permeability of Deposited Snow", Institute of Low Temperature Science: Sapporo, Japan: Contribution No. 1053. English Translation, 1970.
68. Singh R. P., "Heating and cooling processes for foods" In: Heldman D. R., Lund D. B., editors. Handbook of food engineering. Marcel Dekker: New York; pp.247-276. 1992.
69. Sokratov, S. A., Maeno, N., "Heat and mass transport in snow under a temperature gradient", Snow engineering, pp.49-52 , 1997.
70. Stoffel, M., "Numerical Modelling of Snow Using Finite Elements", Published by vdf Hochschulverlag AG, 2006.
71. Sturm, M., Johnson, J. B., "Natural Convection in the Subarctic Snow Cover", Journal of Geophysical research, Vol. 96, NO. B7, pp. 11,657-11,671, 1991.
72. Sturm, M., Holmgren, J., König, M. and Morris, K., "The thermal conductivity of seasonal snow", J. Glaciol., Vol.43(143), pp.26–41, 1997.
73. Szczepanik, K., Ooi, A., Aye, L. and Rosengarten, G., "A Numerical Study of Heat Transfer from a Cylinder in Cross Flow", 15th Australasian Fluid Mechanics Conference, the University of Sydney, Sydney, Australia, December 2004.
74. Tseng, P.-H., Illangasekare, T. H. and Meier, M. F., "Modeling of snow melting and uniform wetting front migration in a layered subfreezing snowpack", water resources

research, Vol.30, pp.2363-2376, August 1994.

75. Van Genuchten, M. TH., "A closed-form equation for predicting the hydraulic conductivity of unsaturated soils", Soil SCI. SOC. AM. J., Vol.44, 1980.
76. Verma, L. S., Shrotriya, A. K., Singh, R. and Chaudhry, D. R., "Thermal conduction in two phase materials with spherical and non-spherical inclusions", J.Phys.D: Appl.Phys., Vol.24, pp.1729–1737, 1991.
77. Wakahama, G., Kuroiwa, D.and Goto, K., "Snow accretion on electric wires and its prevention", J. Glaciol. Vol19 (81), pp. 479–487, 1977.
78. Wankiewicz, A., "Water percolation within a deep snowpack—field investigations at a site on Mt Seymour", British. 1976.
79. Wankiewicz, A., "A review of water movement in snow". In Colbeck, S.C. and M. Ray, eds. "Proceedings. Modeling of Snow Cover Runoff". Hanover, NH, Cold Regions Research and Engineering Laboratory, pp.222-252, 1979.
80. Woodside, W. and Messmer, J., "Thermal conductivity of porous media. I: Unconsolidated sands & II: Consolidated sands.", J. Appl Phys. No. 32, pp. 1688–1768,1961.
81. Yukino, T., Hase, Y., Matsuda, M., Nishimura, H., Imaizumi, M., "Experiment of Snow Accretion and Geometrical Analysis of the Shape", IWAIS 1998, pp. 95-99, 1998.
82. Zhukauskas, A., Ziugzda, J., "Heat Transfer of a Cylinder in Cross-flow", Hemisphere Publishing Co., Washington, DC, 1985.

APPENDIX I THERMAL EQUIVALENT CONDUCTIVITY OF SNOW

Empirical Thermal Conductivity Laws

Author (year)	Equations	Comments
Jansson(1901)	$k_{eff} = 0.0209 + 0.000795\rho + 2.511e^{-12}\rho^4$	
Devaux(1933)	$k_{eff} = 0.0293 + 2.93\left(\frac{\rho}{1000}\right)^2$	
Snow Hydrology, 1956	$k_{snow} = S_k\rho^2_{snow}$	s_k is an empirical parameter
Sturm *et al.* (1997)	$k_{eff} = 0.023 + 0.234\left(\frac{\rho}{1000}\right)$	for $\rho < 156 kg/m^3$
Sturm *et* al. (1997)	$k_{eff} = 0.138 - 1.01\left(\frac{\rho}{1000}\right) + 3.233\left(\frac{\rho}{1000}\right)^2$	for $\rho > 156 kg/m^3$
Aggarwal, 2004	$k_e = 3.5926 \times 10^{-3} + 8.402 \times 10^{-4}\rho - 1.7756 \times 10^{-6}\rho^2 + 3.806358 \times 10^{-9}\rho^3$	

APPENDIX II FEM AND FVM MODELING PROCESS

A. FEM

1. Discretization of the continuum

Divide the solution region into non-overlapping elements or sub-regions. The simplest geometric shape that can be employed to approximate irregular surfaces is the triangle and it is one of the popular elements currently used in finite element calculations.

For a cylinder-like geometry, it is usually convenient to apply a radius coordinate thereby causing the schematic of (c) in **Figure 4-13** to be created. This schematic is suitable for the special kind of problems whose results are also radius-symmetric. The melt water flow problem, however, always occurs along the gravity force direction and not in a radial direction. Also, since almost half of the elements are obtuse triangles, which is not good for the convergence of computation.

Creating right triangles, such as (b) in **Figure 4-13**, is easier than creating equilateral triangles, such as (c) in **Figure 4-13**, while constructing a mesh for a cylinder-like geometry. The shape of the equilateral triangle, however, was chosen in this particular study so as to benefit the computation.

The boundary elements should be specifically handled to fit the actual geometry; the need for this recommendation becomes evident upon examining **Figure 4-14**.

2. Select Interpolation or Shape Functions

The next step is to choose the type of interpolation function which represents the variation of the field variable over an element. The number of nodes forms an element; the nature and number of unknowns at each node decide the variation of a field variable within that same element.

A typical triangle element is shown in **Fig. 1**. The pore water pressure head, ψ, distributes into a two-dimensional linear triangular element, also known as a simplex element, and can be represented by

$$\psi = N_i\psi_i + N_j\psi_j + N_k\psi_k = [N_i \quad N_j \quad N_k]\begin{Bmatrix}\psi_i\\ \psi_j\\ \psi_k\end{Bmatrix} \qquad \textbf{Equation 1}$$

where

$$N_i = \frac{1}{2A}(a_i + b_i x + c_i z)$$
$$N_j = \frac{1}{2A}(a_j + b_j x + c_j z) \qquad \textbf{Equation 2}$$
$$N_k = \frac{1}{2A}(a_k + b_k x + c_k z)$$

and

$$a_i = x_j z_k - x_k z_i \quad b_i = z_j - z_k \quad c_i = x_k - x_j$$
$$a_j = x_k z_i - x_i z_k \quad b_j = z_k - z_i \quad c_i = x_i - x_k \qquad \textbf{Equation 3}$$

$$a_k = x_i z_j - x_j z_i \quad b_k = z_i - z_j \quad c_i = x_j - x_i$$

and A is the area of this triangular element.

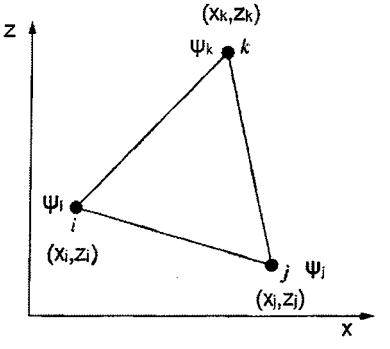

Fig. 1 A linear triangle element

The graduates of the pressure head are given by

$$g = \begin{Bmatrix} \frac{\partial \psi}{\partial x} \\ \frac{\partial \psi}{\partial z} \end{Bmatrix} = \frac{1}{2A} \begin{bmatrix} b_i & b_j & b_k \\ c_i & c_j & c_k \end{bmatrix} \begin{Bmatrix} \psi_i \\ \psi_j \\ \psi_k \end{Bmatrix} = [B]\{\psi\} \qquad \textbf{Equation 4}$$

3. Form Element Equations (Formulation)

Next, the matrix equations expressing the properties of the individual elements by forming an element Left Hand Side (LHS) matrix and load vector must be determined.

From a previous discussion concerning a liner element

$$\bar{\psi} = [N_i \quad N_j \quad N_k] \begin{Bmatrix} \psi_i \\ \psi_j \\ \psi_k \end{Bmatrix} \qquad \textbf{Equation 5}$$

the Governing **Equation 4-3** can be written as

$$f(\psi) = \frac{\partial}{\partial x}\left[Kk_{rw}\left(\frac{\partial \psi}{\partial x}\right)\right] + \frac{\partial}{\partial z}\left[Kk_{rw}\left(\frac{\partial \psi}{\partial z} + 1\right)\right] - C\frac{\partial \psi}{\partial t} = 0 \qquad \textbf{Equation 6}$$

The Galerkin method requires that the following expression be satisfied

$$\int_{\Omega} w_k f(\bar{\psi})\, d\Omega = 0 \qquad \textbf{Equation 7}$$

where the weight, w_k, is replaced by the shape functions at the nodes, N_l, where the subscript l represents the nodes in the domain, as follows,

$$\int_{\Omega} N_l f(\bar{\psi})\, d\Omega = \int_{\Omega} N_l \left\{\frac{\partial}{\partial x}\left[Kk_{rw}\left(\frac{\partial \bar{\psi}}{\partial x}\right)\right] + \frac{\partial}{\partial z}\left[Kk_{rw}\left(\frac{\partial \bar{\psi}}{\partial z} + 1\right)\right] - C\frac{\partial \bar{\psi}}{\partial t}\right\} d\Omega = 0 \qquad \textbf{Equation 8}$$

Integration by parts is often essential when dealing with second-order derivatives. Using Green's lemma, the second derivatives can be rewritten in two parts as

$$\int_{\Omega} N_l \frac{\partial}{\partial x}\left[Kk_{rw}\left(\frac{\partial \bar{\psi}}{\partial x}\right)\right] d\Omega = \int_{S} N_l \left[Kk_{rw}\left(\frac{\partial \bar{\psi}}{\partial x}\right)\right] dS - \int_{\Omega} \frac{\partial N_l}{\partial x}\left[Kk_{rw}\left(\frac{\partial N_m}{\partial x}\right)\right]\{\overline{\psi_m}\}\, d\Omega \qquad \textbf{Equation 9}$$

where m represents the nodes.

For internal nodes, **Equation 9** can be written as

$$\int_{\Omega} N_l \frac{\partial}{\partial x}\left[Kk_{rw}\left(\frac{\partial \bar{\psi}}{\partial x}\right)\right] d\Omega = \int_{\Omega} \frac{\partial N_l}{\partial x} \left[Kk_{rw}\left(\frac{\partial N_m}{\partial x}\right)\right] \{\overline{\psi_m}\}\, d\Omega$$
$$= \int_{\Omega} Kk_{rw} \frac{\partial N_l}{\partial x} \frac{\partial N_m}{\partial x} \{\overline{\psi_m}\}\, d\Omega \qquad \textbf{Equation 10}$$

There is a special item in the governing equation making it possible to take the effects of gravity into account. This item is a first-order derivative and can be rewritten as

$$\int_{\Omega} N_l \frac{\partial}{\partial z}\left[\frac{\partial}{\partial z}(Kk_{rw} z)\right] d\Omega = \int_{S} N_l Kk_{rw}\, dS - \int_{\Omega} \frac{\partial N_l}{\partial z}(Kk_{rw})\, d\Omega \qquad \textbf{Equation 11}$$

For internal nodes, **Equation 11** can be written as

$$\int_{\Omega} N_l \frac{\partial}{\partial z}\left[\frac{\partial}{\partial z}(Kk_{rw} z)\right] d\Omega = -\int_{\Omega} \frac{\partial N_l}{\partial z}(Kk_{rw})\, d\Omega = -Kk_{rw} \int_{\Omega} \frac{\partial N_l}{\partial z} d\Omega$$
$$= -\frac{Kk_{rw}}{2}[c] = -\frac{Kk_{rw}}{2}[c_i \quad c_j \quad c_k] \qquad \textbf{Equation 12}$$

Substituting **Equation 9** and **Equation 11** into **Equation 8** we obtain

$$-\int_{\Omega} Kk_{rw}\left(\frac{\partial N_l}{\partial x}\frac{\partial N_m}{\partial x} + \frac{\partial N_l}{\partial z}\frac{\partial N_m}{\partial z}\right)\{\overline{\psi_m}\}\, d\Omega - \frac{Kk_{rw}}{2}[c_i \quad c_j \quad c_k]$$
$$+ \int_{S} N_l \left[Kk_{rw}\left(\frac{\partial \bar{\psi}}{\partial x}\right)\right] dS + \int_{S} N_l Kk_{rw}\, dS \qquad \textbf{Equation 13}$$
$$- \int_{\Omega} N_l C \frac{\partial \bar{\psi}}{\partial t} d\Omega = 0$$

4. Assembling the Element Equations to Obtain a System of Simultaneous Equations

To find the properties of the overall system, all the individual element equations must be assembled; that is to say, the matrix equations of each element must be combined appropriately in such a way as to cause the resulting matrix to represent the behavior of the

entire solution region of the problem. The boundary conditions should be incorporated after assembling the contributions of the individual element, that is,

$$[C_m]\left\{\frac{\partial \psi}{\partial t}\right\} + [K_{km}]\{\psi\} = \{f\} \qquad \textbf{Equation 14}$$

where $[\mathbf{K_{km}}]$ is the global LHS matrix, which is the uniting of the individual element LHS matrices, as given by,

$$[K_{km}] = -\int_{\Omega} Kk_{rw}\left(\frac{\partial N_l}{\partial x}\ \frac{\partial N_m}{\partial x} + \frac{\partial N_l}{\partial z}\ \frac{\partial N_m}{\partial z}\right)\{\overline{\psi_m}\}\, d\Omega \qquad \textbf{Equation 15}$$

$\{\mathbf{f}\}$ is the global load vector, which is the uniting of the individual element load vectors,

$$\{f\} = \frac{Kk_{rw}}{2}[c] + \int_S N_l\left[Kk_{rw}\left(\frac{\partial \bar{\psi}}{\partial x}\right)\right] dS + \int_S N_l Kk_{rw}\, dS \qquad \textbf{Equation 16}$$

$\{\psi\}$ is the global unknown vector,

and $[\mathbf{C_m}]$ is defined as

$$[C_m] = \int_{\Omega} CN_l N_m d\Omega \qquad \textbf{Equation 17}$$

5. Time Discretization

Choosing an integration method for extrapolating the state variables is an extremely important task, and may prove difficult for non-linear systems such as the one under observation. It is of utmost importance to ensure that the system is stable over time as well as physically correct while maintaining storage requirements and computational costs to a

minimum. Unfortunately, it is difficult to find an effective way for two- or three dimensional modeling.

Using the Taylor series, the pressure head ψ can be written as

$$\psi^{n+1} = \psi^n + \Delta t\frac{\partial\psi^n}{\partial t} + \frac{\Delta t^2}{2}\frac{\partial^2\psi^n}{\partial t} + \cdots \qquad \textbf{Equation 18}$$

If second- and higher- order terms in the above equation are disregarded, then

$$\frac{\partial\psi^n}{\partial t} \approx \frac{\psi^{n+1} - \psi^n}{\Delta t} + O(\Delta t) \qquad \textbf{Equation 19}$$

which is the first accurate order in time. If parameter $\boldsymbol{\beta}$ is introduced to the above equation, then

$$\psi^{n+\beta} = \beta\psi^{n+1} + (1-\beta)\psi^n \qquad \textbf{Equation 20}$$

Substituting **Equation 20** into **Equation 14** it is possible to obtain

$$[C_m]\left\{\frac{\psi^{n+1} - \psi^n}{\Delta t}\right\} + [K_{km}]\{\psi\}^{n+\beta} = \{f\}^{n+\beta} \qquad \textbf{Equation 21}$$

or

$$[C_m]\left\{\frac{\psi^{n+1} - \psi^n}{\Delta t}\right\} + [K_{km}]\{\beta\psi^{n+1} + (1-\beta)\psi^n\} = \beta\{f\}^{n+1} + (1-\beta)\{f\}^n \qquad \textbf{Equation 22}$$

The above equation can be rearranged as follows:

$$([C_m] + \beta\Delta t[K_{km}])\psi^{n+1} = ([C_m] - (1-\beta)[K_{km}]\Delta t)\psi^n + \Delta t(\beta\{f\}^{n+1} + (1-\beta)\{f\}^n) \quad \textbf{Equation 23}$$

where

$$C_m^{n+\beta} = \beta C_m^{n+1} + (1-\beta)C_m^n$$
$$K_{km}^{n+\beta} = \beta K_{km}^{n+1} + (1-\beta)K_{km}^n \quad \textbf{Equation 24}$$

6. Solution to the System of Equations

The resulting set of algebraic equations for **Equation 23** may now be solved to obtain the nodal values of the field variable.

B. FVM

The finite volume method can be considered as a further refined version of the finite difference method and has become widely used in computational fluid dynamics. The vertex-centered finite volume technique is similar to the linear finite element method.

Most of the finite difference schemes used in fluid dynamics and heat transfer problems can be viewed as special cases within a weighted residual framework. For weighted residual procedures, the error in the approximate solution of the conservation equations is not set to zero, but instead its integral, with respect to selected 'weights', is required to vanish. Within this family, the collocation method reproduces the classical finite difference equations, whereas the finite volume algorithm is obtained by using constant weights.

1. Discretization of the continuum

It can be considered that no elements but only nodes exist in the FVM. However, to achieve a vector for a given node, the four adjacent nodes must be known. It may be assumed that there exists a virtual element (usually a rhombic shape, as shown in **Fig. 2**) consisting of five nodes for each node being solved.

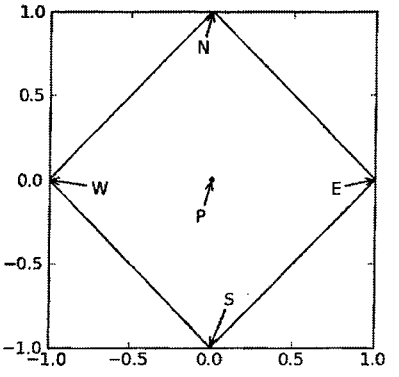

Fig. 2 A virtual element in FVM mesh

2. Governing Equation Discretization

The key step in FEM is the integration of the governing equation over a control volume to obtain a discretized equation at its nodal point.

FEM requires that the following expression be satisfied

$$\int_{\Delta V} f(\psi)\, dV = 0 \qquad \textbf{Equation 25}$$

or

$$\int_{\Delta V} \left\{\frac{\partial}{\partial x}\left[Kk_{rw}\left(\frac{\partial \psi}{\partial x}\right)\right] + \frac{\partial}{\partial z}\left[Kk_{rw}\left(\frac{\partial \psi}{\partial z} + 1\right)\right] - C\frac{\partial \psi}{\partial t}\right\} dV = 0 \qquad \textbf{Equation 26}$$

where V refers to a control volume. For two-dimensional models, the above equation can be written as

$$\int_{\Delta S} \left\{\frac{\partial}{\partial x}\left[Kk_{rw}\left(\frac{\partial \psi}{\partial x}\right)\right] + \frac{\partial}{\partial z}\left[Kk_{rw}\left(\frac{\partial \psi}{\partial z} + 1\right)\right] - C\frac{\partial \psi}{\partial t}\right\} dx.dz = 0 \qquad \textbf{Equation 27}$$

The schematic of a two-dimensional grid for FEM is shown in **Fig. 3**. The discretization of the governing equation can be obtained by

$$\left[\left(Kk_{rw}\left(\frac{\partial \psi}{\partial x}\right)\right)_e - \left(Kk_{rw}\left(\frac{\partial \psi}{\partial x}\right)\right)_w\right] + \left[\left(Kk_{rw}\left(\frac{\partial \psi}{\partial z}\right)\right)_n - \left(Kk_{rw}\left(\frac{\partial \psi}{\partial z}\right)\right)_s\right] + [(Kk_{rw})_n - (Kk_{rw})_s] + \int_{\Delta S} \left\{-C\frac{\partial \psi}{\partial t}\right\} dS = 0 \qquad \textbf{Equation 28}$$

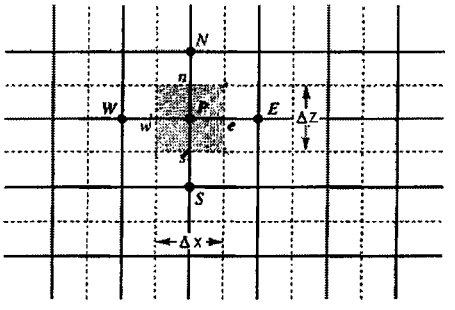

Fig. 3 Schematic of a two-dimensional grid

As shown in **Fig. 3**, the expression of water flux through the control volume faces can be written as

$$water\ flow\ accross\ west\ face\ =\ \mathrm{Kk_{rw}}\left(\frac{\partial\psi}{\partial \mathrm{x}}\right):\mathrm{w}\ =\ \mathrm{Kk_{rw}}\frac{\psi_P-\psi_W}{\delta \mathrm{x_{WP}}}$$

$$water\ flow\ accross\ east\ face\ =\ \mathrm{Kk_{rw}}\left(\frac{\partial\psi}{\partial \mathrm{x}}\right):\mathrm{e}\ =\ \mathrm{Kk_{rw}}\frac{\psi_E-\psi_P}{\delta \mathrm{x_{PE}}}$$

$$water\ flow\ accross\ north\ face\ =\ \mathrm{Kk_{rw}}\left(\frac{\partial\psi}{\partial \mathrm{y}}\right):\mathrm{n}\ =\ \mathrm{Kk_{rw}}\frac{\psi_N-\psi_P}{\delta \mathrm{z_{PN}}}$$

$$water\ flow\ accross\ south\ face\ =\ \mathrm{Kk_{rw}}\left(\frac{\partial\psi}{\partial \mathrm{y}}\right):\mathrm{s}\ =\ \mathrm{Kk_{rw}}\frac{\psi_P-\psi_S}{\delta \mathrm{z_{SP}}}$$

Equation 29

By substituting the above expressions into **Equation 28,** and **Equation 26,**

$$\mathrm{a_p}\psi_P-\mathrm{a_W}\psi_W-\mathrm{a_E}\psi_E-\mathrm{a_N}\psi_N-\mathrm{a_S}\psi_S\ =\ S \qquad \textbf{Equation 30}$$

is obtained where

$\mathrm{a_W}$	$\frac{\mathrm{Kk_{rw}}}{\delta \mathrm{x_{WP}}}$	$\mathrm{a_N}$	$\frac{\mathrm{Kk_{rw}}}{\delta \mathrm{z_{PN}}}$
$\mathrm{a_E}$	$\frac{\mathrm{Kk_{rw}}}{\delta \mathrm{x_{PE}}}$	$\mathrm{a_S}$	$\frac{\mathrm{Kk_{rw}}}{\delta \mathrm{z_{SP}}}$
$\mathrm{a_P}$	$\mathrm{a_W}+\mathrm{a_E}+\mathrm{a_S}+\mathrm{a_N}$		
S	$-[(\mathrm{Kk_{rw}})_n-(\mathrm{Kk_{rw}})_s]+\int_{\Delta S}\left\{\mathrm{C}\frac{\partial\psi}{\partial t}\right\}\mathrm{dS}$		

3. Time Discretization

Using the same time discretization discussed in FEM, **Equation 30** can be written as

$$\begin{aligned}&\mathrm{a_p}\psi_P-\beta(\mathrm{a_W}\psi_W+\mathrm{a_E}\psi_E+\mathrm{a_N}\psi_N+\mathrm{a_S}\psi_S)\\&\quad-(1-\beta)\left(\mathrm{a_W}\psi_W^0+\mathrm{a_E}\psi_E^0+\mathrm{a_N}\psi_N^0+\mathrm{a_S}\psi_S^0-\mathrm{a_P}\psi_P^0\right)\\&\quad-\beta[(\mathrm{Kk_{rw}})_n-(\mathrm{Kk_{rw}})_s]-(1-\beta)[(\mathrm{Kk_{rw}^0})_n-(\mathrm{Kk_{rw}^0})_s]\\&=\frac{\psi_P-\psi_P^0}{\Delta t}\int_{\Delta S}\mathrm{CdS}\ =\ \frac{\psi_P-\psi_P^0}{\Delta t}[\mathrm{C_m}]\end{aligned} \qquad \textbf{Equation 31}$$

The above equation can be rearranged as follows:

$$\left(a_p - \frac{\psi_P}{\Delta t}[C_m]\right)\psi_P - \beta(a_W\psi_W + a_E\psi_E + a_N\psi_N + a_S\psi_S) = (1-\beta)\left(a_W\psi_W^0 + a_E\psi_E^0 + a_N\psi_N^0 + a_S\psi_S^0 - a_P\psi_P^0\right) + \beta[(Kk_{rw})_n - (Kk_{rw})_s] + (1-\beta)[(Kk_{rw}^0)_n - (Kk_{rw}^0)_s] - \frac{\psi_P^0}{\Delta t}[C_m] \quad \textbf{Equation 32}$$

or

$$[K_m]\{\psi\} = \{f\} \quad \textbf{Equation 33}$$

where

$$[K_m] = \left[\left(a_p - \frac{\psi_P}{\Delta t}[C_m]\right) \quad -\beta a_W \quad -\beta a_E \quad -\beta a_S \quad -\beta a_N\right]$$

$$\{\psi\} = \begin{Bmatrix}\psi_P\\ \psi_W\\ \psi_E\\ \psi_S\\ \psi_N\end{Bmatrix}$$

$$\{f\} = (1-\beta)\left(a_W\psi_W^0 + a_E\psi_E^0 + a_N\psi_N^0 + a_S\psi_S^0 - a_P\psi_P^0\right) + \beta[(Kk_{rw})_n - (Kk_{rw})_s] + (1-\beta)[(Kk_{rw}^0)_n - (Kk_{rw}^0)_s] - \frac{\psi_P^0}{\Delta t}[C_m] \quad \textbf{Equation 34}$$

$$C_m^{n+\beta} = \beta C_m^{n+1} + (1-\beta)C_m^n$$

4. Solution to the System of Equations

The resulting set of algebraic equations, **Equation 33**, may now be solved to obtain the nodal values of the field variable.